Davis, E. E., Mottl, M. J., Fisher, A. T., et al., 1992
Proceedings of the Ocean Drilling Program, Initial Reports, Vol. 139

5. SITE 855[1]

Shipboard Scientific Party[2]

HOLE 855A

Date occupied: 15 July 1991

Date departed: 16 July 1991

Time on hole: 1 day, 3 hr, 15 min

Position: 48°26.563′N, 128°38.271′W

Bottom felt (drill-pipe measurement from rig floor, m): 2455.5

Distance between rig floor and sea level (m): 10.70

Water depth (drill-pipe measurement from sea level, m): 2444.8

Total depth (rig floor, m): 2531.90

Penetration (m): 76.40

Number of cores (including cores with no recovery): 9

Total length of cored section (m): 76.40

Total core recovered (m): 33.99

Core recovery (%): 44

Oldest sediment cored:
Depth below seafloor (m): 64.96
Nature: silty clay
Earliest age: Pleistocene
Measured velocity (km/s): 1.530

Hard rock:
Depth below seafloor (m): 76.40
Nature: phyric basalt

Basement:
Depth below seafloor (m): 64.96
Nature: basalt

HOLE 855B

Date occupied: 16 July 1991

Date departed: 17 July 1991

Time on hole: 12 hr

Position: 48°26.568′N, 128°38.254′W

Bottom felt (drill-pipe measurement from rig floor; m): 2457.0

Distance between rig floor and sea level (m): 10.70

Water depth (drill-pipe measurement from sea level, m): 2446.3

Total depth (rig floor; m): 2520.30

Penetration (m): 63.30

Number of cores (including cores with no recovery): 8

Total length of cored section (m): 63.30

Total core recovered (m): 12.39

Core recovery (%): 19

Oldest sediment cored:
Depth below seafloor (m): 44.5
Nature: silty clay
Earliest age: Pleistocene
Measured velocity (km/s): 1.574

Hard rock:
Depth below seafloor (m): 63.30
Nature: basalt

Basement:
Depth below seafloor (m): 53.60
Nature: basalt

HOLE 855C

Date occupied: 17 July 1991

Date departed: 18 July 1991

Time on hole: 1 day, 0 hr, 30 min

Position: 48°26.571′N, 128°38.321′W

Bottom felt (drill-pipe measurement from rig floor m): 2454.5

Distance between rig floor and sea level (m): 10.70

Water depth (drill-pipe measurement from sea level, m): 2443.8

Total depth (rig floor; m): 2565.50

Penetration (m): 111.00

Number of cores (including cores with no recovery): 13

Total length of cored section (m): 111.00

Total core recovered (m): 60.77

Core recovery (%): 54

Oldest sediment cored:
Depth below seafloor (m): 101.20
Nature: plagioclase sand and plagioclase silty clay
Earliest age: Pleistocene
Measured velocity (km/s): 1.702

Hard rock:
Depth below seafloor (m): 111.00
Nature: basalt

Basement:
Depth below seafloor (m): 101.20
Nature: basalt

HOLE 855D

Date occupied: 18 July 1991

Date departed: 18 July 1991

Time on hole: 17 hr, 45 min

Position: 48°26.542′N, 128°38.317′W

Bottom felt (drill-pipe measurement from rig floor, m): 2454.5

Distance between rig floor and sea level (m): 10.70

Water depth (drill-pipe measurement from sea level, m): 2443.8

Total depth (rig floor; m): 2573.10

Penetration (m): 118.60

Number of cores (including cores with no recovery): 6

[1] Davis, E. E., Mottl, M. J., Fisher, A. T., et al., 1992. *Proc. ODP, Init. Repts.,* 139: College Station, TX (Ocean Drilling Program).
[2] Shipboard Scientific Party is as given in the list of participants preceding the contents.

Total length of cored section (m): 39.10

Total core recovered (m): 1.98

Core recovery (%): 5

Oldest sediment cored:
Depth below seafloor (m): 108.50
Nature: silty hemipelagic clay
Earliest age: Pleistocene

Hard rock:
Depth below seafloor (m): 118.60
Nature: basalt

Basement:
Depth below seafloor (m): 113.90
Nature: basalt

Principal results: Site 855 is located along the normal fault that forms the eastern topographic boundary of the sedimented rift valley, Middle Valley, of the northern Juan de Fuca Ridge. Throw on the fault of about 115 m is greater than the local sediment thickness of about 90 m, so that basement is exposed along the seafloor scarp. Four holes were drilled at Site 855 to form a transect across the hanging-wall block (Table 1). Individual holes were located 40 m (Hole 855B), 70 m (Hole 855A), and 125 m (Holes 855C and 855D) from the base of the scarp. Precise estimates of these ranges were obtained from a Mesotech scanning sonar image made of the scarp from the bottom of the drill string before spudding the first hole.

The objectives of this transect were to define the cross-sectional geometry and hydrologic nature of this rift-bounding fault, and to determine the nature and rate of fluid flow along the fault or through basement in this part of the rift valley where seawater may be drawn into basement either along the fault outcrop or through the thin sediment section.

All holes (see Table 2 for coring summary) intersected basalt, two inferred to be in the foot wall (Holes 855A and 855B) and two in the hanging wall (Holes 855C and 855D). The offsets from the scarp and the depths to basalt (determined by the depth at which the drilling rate abruptly decreased) at Holes 855A (74 m) and 855B (45 m) provide a lower limit of the dip of the fault. The apparent dip is about 45°. Whether this is the true dip, or reflects the average dip of a zone of en-echelon stair-step faults, cannot be ascertained. The depths to basalt at Hole 855C (98 m) and 855D (108 m) are consistent with the reflection time to basement (130 ms TWT) and the acoustic velocities determined for the section.

Drilling conditions and recovery in basalt were poor, with binding and hole collapse typical at all holes. The objective of reaching the normal fault zone at a level of basalt/basalt contact, estimated to be about 35 m sub-basement at the location of Holes 855C and 855D in the hanging-wall block (see inferred geometry shown in Fig. 35), was not possible. Operations were terminated after 3, 18, 9, and 11 m of basement penetration at Holes 855A, 855B, 855C, and 855D, respectively. Total penetration depths were not sufficient to permit logging.

Small pieces of basalt were recovered at each hole, with basalt recovery averaging 8%. Given the simple fault geometry inferred, this disposition of the basement samples may allow the basaltic section to be characterized at three levels, one at the top of basement (Holes 855C and 855D), one at roughly 60 m sub-basement (Hole 855B), and one at 100 m sub-basement (Hole 855A). The samples range from porphyritic basalt with large phenocrysts of plagioclase and olivine, to basalt containing only sparse phenocrysts of plagioclase. Relatively fresh glassy margins are present on many samples, although most of the samples show various degrees of low-temperature alteration. No systematic spatial or depth variations are evident.

Drilling at this site was done with the rotary core barrel (RCB) so that objectives in basement could be reached with a single pipe trip. Unfortunately, the RCB cores in the unconsolidated sediment section were mechanically disturbed and core recovery on average was only 39%. A single lithologic unit was defined which consists of dark green to gray clay, silty clay, and quartz-plagioclase sandy silt and silty sand, comprising fining-upward turbidite sequences throughout the cored interval. The sequences range in thickness from 13 to 131 cm. In Hole 855C we cored 28 such sequences in 98 m. They are readily detected in magnetic susceptibility traces obtained on the multisensor track, in which positive peaks correspond with coarse sediments at the base of the units. Clear correlations between local lithology, thermal conductivity, porosity, and remanent magnetization were also defined, despite the coring disturbances.

Table 1. Summary of hole locations and depths.

Hole	Depth[a] (mbrf)	Offsets from beacon	GPS position
855A	2455.5	0 m N, 218 m E	48° 26.563′N, 128° 38.271′W
855B	2457.0	0 m N, 247 m E	48° 26.568′N, 128° 38.254′W
855C	2454.5	9 m N, 163 m E	48° 26.571′N, 128° 38.321′W
855D	2454.5	40 m S, 163 m E	48° 26.542′N, 128° 38.317′W
[b]Computed beacon position:			48° 26.565′N, 128° 38.452′W

[a]Depths given in meters below rig floor. Depths below sea level can be calculated by subtracting height of rig floor above water line at this site (10.7 m).
[b]See "Explanatory Notes" chapter (this volume).

Table 2. Site 855 coring summary.

Core	Date (July 1991)	Time (UTC)	Depth (mbsf)	Cored (m)	Recovered (m)	Recovery (%)
139-855A-						
1R	16	0210	0.0–7.6	7.6	6.99	92.0
2R	16	0325	7.6–16.6	9.0	7.32	81.3
3R	16	0425	16.6–26.0	9.4	4.90	52.1
4R	16	0520	26.0–35.5	9.5	5.94	62.5
5R	16	0820	35.5–45.5	10.0	2.31	23.1
6R	16	0905	45.5–55.1	9.6	1.94	20.2
7R	16	0950	55.1–64.8	9.7	3.93	40.5
8R	16	1100	64.8–74.3	9.5	0.33	3.5
9R	16	1300	74.3–76.4	2.1	0.33	15.7
			Coring totals	76.4	33.99	44.5
139-855B-						
1R	16	1530	0.0–5.7	5.7	0.00	0.0
2R	16	1620	5.7–15.1	9.4	3.02	32.1
3R	16	1700	15.1–24.5	9.4	0.00	0.0
4R	16	1745	24.5–34.0	9.5	7.86	82.7
5R	16	1830	34.0–43.9	9.9	0.65	6.6
6R	16	1930	43.9–48.6	4.7	0.69	14.7
7R	16	2110	48.6–53.6	5.0	0.00	0.0
8R	17	0100	53.6–63.3	9.7	0.17	1.8
			Coring totals	63.3	12.39	19.6
139-855C-						
1R	17	0305	0.0–8.7	8.7	8.45	97.1
2R	17	0405	8.7–17.7	9.0	9.33	103.0
3R	17	0725	17.7–27.1	9.4	7.66	81.5
4R	17	0810	27.1–36.6	9.5	5.96	62.7
5R	17	1035	36.6–46.5	9.9	0.02	0.2
6R	17	1135	46.5–56.1	9.6	9.86	103.0
7R	17	1345	56.1–65.7	9.6	9.36	97.5
8R	17	1445	65.7–75.2	9.5	1.54	16.2
9R	17	1700	75.2–84.9	9.7	0.59	6.1
10R	17	1745	84.9–94.6	9.7	5.66	58.3
11R	17	2030	94.6–101.2	6.6	2.32	35.1
12R	17	2230	101.2–106.9	5.7	0.02	0.4
13R	18	0145	106.9–111.0	4.1	0.00	0.0
			Coring totals	111.0	60.77	54.7
139-855D-						
1R	18	0650	79.5–85.0	5.5	0.00	0.0
2R	18	0750	85.0–94.7	9.7	0.00	0.0
3R	18	1050	94.7–104.3	9.6	0.46	4.8
4R	18	1125	104.3–108.5	4.2	0.78	18.6
5R	18	1320	108.5–113.9	5.4	0.24	4.4
6R	18	1945	113.9–118.6	4.7	0.50	10.6
			Coring totals	39.1	1.98	5.1

Pore waters squeezed from the sediments and collected *in situ* with the water-sampler temperature probe indicate that fluids in basement at all four holes are nearly identical to seawater. Chlorinity, alkalinity, sulfate, Mg, Ca, and silica all display maxima or minima within the sediment section and then return to seawater values near basement. Coupled with the low heat flow found in Hole 855C, these data indicate that seawater is being drawn down into the basalt layer along the outcrop at the fault scarp.

BACKGROUND AND OBJECTIVES

Site 855 is located in the easternmost part of Middle Valley along the base of the first major fault scarp that, at this latitude, forms the topographic boundary of the valley (Figs. 1 and 2). The site, comprising an array of four closely spaced holes, is situated in the hanging wall of the axis-facing normal fault that has produced the scarp. The positions of individual holes (Fig. 3) were established with the intention of intersecting the fault at a variety of depths ranging from a few tens to a few hundred meters, and possibly into a variety of combinations of lithologies in contact across the fault, including unconsolidated sediment, consolidated sediment, altered sediment, and basalt. The dip of the fault to be intersected was initially estimated on the basis of (1) seismic reflection data, and (2) the combination of the scarp height defined by the local bathymetry and the plan-view width of the scarp as determined from acoustic image data (see "Site Geophysics and Geology" section, this chapter).

Drilling at this site was intended to provide information about the rates and geochemical consequences of fluid flow in the part of the rift where diffuse or localized draw-down of fluids could occur, and about the influence of a major fault zone on the hydrologic regime. Also the heat flow in this part of the rift (ca. 0.5 W/m^2; Davis and Villinger, this volume) is about half that at other sites occupied during the leg. Thus the site provides a reference section of sediment with a low thermal gradient, to which the sections at other sites, where the effects of higher temperatures and upward fluid flow may be present, can be compared.

SITE GEOPHYSICS AND GEOLOGY

Individual hole positions at Site 855 were established with respect to the normal-fault scarp seen in seismic data (Fig. 1), bathymetry (Fig. 2A), surface- and deep-towed side-scan acoustic imagery (Figs. 2B and 3), and 3.5-kHz profiling (Fig. 4). Precise control for siting the beacon and the holes was provided by a final survey using the TV camera and acoustic scanner on the end of the drill string (see "Operations" section, this chapter). Throw on the fault at this location (see discussion below) has produced steep relief at the seafloor. The change in water depth across the scarp is 115 m, whereas the width of the scarp in plan view at this location, as defined by the side-scan acoustic imagery, is only about 100 m (Figs. 2B and 3). The slope of the seafloor thus defined is 50°. The image of the fault is consistently very narrow along its length, and there is no evidence for accumulation of debris at the base of the scarp.

Of all sites in Middle Valley, Site 855 is located farthest from the rift axis, over crust that could be as old as 400,000 yr (Davis and Villinger, this volume). Its location with respect to the structure of the valley is shown in Figure 1 (see also maps and profiles in back pocket, this volume). Acoustic basement rises in discrete steps from the valley axis, where the sediment section is roughly 800–1000 milliseconds (ms) thick, to higher levels in the east. Beneath Site 855 at the eastern valley-bounding fault scarp, basement appears to lie at a depth of just over 100 ms two-way traveltime (TWT) below the seafloor.

The definition of basement in the multichannel seismic (MCS) profile is not sharp; coherent reflectors can be seen over a considerable interval, typically 200 to 300 ms deeper than the first bright basement arrival, at many locations along the line. This acoustic character can be seen near Site 855 along MCS line 89-13, west of shotpoint 900 (Fig. 5). There, strong arrivals begin at about 200 ms below seafloor (bsf), and reverberant, coherent arrivals persist in the MCS data to over 600 ms bsf.

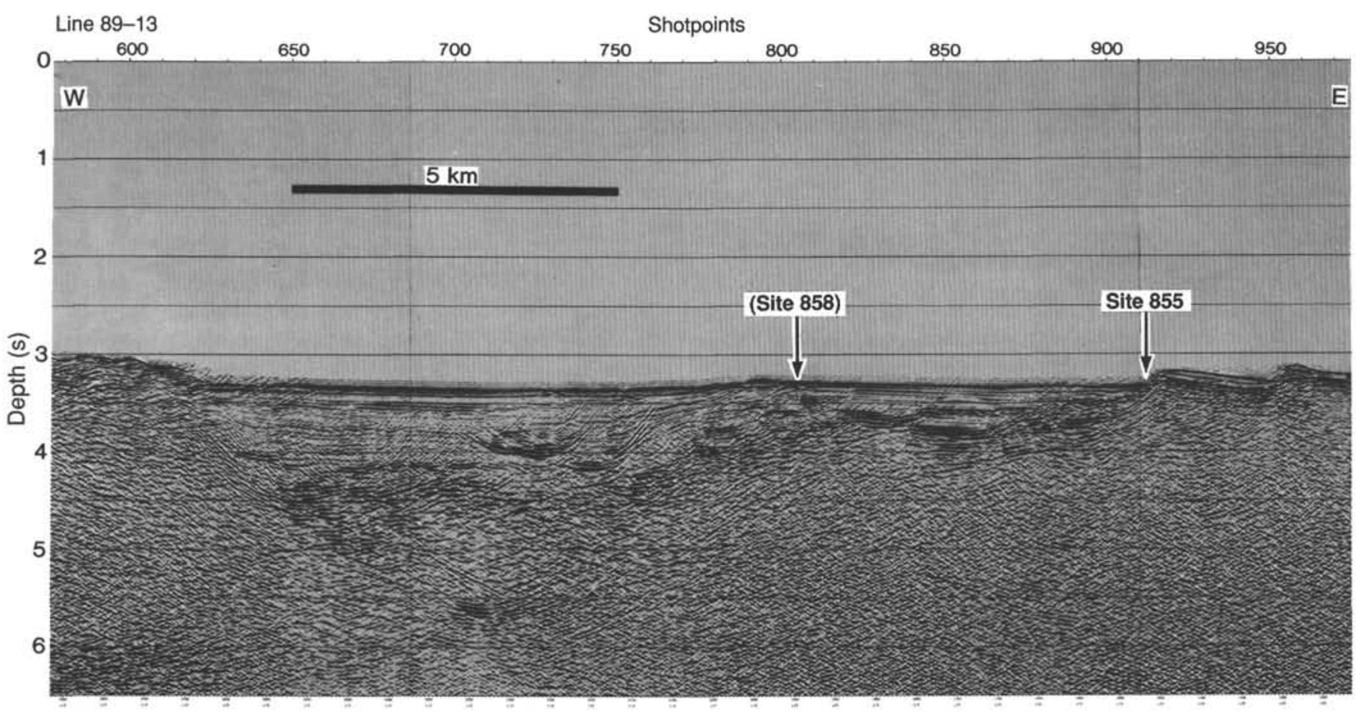

Figure 1. Multichannel seismic reflection profile 89-13, crossing Middle Valley and Site 855 (from Rohr et al., 1992). The location of Site 858 is shown for reference.

A

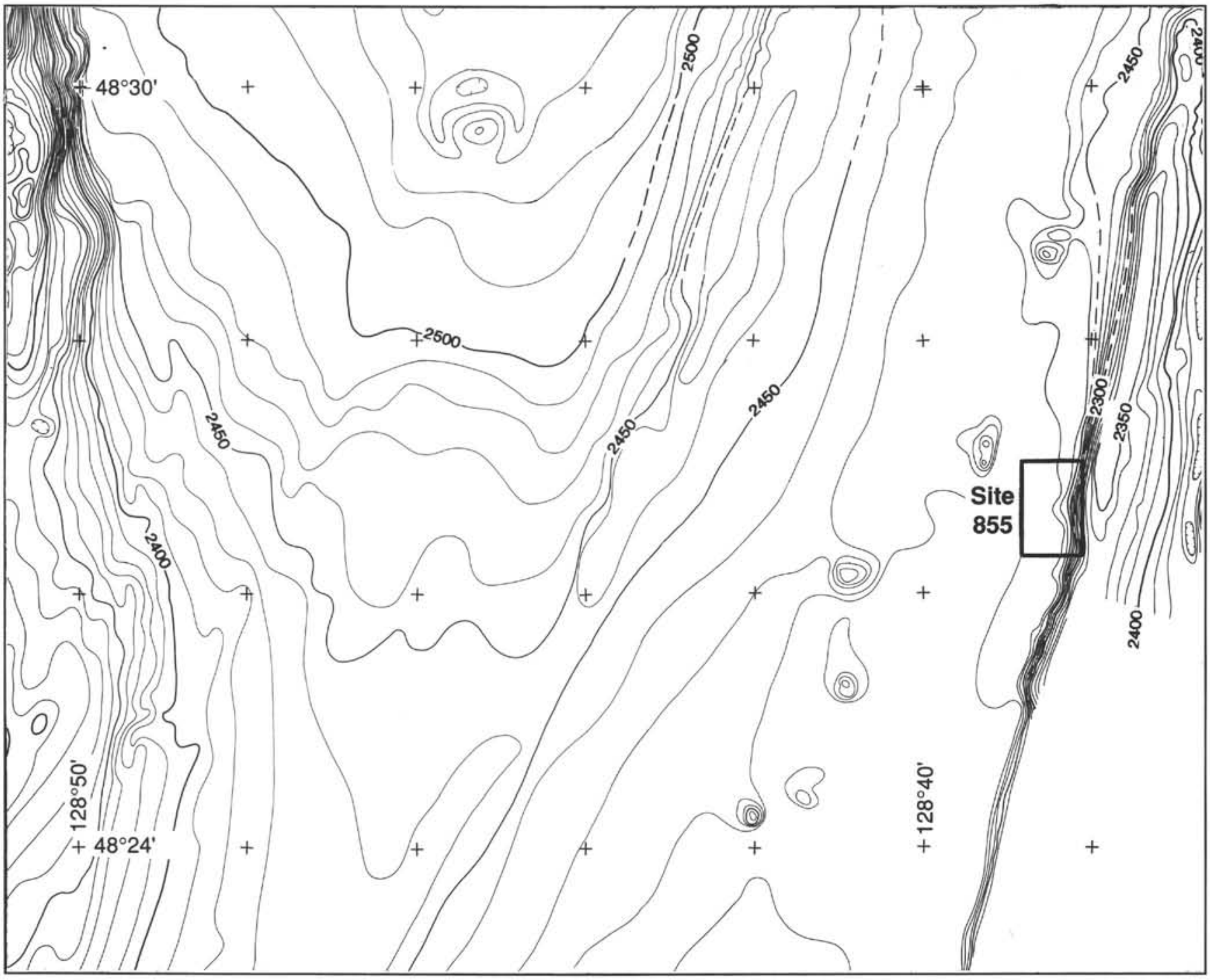

Figure 2. **A.** Bathymetry in the part of Middle Valley occupied by Leg 139, based on continuous SeaBeam swath soundings. Depths are computed using a sonic velocity of 1500 m/s and contoured at 10-m intervals. **B.** Long-range SeaMARC II side-scan acoustic imagery of the same area as in (A), showing the narrow image of the fault scarp at the base of which the holes at the site were drilled. The area included in Figure 3 is outlined.

Directly beneath Site 855, this reverberant character is not observed; coherent reflections are absent below about 200 ms bsf. The seafloor reflection in the MCS data is strong (Fig. 6), although locally the waveform is somewhat distorted by the presence of diffracted energy from the fault scarp. Immediately below the seafloor, the section is fairly transparent. At a depth of 120 ms bsf, a bright event is present, nominally 50%–100% higher in amplitude than the seafloor reflection. Some reverberant energy persists to a depth of about 180 ms bsf. The section in the foot wall immediately east of the fault scarp is very similar to that of the hanging wall, with the same bright event present 120 ms below the seafloor reflection. A local match in seismic stratigraphy is also seen in the 3.5-kHz profile across the fault (Fig. 4); these observations indicate that the scarp has been produced during the time following deposition of the full sediment section at this location. The throw on the fault as determined by the total bathymetric relief of the scarp, 115 m, is somewhat greater than the depth to the reflective horizon of roughly 100 m, as estimated from the traveltime to the event and the average velocity to this depth as given in Davis and Villinger (this volume; 1610 m/s), and as determined by the drilling results. Thus, the horizon, inferred to be basement, probably outcrops just above the base of the scarp.

Heat flow through the seafloor of the hanging wall in the vicinity of Site 855 ranges from 470 mW/m^2 to more than 600 mW/m^2 (Fig. 7). Two measurements closest to the site are situated 200–300 m farther away from the scarp than the drilling site; values are 480 and 505 mW/m^2. Several transects of measurements near the site cross the fault from the hanging wall to the foot wall. No clear systematic pattern is observed in the hanging wall; in the foot wall, there is a tendency for values to be anomalously low near the fault and to increase to the east. This pattern is best displayed along the transect located about 2 km south of Site 855 (Fig. 7). There the heat flow decreases from about 500 mW/m^2 at the base of the scarp to 300 mW/m^2 at the top. Values then increase steadily with distance east of the scarp back up to 500 mW/m^2 at the base of the next fault scarp. The cause of this variability is inferred to be topographically forced flow through the back-tilted igneous layer lying beneath the roughly 100-m-thick sediment section of the foot wall block east of the fault (see Davis and Villinger, this volume).

B

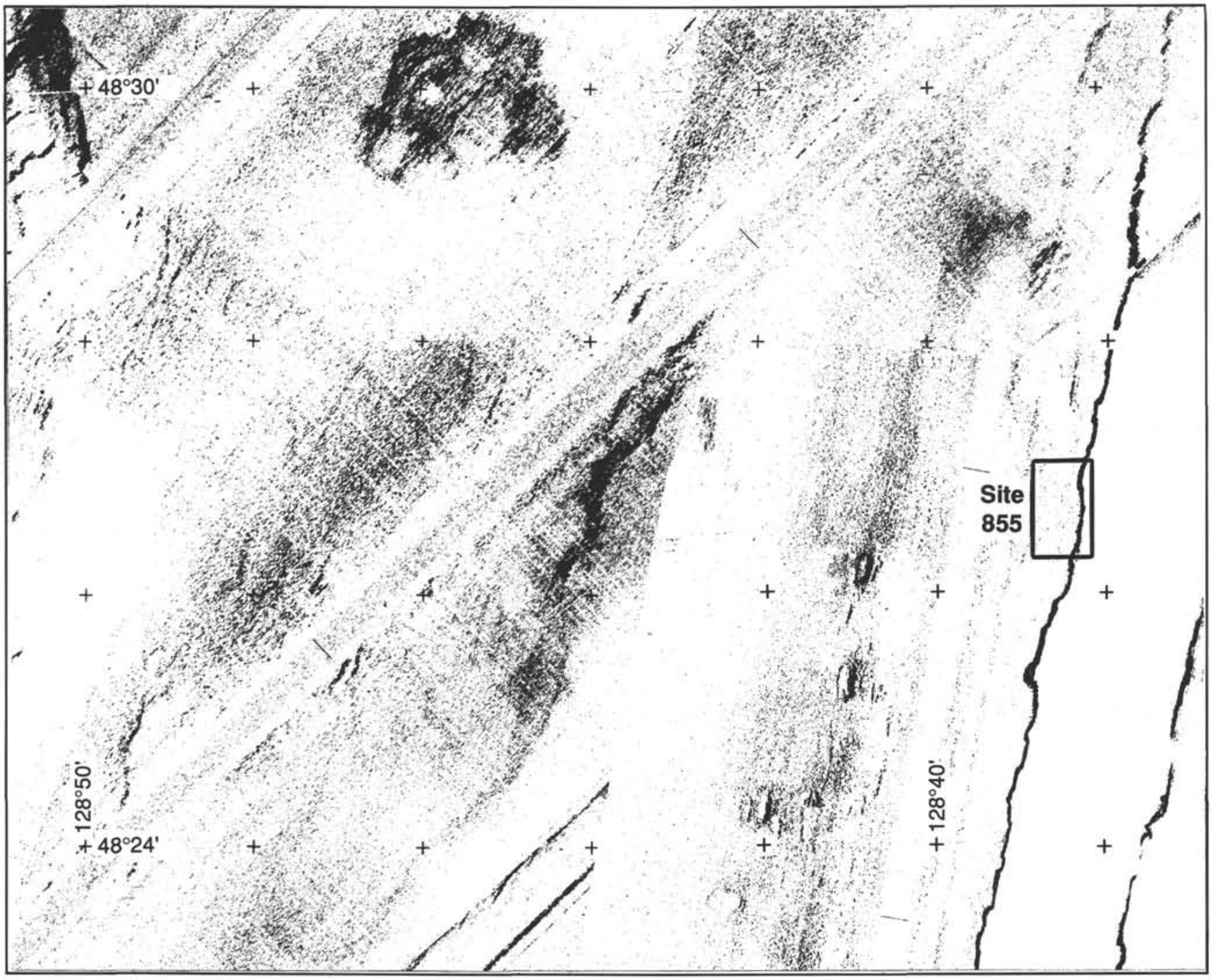

Figure 2 (continued).

OPERATIONS

Hole 855A

After completing the initial site survey and verifying the position of the fault scarp, at the base of which Site 855 was to be located, a recoverable beacon was dropped approximately 240 m west of the base of the scarp. We then offset approximately 200 m east of the beacon and began deploying the drill string.

The initial pipe trip proceeded slowly because of the need to measure and clean the drill string at the first site of each leg. When about half the drill pipe had been run, the vibration-isolated television camera frame was deployed so that the sonar/television sensors would reach scanning depth at about the same time as the bit.

The site was located on the downthrown limb of the eastern boundary fault of Middle Valley. The drilling objective of Hole 855A was to penetrate the fault plane at a relatively shallow depth below the seafloor. The spud location was selected by locating the escarpment with the Mesotech scanning sonar and offsetting the rig with the dynamic positioning system to the proper spot. The drill string and camera frame then were lowered so that spud-in could be observed with the underwater TV camera. The fault appeared as single, thin, and linear bright reflector rather than a zone of greater backscatter.

The image is interpreted to result from a discrete layer, probably the top of the basalt layer outcropping along the fault scarp. The initial spud was made at 1600 hr UTC, when sediment disturbance was seen on the monitor. The offset from the bright reflector was 80 m, and allowing for the 45° dip of the scarp and a 10-m local elevation of the layer above the hanging-wall seafloor, a distance from the base of the scarp was estimated as 70 m. The drill pipe was marked at 2455.5 m from the driller's datum at the dual elevator stool, which was 10.7 m above sea level.

When the first core barrel was retrieved, the core-catcher flapper hinge was found to have failed, allowing the contents of the barrel to escape. The camera frame then was recovered and a second spud was done. Two wireline runs were required for the core because the GS pulling tool failed to engage the core barrel on the first attempt. A good 7-m core finally was recovered on the third attempt.

An RCB bit was deployed during this first phase of operation at Site 855, since the initial objective was to determine the geometry of the fault and to tag basement at each hole drilled, and to penetrate to bit destruction at the final hole. More detailed sampling would be done later if necessary with the advanced piston corer/extended core

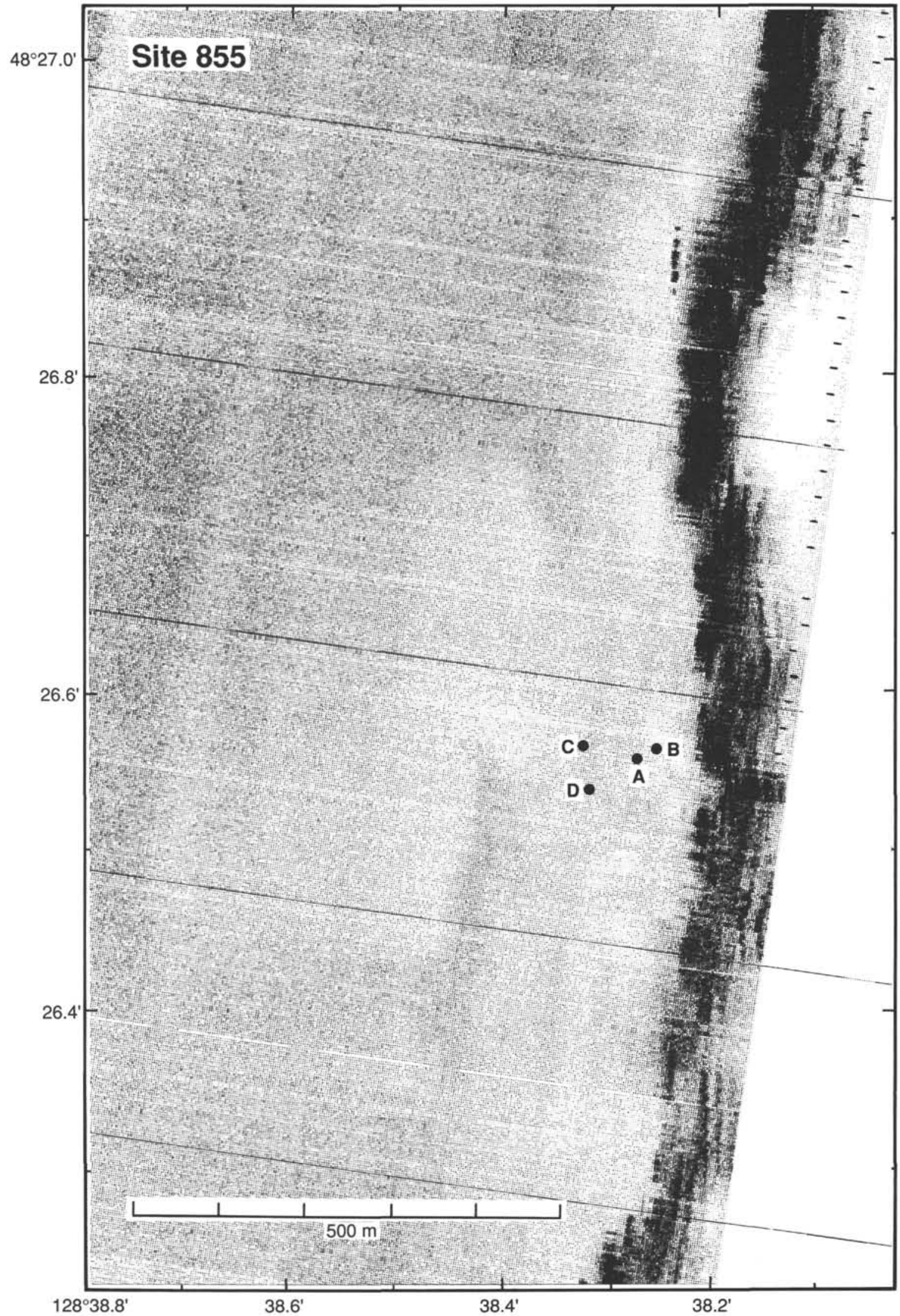

Figure 3. Deep-towed SeaMARC I side-scan acoustic imagery in the immediate vicinity of Site 855 (from Johnson et al., in press), with individual hole locations shown.

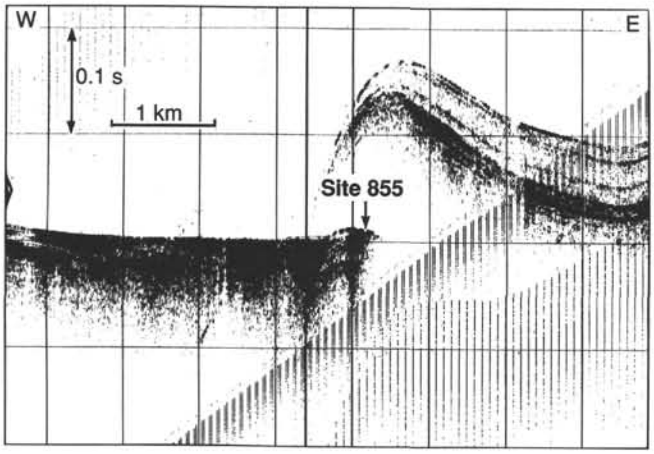

Figure 4. 3.5-kHz profile crossing the normal-fault scarp at the location of Site 855.

barrel (APC/XCB) system. The first three RCB cores were "punch cores" with no rotation or circulation used. It was necessary to rotate and "break circulation" on Core 139-855A-4R. Core recovery averaged 71% for the interval. At 35.5 mbsf, the first water-sampler temperature probe (WSTP) run was attempted. The run proceeded smoothly and a good water sample was collected, although the temperature measurement was unsuccessful as a result of an incorrectly wired battery pack.

Continuous circulation was required to penetrate and continue coring; recovery dropped to about 22% as a result. The rate of penetration decreased abruptly at 74 mbsf where rubbly basalt was encountered, and hole problems began immediately. Coring was terminated at 76.4 mbsf.

Hole 855B

The rig was offset 30 m to the east (toward the fault scarp) in order to intersect the sediment/basalt (fault?) interface at a higher stratigraphic level. The rig's weight indicator registered contact with the seafloor at 2457 m. RCB cores were taken, with spotty recovery, to 45 mbsf, where hard drilling was encountered. Drilling was uneven to about 53 mbsf, where the rocks became uniformly hard, although torquing tendencies persisted.

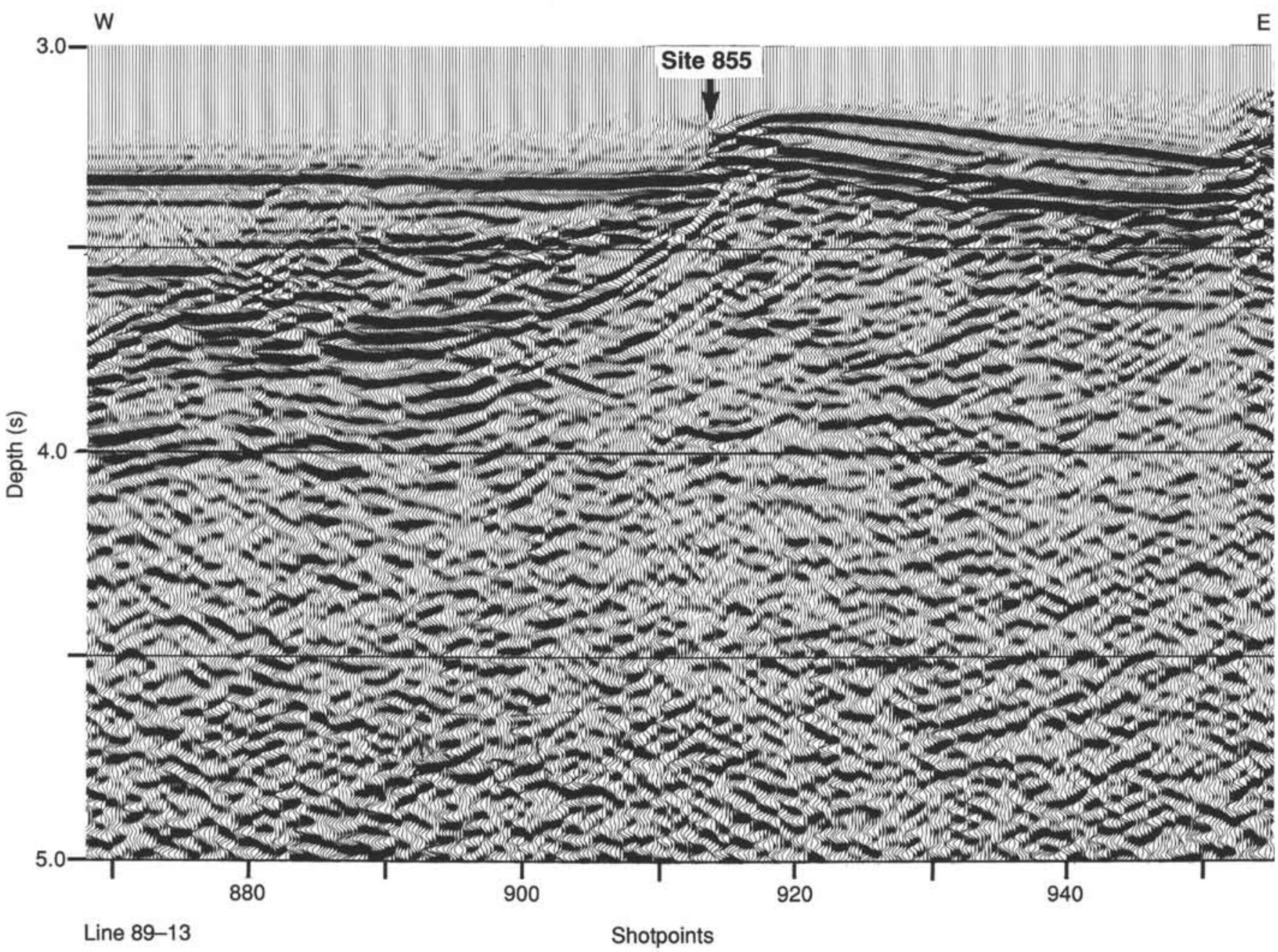

Figure 5. Detail of multichannel seismic reflection profile 89-13 crossing Site 855. Shotpoints are spaced 50 m apart.

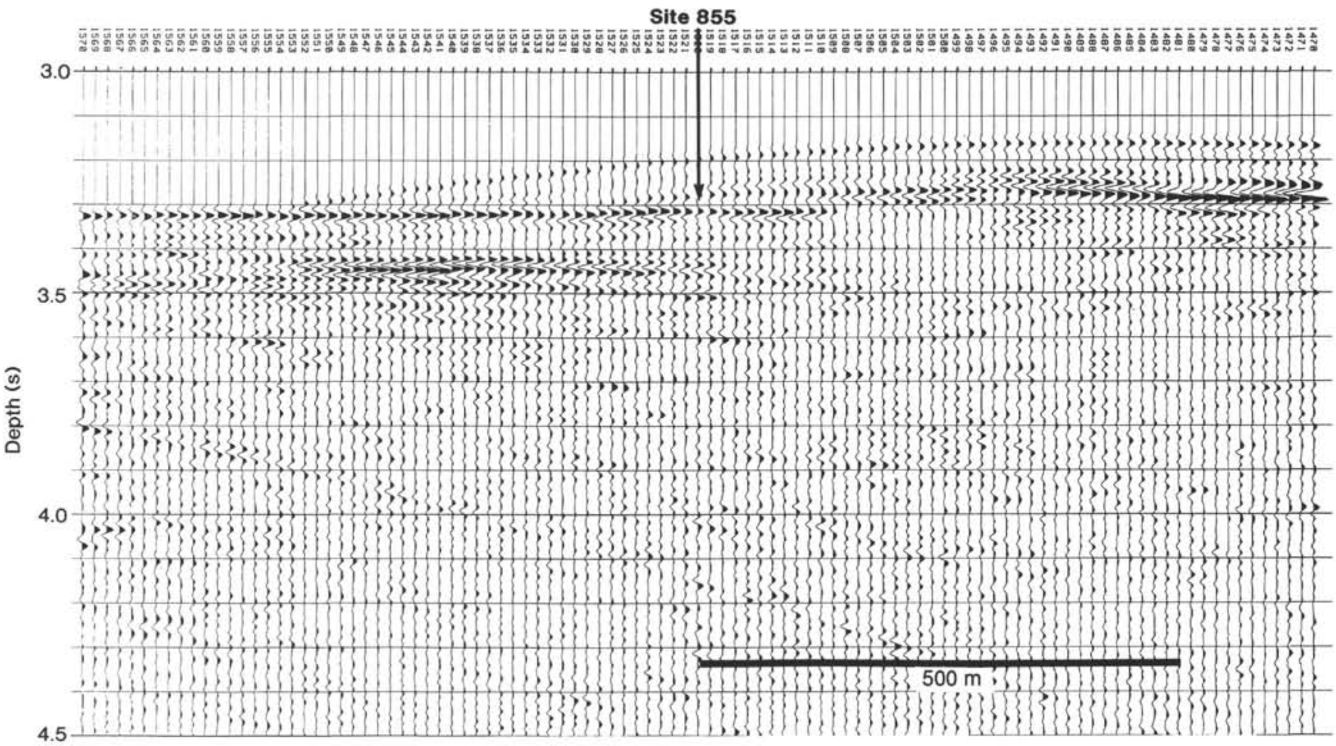

Figure 6. Near-trace display of multichannel seismic reflection line 89-13 over Site 855. Individual traces are spaced 12.5 m apart. (Plot provided by K. Rohr.)

Unfortunately, none of the transitional material was recovered and the only core recovered from below 45 mbsf was a handful of basalt "rollers" in what was to be the final core. Total depth of the hole was 63.3 mbsf.

The simplest interpretation of results of drilling to this point was that the basalt in both the 855A and 855B holes represented the foot wall of the normal fault, which had an apparent dip of about 45°. A location was chosen for Hole 855C that would allow for penetration of the fault where basalt occurred in both the hanging and foot wall. If penetration was adequate, a logging program would be carried out.

Hole 855C

When the bit had been pulled clear of the seafloor, we took up a new position 55 m west of Hole 855A. A jet-in test was conducted to determine the casing point for the reentry hole scheduled for Site 855 later in the leg. Without rotating the drill string, a depth of 57 mbsf was reached with a maximum circulation rate of 250 gallons per minute. Though further jetting would have been possible, the depth reached was adequate for the projected casing strings.

Upon spud-in on 17 July, the bit took weight at 2457 m. A nearly full core was recovered, however, and seafloor depth was fixed at 2454.5 m on the basis of core recovery. Core recovery was quite good to about 66 mbsf, where the requirement for circulation again caused a sharp decrease. WSTP runs were made at 37, 56, 75, and 95 mbsf. Good water samples were collected at 37 and 75 mbsf. Reliable temperatures were recorded at 56 and 75 mbsf.

Hard material was encountered at 98 mbsf, and drilling problems began shortly thereafter in the form of high and irregular torque, sticking tendencies, and a total lack of core recovery. Several meters of hole were lost whenever the bit was raised, and overpull of up to 100,000 lb was required to free the string. Various measures, including mud flushes and a core breaker, were used in attempts to clean the hole and recover rock samples. Drilling parameters over the 13-m sub-basement interval indicated a "rockpile" of cobble-to-boulder-sized pieces and no solid matrix. The only material recovered from three coring attempts in this interval was two small basalt pebbles found in the GS retrieving tool cup *on top of* the core barrel on which the core breaker was run.

The location of Hole 855C was unsatisfactory for a reentry cone installation, but a final attempt to find drillable "basement" was requested before abandoning the site as a reentry candidate. The bit was again pulled clear of the seafloor and the rig was offset 50 m to the south.

Hole 855D

Hole 855D was spudded on 18 July with the same indicated depth as Hole 855C. The hole was drilled without coring to 79.5 mbsf, where a WSTP run was made and a contaminated water sample was collected. Continuous RCB coring then began with the objective of resampling the lowermost sediments and coring into basalt to bit destruction.

No core recovery at all was achieved from the first two coring attempts. A review of the WSTP temperature data suggested either that the probe had not exited the core bit during the measurement run or that the probe cracked the formation on penetration. Also there had been no recovery from the final two coring attempts in Hole 855C. Although circulating pressures were normal, a mechanical obstruction was suspected. A bit deplugger was made up to an inner core barrel and pumped down the pipe. The first result was inconclusive, so the deplugger was deployed a second time. The marking chalk on the latch finger was undisturbed, showing clearly that the latch had not engaged the sleeve downhole.

As the hole had been drilled nearly to basalt, we decided to continue penetration to basement, even if core could not be collected, to determine the depth and drilling parameters of the basement. The inner core barrel (with a chalked latch) was pulled after 9.6 m. It showed signs of latching and contained 0.5 m of sediment core. The next core reached basement at 108 mbsf and also recovered some sediment. Two short cores in basement were attempted, but only a few "rollers" were recovered from each. The familiar torquing/sticking/

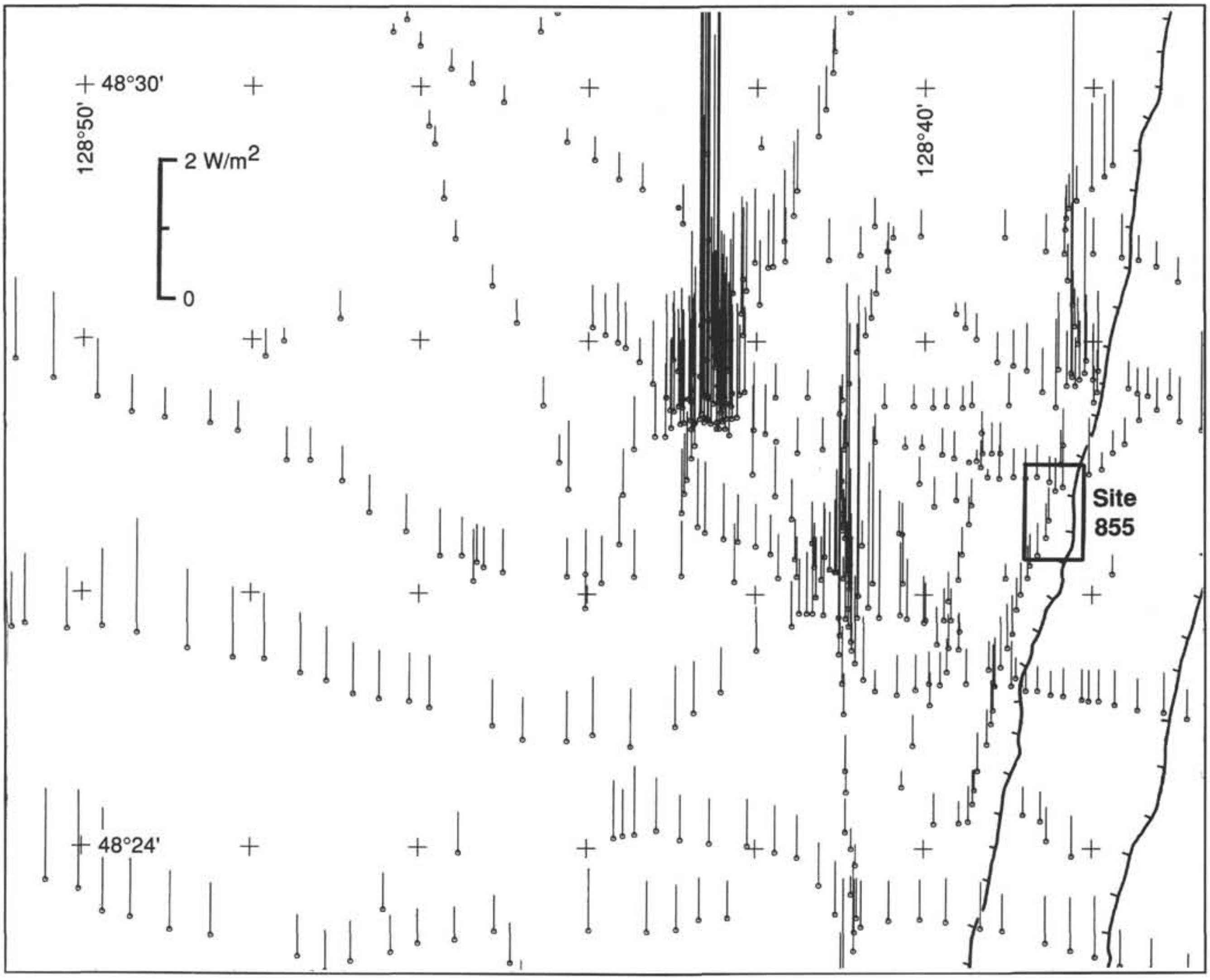

Figure 7. Heat flow in the part of Middle Valley occupied by Leg 139 (same area as in Fig. 2). Measurements were made along multipenetration lines running through the area. The quality of navigational control is variable; uncertainty of most measurement positions is about 100 m. The fault scarps imaged in the seismic reflection profiles and acoustic imagery (Figs. 2–6) are shown by the hachured lines. The area of Site 855 (shown in Fig. 3) is outlined.

filling tendencies returned, and operations were terminated at 118.6 mbsf. There was little chance of drilling a hole deep enough for logging and the site was clearly not suitable for a reentry installation.

The drill string then was recovered to the rig floor. No core pieces or mechanical problems were found with the bit or associated components that would explain the apparent blockage. It was concluded that some basalt core fragments had been blocking the bit or float valve cavity and that the deplugger had dislodged them. The bit showed considerable wear to its exterior from the basalt rubble and the mechanical bit release disconnect had been crushed in at the window band.

LITHOSTRATIGRAPHY AND SEDIMENTOLOGY

The four holes drilled at Site 855 are positioned in a line generally perpendicular to the eastern boundary fault of Middle Valley. Hole 855B is approximately 40 m from the fault scarp, Hole 855A is approximately 70 m from the scarp, and Holes 855C and 855D are approximately 125 m from the scarp. All of the holes were drilled with the RCB, resulting in badly disturbed sediment and poor recovery. Although the thickness of the sediment column varies from hole to hole, all of the holes are lithologically similar and only one lithostratigraphic unit is defined for the entire stratigraphic sequence. Hole 855C is used here as the "type section" because it is the deepest hole and because core recovery (54%) was the highest for the site.

Lithologic Unit I

Sections 139-855A-1R-1, 0 cm, to -8R-1, 16 cm (0 to 64.96 mbsf); 139-855B-1R-1, 0 cm, to -6R-CC, 0 cm (0 to 34.55 mbsf); 139-855C-1R-1, 0 cm, to -12R-CC, 0 cm (0 to 106.88 mbsf); 139-855D-1R-1, 0 cm, to -4R-CC, 28 cm (0 to 108.5 mbsf); Holocene to Pleistocene.

Lithologic Unit I comprises three major lithologies: dark greenish gray (5GY 4/1) clay, dark greenish gray (5GY 4/1) to dark gray (5Y 4/1) silty clay, and dark greenish gray (5BG 4/1) to gray (5Y 4/2) quartz-plagioclase sandy silt and silty sand. These lithologies comprise fining-upward sequences throughout the entire cored interval. The coarser grained intervals (silt and sand) are typically plagioclase-rich and commonly contain quartz, mica (predominantly biotite), and amphibole. All of the sampled intervals contain zircon. Pyrite, calcite, glauconite, and opaque minerals are present locally in small quantities. Biogenic components are present in most intervals and include foraminifers, diatoms, radiolarians, siliceous spicules, and nannofossils.

Sedimentary structures indicative of gravity-driven mass flows, along with a large assemblage of benthic foraminifers indigenous to the shelf and rare occurrences of shelf diatoms (see "Biostratigraphy" section, this chapter), suggest that much of this sediment was derived from the shelf. Hole 855C penetrated a minimum of 28 turbidite sequences characterized by sharp bases overlain by sand- and silt-size clastic material that grades to silty clay and to clay (Section 139-855C-7R-4; Fig. 8). The basal coarse fraction ranges from <10 to 116 cm thick, typically exhibits normal size grading, is locally massive, and contains rare planar laminations. This combination of sedimentary structures records deposition of Bouma "a" through "c" units. The overlying, commonly laminated, silty and clayey fractions record deposition of Bouma "c" and "d" units. Locally, pelagic Bouma "e" units can be distinguished from the underlying "d" units by a slight color change from dark greenish gray (5BG 4/1) turbiditic silty clays to greenish gray (5G 5/1) pelagic sediments. Both the "d" and the "e" units exhibit local bioturbation (Section 139-855C-7R-4; Fig. 9). Complete "a–e" turbidite sequences are uncommon in these cores. Sequences containing Bouma units "b" through "d" dominate the cored intervals. The overall thickness of the turbidite sequences ranges from 13 to 131 cm.

These turbidite intervals are also easily recognized on the magnetic susceptibility curves. Each barrel sheet from Site 855 contains a magnetic susceptibility plot. As illustrated in Figure 10, positive peaks on these plots correspond closely to the bases of the turbidite units.

BIOSTRATIGRAPHY

Sediment at Site 855 is largely turbiditic with intervening hemipelagic units that were strongly disrupted by rotary drilling. The drilling disturbance mixed a turbiditic fauna displaced from shallow water with the *in-situ* bathyal fauna, and even made distinction of lithologic units difficult (see "Lithostratigraphy and Sedimentology" section, this chapter). Sediment recovery at Hole 855A and 855C was generally poor except in the uppermost cores, and sediment recovery at Holes 855B and 855D was poor in all cores. Dissolution affected both foraminifers and calcareous nannofossils, particularly in the deep sequences (Table 3). The cored sequence at Hole 855D is similar in depth to Core 139-855C-11R (approximately 110 mbsf) and the calcareous nannofossil assemblage suggests that the base of Hole 855D could be older than those at Holes 855A, 855B, and/or possibly 855C.

Foraminifers

The planktonic foraminiferal fauna (Table 4) bears species typical of subarctic waters and includes *Globigerina bulloides* d'Orbigny, *Globigerinita glutinata* (Egger), *Globigerinita minuta* (Natland), *Globigerinita uvula* (Ehrenberg), sinistral and dextral *Neogloboquadrina pachyderma* (Ehrenberg), *Tenuitella iota* (Parker), *Tenuitella parkerae* (Brönnimann and Resig), and *Turborotalita quinqueloba* (Natland). Distinct specimens of *Turborotalita clarkei* (Rögl and Bolli) were recognized occasionally, but because they are difficult to distinguish from *Turborotalita quinqueloba* without SEM examination, the two taxa were grouped together as *Turborotalita quinqueloba*. Transitional species occur rarely in the sequence and include *Orbulina universa* d'Orbigny, *Neogloboquadrina dutertrei* (d'Orbigny), and *Globorotalia scitula* (Brady), and a subtropical species, *Globorotalia theyeri* Fleisher, also occurs rarely. No distinct faunal change could be detected by qualitative observation except for the coiling change in *Neogloboquadrina pachyderma*. The abundance of planktonic foraminifers, however, is consistently high in Holocene samples, whereas their abundance is low in some Pleistocene samples in which mineral grains dominate (Tables 3 and 4).

The Holocene-Pleistocene boundary was recognized in two of four holes using the relative frequency of dextral to sinistral *Neogloboquadrina pachyderma* (Bandy, 1960; Table 5). The dextral form occurs commonly in Samples 139-855A-1R-1, 0–1 cm, 139-855A-1R-CC, and 139-855C-1R-1, 0–1 cm, and is rare or absent from deeper core-catcher samples. Sinistral *Neogloboquadrina pachyderma* occurs abundantly throughout this interval. The three samples are assigned to Zone CD1, and all other fossiliferous samples are tentatively assigned to Zone CD2 (Lagoe and Thompson, 1988).

The bathyal benthic assemblage changes markedly at the Holocene-Pleistocene boundary (Table 4). The Holocene fauna includes *Hoeglundina elegans* and *Uvigerina dirupta*, whereas the Pleistocene fauna contains *Melonis*. The Holocene fauna contains few or no taxa reworked from the continental shelf, whereas the Pleistocene fauna contains numerous specimens from the shelf, especially in samples that contain abundant mica and other sand-size mineral grains of presumed turbiditic origin. Reworked taxa include *Buliminella elegantissima, Cassidulina reniformis, Elphidium excavatum* and other *Elphidium* species, *Epistominella pacifica, Nonionella, Nonion,* and *Rosalina.*

The faunal changes in both benthic and planktonic foramini-fers near the Holocene-Pleistocene boundary suggest that environmental conditions on the seafloor at 2455 m changed between the last glacial and interglacial stages.

Calcareous Nannofossils

With few exceptions, shipboard descriptions of nannofossils were limited to core-catcher samples. Calcareous nannofossils are rare to abundant within 26 cores recovered from Holes 855A, 855B, 855C, and 855D. The remaining core-catcher samples, except Sample 139-855D-4R-CC, which is barren of nannofossils, were either not recovered or were hard rock. In general, the calcareous nannofossils recovered from this site are poorly preserved and exhibit a high degree of etching and dissolution. The fossil assemblages are low in diversity with only one to 11 species including *Emiliania huxleyi, E. pujosae, Gephyrocapsa oceanica, G. caribbeanica, Calcidiscus leptoporus, Coccolithus pelagicus, Braarudosphaera bigelowii, Syracosphaera pulchra, Pontosphaera japonica, Umbilicosphaera sibogae, Rhabdosphaera claviger,* and *Thoracosphaera* sp. (Table 6).

The marker species of Zone NN21, *Emiliania huxleyi,* was encountered in most samples from Holes 855A, 855B, and 855C, and the nannofossil assemblages were, therefore, assigned to the lower part of Zone NN21 of Martini (1971). The age of the sections is, therefore, latest Pleistocene to Holocene. *E. huxleyi* occurs in low abundance in most core-catcher samples at this site, but is common in abundance in a few core-catcher samples from the upper sections of Holes 855A and 855C. Shore-based study will determine whether or not the *E. huxleyi* Acme Zone is present at the top of the sequences. *Emiliania huxleyi* is absent from Samples 139-855A-4R-CC, 139-855A-6R-CC, 139-855A-7R-CC, 139-855C-4R-CC, 139-855C-8R-CC, 139-855C-10R-CC, and 139-855C-11R-CC, and was probably removed by dissolution. Hole 855D had very low recovery, and nannofossils were found only in Sample 139-855D-3R-CC. The fossil assemblage, including poorly preserved *Gephyrocapsa oceanica, G. caribbeanica,* and *Coccolithus pelagicus,* falls into Zones NN19–21. The sediments from Hole 855D are, therefore, late Pleistocene in age and cannot be assigned to a subdivision of the pleistocene.

Species of small *Gephyrocapsa oceanica* usually dominate the nannofossil assemblages and occur in every sample. They are usually 3–4 μm in size. *Coccolithus pelagicus* is the second most abundant species, and shows the most resistance to dissolution. Fossils reworked from pre-Pleistocene sediments are rare, and occur only in Samples 139-855A-3R-CC, 139-855A-6R-CC, 139-855C-4R-CC, and 139-855C-10R-CC. They are *Cruciplacolithus tenuis, Sphenolithus heteromorphus,* and *Discoaster* sp.

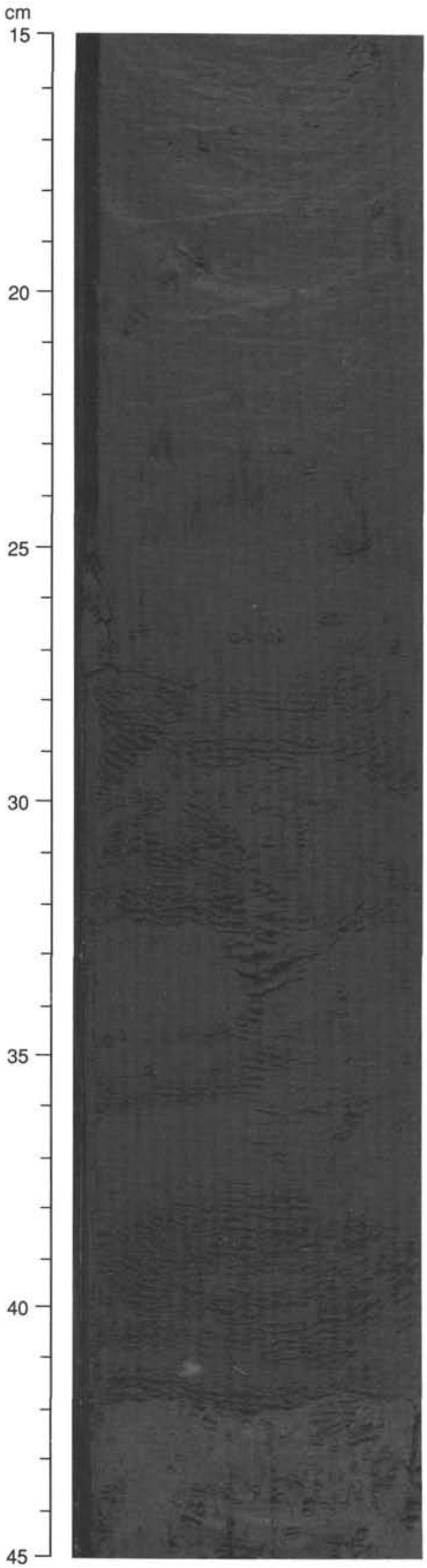

Figure 8. Typical sharp-based fining-upward turbidite sequence at Site 855 (interval 139-855C-7R-4, 15–45 cm).

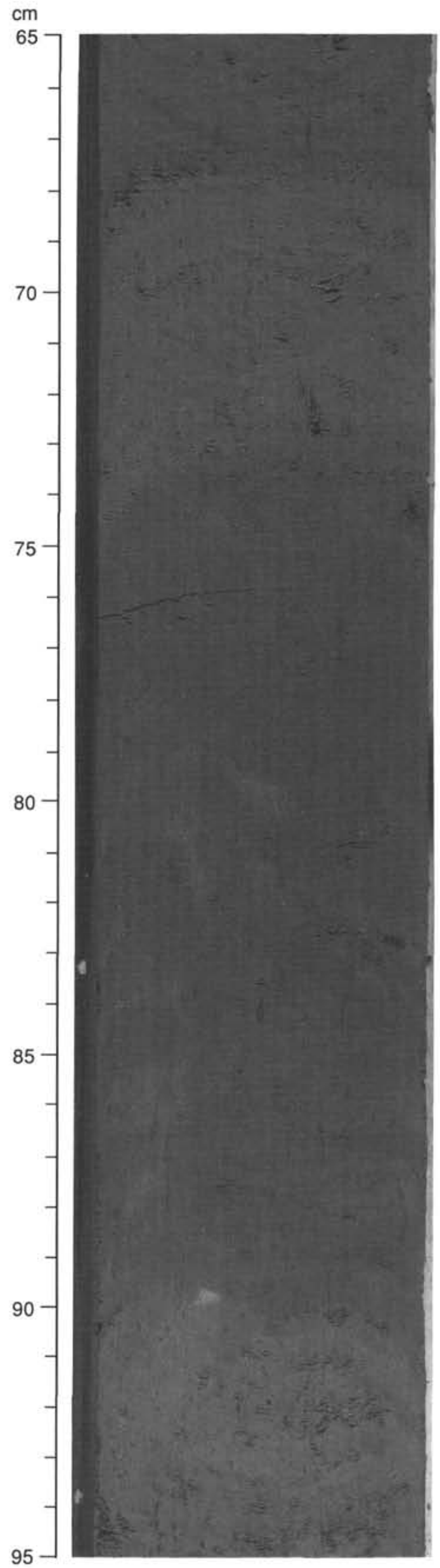

Figure 9. Bioturbation in "d" (darker sediment: interval 139-855C-7R-4, 74–90 cm) and "e" (interval 139-855C-7R-4, 68–74 cm) turbidite intervals.

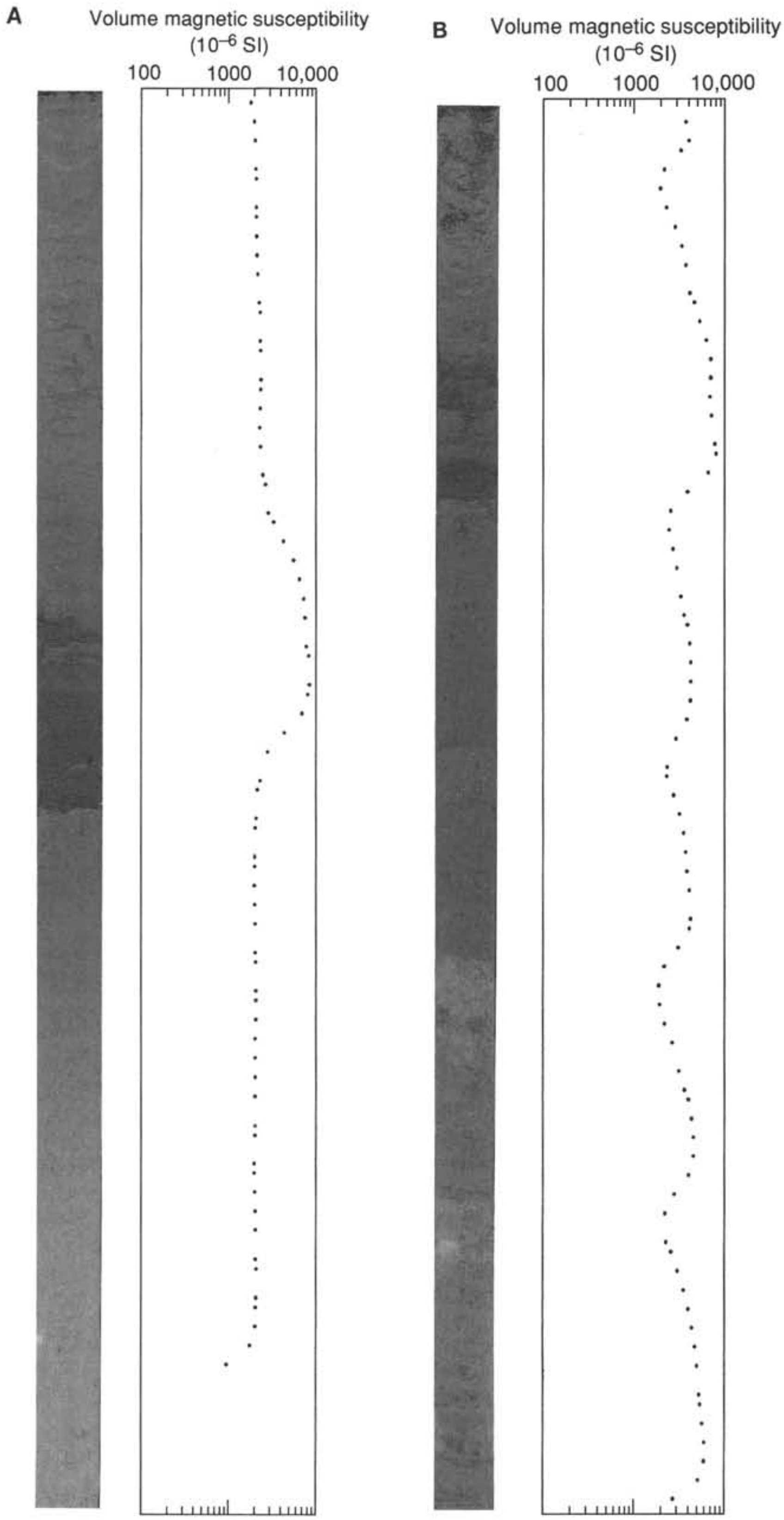

Figure 10. Relationship between magnetic susceptibility plots and core at Site 855. **A.** Strong positive peaks correspond to the sharp grain-size change that marks the contact between two turbidite units (Section 139-855C-10R-4). **B.** Note the weak positive deflection of the curve through the mixed grain-size (bioturbated) sections (Section 139-855C-7R-4).

Table 3. Comparison of abundances of calcareous nannofossils, planktonic foraminifers, and benthic foraminifers to lithology of sample.

Sample (cm)	Lithology	Nannofossil abundance	Benthic foraminifer abundance	Planktonic foraminifer abundance
139-855A-				
1R-1, 0–1	Silty clay	A	A	A
1R-CC	Disturbed clay	A	A	A
2R-CC	Disturbed clay	C	A	A
3R-CC	No description	C	A	A
4R-CC	Silt and silty clay	F	A	A
5R-CC	Clay with silt patches	C	C	F
6R-CC	Clay	F	R	R
7R-CC	Silt and silty clay	C	R	R
8R-CC	Silty clay with sand	A	C	C
139-855B-				
2R-1, 0–1	Silty clay	C	A	A
2R-CC	Silty clay	C	A	A
4R-CC	Silty clay	R	F	F
5R-CC	Silty clay	F	R	F
6R-CC	Clay	F	A	A
139-855C-				
1R-1, 0–1	Silty clay	A	A	A
1R-CC	Silty clay	F	F	A
2R-CC	Silty clay	A	C	A
3R-CC	Clayey silt	C	F	A
4R-CC	Silt	F	C	A
5R-CC	No description	A	A	A
6R-CC	Clayey silt	C	F	R
7R-CC	Graded silty clay	F	R	F
8R-CC	Clay	R	B	B
9R-CC	Disturbed clay	C	C	R
10R-CC	Clay	C	R	R
11R-CC	Silty clay	R	R	F
139-855D-				
3R-CC	Disturbed silt	R	R	R
4R-CC	Moderately indurated clay	B	B	B

Note: A = abundant, C = common, F = few, R = rare, B = barren.

Comparison

We compared the abundance of foraminifers to that of calcareous nannofossils (Table 3). Foraminifers in general were preserved in greater abundance than calcareous nannofossils in this environment. Of 29 samples inspected for fossils, 15 bore abundant foraminifers, whereas only six bore abundant calcareous nannofossils. Abundance did not correlate between the two groups of microfossils. For example, when foraminifers were rare, calcareous nannofossils were both common and rare. Calcareous nannofossils were abundant in the three samples assigned to the foraminiferal Holocene Zone CD1, whereas they are mostly common to rare in Pleistocene samples.

We compared the zonal assignments based on foraminifers to that based on calcareous nannofossils (Table 5). An assemblage change in the planktonic foraminifers delimits the Holocene-Pleistocene boundary, but no floral change is noted in the calcareous nannofossils despite the change from glacial to interglacial conditions. The calcareous nannofossil zonation suggests that the sequence in Hole 855D may be older than those of the other holes, a conclusion consistent with its slightly greater depth in the sedimentary sequence. A note of caution is appropriate at this point. The foraminiferal assemblage is too poorly preserved to make a zonal assignment to confirm the nannofossil biostratigraphy. In addition, the similarity of the calcareous nannofossil flora to that expected in Zone NN20 may be an artifact of poor preservation.

PALEOMAGNETISM

Middle Valley is a young rift valley sedimented by a thick layer of turbidites. The high sedimentation rate in this area permitted collection of detailed paleomagnetic data suitable for the study of geomagnetic secular variations and excursions. As the thermal gradient through the sediments at Site 855 is the lowest among the sites drilled during Leg 139, the degree of sediment hydrothermal alteration is considered to represent an "unaltered background" (see "Lithostratigraphy and Sedimentology" section, this chapter). Unfortunately for paleomagnetic study, the four holes at Site 855 were rotary cored, and so the cores are highly disturbed.

The natural remanent magnetization (NRM) and the magnetization after alternating field (AF) demagnetization were measured on the archive half of the cores from Holes 855A, 855B, and 855C using the pass-through cryogenic magnetometer. Demagnetization steps on archive halves were at 5, 10, and 15 mT for most of the samples. Pass-through measurements were taken at intervals of 2 cm from Cores 139-855C-1R to 139-855C-4R and 10 cm for other core samples. Eleven discrete samples were taken from undisturbed silty parts of cores from the working half of the three holes. These samples were progressively demagnetized in 9–12 steps using the Schonstedt AF demagnetizer and measured with the Molspin spinner magnetometer. Magnetic susceptibility of all the cores was measured on the multisensor track (MST) at 2-cm intervals before splitting.

Remanent Magnetization

Figure 11 shows downhole profiles of NRM for Holes 855A, 855B, and 855C. The NRM intensities are consistently high, ranging from 10 to 100 mA/m. The high intensity is thought to come from high concentrations of fine-grained titanomagnetite deposited within turbidites. The extremely high intensity from 0 to 3 mbsf in Hole 855A may have resulted from rust from the pipe falling onto the core. Paleomagnetic results after 15-mT AF demagnetization for Holes 855A, 855B, and 855C are shown in Figures 12, 13, and 14. The intensity of magnetization does not change significantly after demagnetization to 15 mT. Typical demagnetization diagrams for the discrete samples are shown in Figure 15, and the direction of primary component and median destructive field (MDF) of all the discrete samples are listed in Table 7. In general, remanent magnetization is stable against AF demagnetization, and the MDF of all the samples is 23–30 mT.

As the RCB cores were twisted and disturbed by drilling, the declination of magnetization was highly disrupted. The inclination also seems to be disrupted, although histograms of inclination for three holes (Fig. 16) show peaks around 50°–70°, which is consistent with the inclination expected from the axial dipole field at this site (67°). Although negative inclination values could be records of real geomagnetic excursions (e.g., Hole 855C, 21–22 mbsf, 27–28 mbsf; Fig. 17), we failed to correlate those zones showing anomalous directions between the three holes because core recovery was poor and the paleomagnetic records were noisy. Progressive AF demagnetization data on discrete samples with negative inclination show that remanent magnetization is stable (Fig. 15B, 15D). However, mechanical deformation on sediment cores possibly produced stable remanent magnetization in anomalous directions (Hays et al., 1969). We could not detect reliable evidence of geomagnetic excursions from the paleomagnetic results of RCB cores at Site 855.

Magnetic Susceptibility

Magnetic susceptibility is shown together with magnetization intensity in Figures 12, 13, and 14. High magnetic susceptibility of about 2×10^{-3} (SI units) is consistent with the high remanent magnetization intensity in the cores. These profiles are composed of many peaks, which are well-correlated with the presence of turbidites. High concentrations of coarse-grained, multidomain magnetite in the basal plane are thought to contribute to high magnetic susceptibility. The magnetic susceptibility does not always correlate positively with the intensity of magnetization (Fig. 17), because magnetic susceptibility

Table 4. Range chart of planktonic and benthic foraminifers grouped as textularids, miliolids, and rotalids, their abundance and preservation, and abundance of other major constituents of the sand-size fraction.

Sample	Abundance of benthic foraminifers	Abundance of planktonic foraminifers	Preservation of foraminifers	*Globigerina bulloides*	*Globigerina quinqueloba*	*Globigerinita glutinata*	*Globigerinita minuta*	*Globigerinita uvula*	*Globorotalia scitula*	*Globorotalia theyeri*	*Neogloboquadrina dutertrei*	*Neogloboquadrina pachyderma* (dex.)	*Neogloboquadrina pachyderma* (sin.)	*Orbulina universa*	*Tenuitella iota*	*Tenuitella parkerae*	*Ammodiscus* sp. A	*Eggerella bradyi*	*Miliammina* sp. A	*Saccammina* sp. A	*Spirosigmoilina tenuis*	*Spirosigmoilinella* (?)	*Miliolina* spp.	*Pyrgo murrhina*	*Pyrgo* spp.
139-855A-																									
1R-1, 0–1	A	A	G	A	C	R	R	-	F	-	-	C	A	-	-	-	X	-	-	X	-	-	-	X	-
1R-CC	A	A	M	A	F	F	F	F	F	-	-	C	A	R	-	-	-	-	-	-	-	-	-	X	-
2R-CC	A	A	M	A	C	-	-	-	-	-	-	-	A	-	-	-	-	-	-	-	-	-	-	-	-
3R-CC	A	A	M	A	C	R	F	R	-	-	-	-	A	-	-	-	-	-	-	-	-	X	-	X	-
4R-CC	A	A	M	A	R	R	-	R	R	-	-	-	A	-	-	-	-	-	X	-	-	-	X	-	-
5R-CC	C	F	M	F	-	-	-	-	-	-	-	-	F	-	-	-	-	-	-	-	-	-	X	-	-
6R-CC	R	R	P	-	R	-	-	-	-	-	-	-	R	-	-	-	-	-	-	-	-	-	-	-	-
7R-CC	R	R	G	R	-	R	-	-	-	-	-	-	R	-	-	-	-	-	-	-	-	-	-	-	-
8R-CC	C	C	G	C	R	R	F	F	R	-	-	R	C	-	R	-	-	X	-	-	-	-	-	-	-
139-855B-																									
2R-1, 0–1	A	A	M	A	R	-	-	R	-	-	-	-	A	-	R	-	-	-	-	-	X	-	-	-	-
2R-CC	A	A	P	A	C	R	-	R	-	-	-	-	A	-	-	-	-	-	-	-	-	-	-	-	-
4R-CC	F	F	M	F	F	-	R	R	R	-	-	R	F	-	-	-	-	-	-	-	-	-	-	-	-
5R-CC	R	F	G	-	R	-	R	-	-	-	-	R	F	-	-	-	-	-	-	-	-	-	-	-	-
6R-CC	A	A	P	A	-	-	-	-	-	-	-	-	A	-	-	-	-	X	-	-	-	-	-	-	-
139-855C-																									
1R-1, 0–1	A	A	G	A	C	C	-	-	R	R	R	C	A	R	-	R	-	-	-	-	-	-	-	X	-
1R-CC	F	A	G	A	C	C	C	-	-	R	-	R	A	-	-	-	-	-	-	-	-	-	-	-	-
2R-CC	C	A	M	A	A	R	-	-	R	-	-	-	A	-	-	-	-	-	-	-	-	-	-	-	-
3R-CC	F	A	G	C	A	C	-	R	R	-	-	-	A	-	-	-	-	X	-	-	-	-	-	-	-
4R-CC	C	A	M	A	C	-	C	-	-	-	-	-	A	-	-	-	-	-	-	-	-	-	-	-	-
5R-CC	A	A	M	A	R	-	R	-	-	-	-	-	A	-	-	-	-	-	-	-	-	-	-	-	X
6R-CC	F	R	M	-	-	R	-	-	-	-	-	-	R	-	-	-	-	-	-	-	-	-	-	-	-
7R-CC	R	F	M	F	-	-	-	-	-	-	-	-	F	-	-	-	-	-	-	-	-	-	-	-	-
8R-CC	B	B	—	-	-	-	-	-	-	-	-	-	-	-	-	-	-	-	-	-	-	-	-	-	-
9R-CC	C	R	G	R	-	-	-	R	-	-	-	-	R	-	-	-	-	-	-	-	-	-	-	-	-
10R-CC	R	R	P	-	R	-	-	-	-	-	-	-	R	-	-	-	-	-	-	-	-	-	-	-	-
11R-CC	R	F	G	F	R	R	R	-	R	-	-	-	F	-	-	-	-	-	-	-	-	-	-	-	-
139-855D-																									
3R-CC	R	R	G	-	-	-	R	-	-	-	-	-	R	-	-	R	-	-	-	-	-	-	-	-	-
4R-CC	B	B	—	-	-	-	-	-	-	-	-	-	-	-	-	-	-	-	-	-	-	-	-	-	-

Note: A = abundant, C = common, F = few, R = rare, B = barren, G = good preservation, M = moderately good preservation, P = poor preservation, X = present.

is thought to depend on the fraction of multidomain magnetite, whereas intensity of magnetization mainly depends on the geomagnetic field strength at the time of deposition and on the concentration of fine-grained, single-domain magnetite, which has higher coercivity.

FLUID GEOCHEMISTRY

Four holes were drilled at Site 855 on the eastern side of the Middle Valley rift to ascertain whether the eastern boundary fault is a conduit through which seawater enters basement. Fluid flow could be either focused along the fault itself, distributed through the igneous layer that is exposed by faulting on the upthrown block, or distributed through the relatively thin sediment layer at this site. If seawater is flowing into basement along the fault at a volumetric rate that is large relative to transport across the sediment-basement interface or to reaction in basement, then the fluid in basement should resemble bottom seawater. In this case, the composition of sediment pore water should approach that of bottom seawater as the fault or basement is approached.

Holes 855A and 855B penetrated the fault plane at 74 and 45 mbsf, respectively, where sediment in the downthrown hanging-wall block to the west is in contact with basalt in the upthrown foot-wall block to the east. Holes 855C and 855D penetrated basalt (basement?) at 98 and 108 mbsf, respectively, in the hanging-wall block, a few tens of meters above the fault plane.

Results and Discussion

Interstitial water was collected from sediment from all four holes at Site 855 (Table 8). Holes 855A and 855C provided the most comprehensive profiles, with sample intervals less than 10 m; samples also were collected from within the uppermost meter of the sediment column and generally within 10 m of the sediment-basalt interface.

Table 4 (continued).

Sample	*Quinqueloculina* spp.	*Triloculina*	*Bolivina pacifica*	*Bolivina seminuda*	*Bolivina* spp.	*Bulimina inflata*	*Bulimina rostrata*	*Buliminella elegantissima*	*Buliminella tenuata*	*Cassidulina cushmani*	*Cassidulina norcrossi*	*Cassidulina reniformis*	*Cassidulinoides* spp.	*Chilostomella oolina*	*Cibicides fletcheri*	*Cibicides kullenbergi*	*Cibicides mckannai*	*Cibicides wuellerstorfi*	*Cibicides* spp.	*Cibicidoides* sp. A	*Dentalina* sp. A	*Elphidium excavatum*	*Elphidium* spp.	*Epistominella exigua*
139-855A-																								
1R-1, 0–1	-	-	-	-	-	-	-	-	-	X	-	-	-	X	-	-	-	X	-	-	-	-	-	-
1R-CC	-	-	X	-	-	X	X	-	-	X	-	-	-	-	-	X	-	-	-	-	-	-	-	-
2R-CC	-	X	-	-	-	-	-	-	X	-	-	-	-	X	-	X	-	-	-	X	-	-	-	-
3R-CC	-	-	X	-	X	-	-	-	-	-	-	-	X	X	-	-	-	-	-	-	-	-	-	-
4R-CC	-	-	-	-	-	-	-	-	-	-	-	-	-	-	-	-	-	-	X	X	-	-	-	-
5R-CC	-	-	-	X	-	-	-	-	-	-	-	-	-	X	-	-	-	X	-	-	-	-	-	-
6R-CC	-	-	-	X	-	-	-	-	-	-	-	-	-	-	-	-	-	-	-	-	-	-	-	-
7R-CC	-	-	-	-	-	-	-	-	-	-	-	-	-	-	-	-	-	-	-	X	-	-	-	-
8R-CC	-	-	-	-	-	X	-	-	-	-	-	-	-	-	-	X	-	-	X	-	-	-	-	-
139-855B-																								
2R-1, 0–1	-	-	-	-	-	-	-	-	X	-	-	-	X	-	-	-	-	-	-	X	-	X	-	-
2R-CC	-	-	X	-	-	-	-	-	-	-	-	-	-	X	-	-	X	X	-	-	-	X	-	-
4R-CC	-	-	-	-	X	-	-	-	-	-	-	-	-	-	-	-	-	-	-	-	-	-	-	-
5R-CC	-	X	-	-	-	-	-	-	-	-	-	-	-	-	-	-	-	-	-	X	-	X	-	-
6R-CC	-	-	-	-	-	-	-	-	-	-	-	-	-	X	-	-	-	-	-	-	-	-	-	-
139-855C-																								
1R-1, 0–1	-	-	-	-	-	X	-	-	-	-	-	-	-	X	X	X	-	-	-	-	-	-	-	-
1R-CC	-	X	X	-	-	-	-	-	-	-	-	-	-	-	-	-	-	X	-	-	-	-	-	-
2R-CC	-	X	-	-	-	-	-	-	-	-	-	-	-	-	X	-	-	X	-	-	-	-	-	-
3R-CC	-	-	-	-	-	-	-	-	-	-	-	-	-	-	-	-	-	-	-	X	-	-	-	-
4R-CC	X	-	-	-	-	-	-	-	-	-	-	X	-	-	-	-	-	-	-	X	-	-	-	X
5R-CC	-	X	-	-	X	-	-	-	-	-	-	-	-	-	-	X	-	X	-	-	-	-	-	-
6R-CC	-	-	-	-	-	-	-	-	-	-	-	-	-	-	-	-	-	-	-	-	-	-	X	-
7R-CC	-	-	-	-	-	-	-	-	-	-	-	-	-	-	-	-	-	-	-	X	-	-	-	-
8R-CC	-	-	-	-	-	-	-	-	-	-	-	-	-	-	-	-	-	-	-	-	-	-	-	-
9R-CC	-	-	-	-	-	-	-	X	-	-	-	-	-	-	-	-	-	-	-	-	-	X	X	-
10R-CC	-	-	-	-	-	-	-	-	-	-	-	-	-	-	-	-	-	-	-	-	-	-	-	-
11R-CC	-	-	-	-	-	-	-	-	-	-	-	-	-	-	-	-	-	-	-	-	-	-	X	-
139-855D-																								
3R-CC	-	-	-	-	-	-	-	X	-	-	-	-	-	-	-	-	-	-	-	-	-	-	-	-
4R-CC	-	-	-	-	-	-	-	-	-	-	-	-	-	-	-	-	-	-	-	-	-	-	-	-

Several samples collected *in situ* with the WSTP have compositions similar to those of waters squeezed from samples collected at similar depths. Only four samples were obtained from Hole 855B and two from Hole 855D.

Concentrations of all of the ions measured change with depth, from bottom-seawater values at the seafloor to a maximum or a minimum at 10 to 70 mbsf (Figs. 18 to 20). With increasing depth below the maximum or minimum, concentrations gradually return to bottom-seawater values as basalt is approached. In the upper part of the sediment column, above the maximum or minimum, the change in the composition of pore water from a bottom-seawater end-member is caused by degradation of organic matter, alteration of detrital silicates, recrystallization of biogenic carbonates and silicates, and diffusion resulting from a glacial-to-interglacial change in the composition of bottom seawater (McDuff, 1985). In the lower part of the sediment column, the gradient with depth in the concentration of a given dissolved species depends on the rate of reaction of that species in the sediment, relative to its rate of diffusion.

The concentration of sulfate in pore water decreases with depth to a minimum value between 10 and 20 mbsf, then returns to the bottom-seawater value near the sediment-basalt interface (Fig. 18). The decrease in sulfate is caused by bacterial degradation of organic matter employing sulfate as an oxidant. The increase in concentration with depth below the sulfate minimum requires a source of sulfate at or near the sediment-basalt interface. No sulfate-bearing minerals were observed in these cores. The most likely source of sulfate is therefore a diffusive flux from pore water in the underlying basalt. Because the concentration of sulfate in the sediment pore water approaches that in bottom seawater as the basalt is approached, we suggest that the pore water in the underlying basalt has a sulfate concentration that is equal to that of bottom seawater.

Profiles of alkalinity and ammonium mirror profiles of sulfate (Figs. 18 and 20) and display a maximum in the upper 10 to 30 m of the sediment column. Concentrations of these dissolved species are changed from those in seawater mainly by bacterial degradation of organic matter, but also by dissolution and precipitation reactions, surface adsorption, and diffusion.

Profiles of phosphate are similar to those of alkalinity and ammonium (Figs. 18 and 20). Differences among these profiles represent differences in the rate of reaction in the lower portion of the sediment column and

Table 4 (continued).

Sample	*Epistominella pacifica*	*Epistominella* cf. *E. vitrea*	*Epistominella* sp. A	*Epistominella* sp. B	*Eponides turgida*	*Gavelinopsis* (?)	*Globobulimina affinis*	*Globobulimina ovula*	*Globobulimina pacifica*	*Globobulimina* spp.	*Globocassidulina* spp.	*Gyroidina altiformis*	*Gyroidina planulata*	*Gyroidina quinqueloba*	*Gyroidina* spp.	*Hoeglundina elegans*	Lagenids	*Lenticulina*	*Melonis barleeanum*	*Melonis pompilioides*	*Nonion labradorica*	*Nonion* spp.	*Nonionella digitata*	*Nonionella* cf. *N. miocenica*	*Nonionella stella*
139-855A-																									
1R-1, 0–1	-	-	-	-	-	-	X	-	-	-	-	-	-	-	-	X	-	-	-	-	-	-	-	-	-
1R-CC	-	-	-	-	-	-	X	-	-	-	-	-	-	-	X	X	X	-	-	-	-	-	-	-	-
2R-CC	-	-	-	-	-	-	X	-	X	-	X	-	X	-	-	-	X	-	-	X	-	-	-	-	X
3R-CC	-	-	-	-	X	-	-	-	-	-	-	-	X	X	X	-	-	-	-	X	-	-	-	-	-
4R-CC	-	-	X	-	X	-	-	-	-	-	X	X	-	X	X	-	X	X	-	X	-	-	-	-	-
5R-CC	-	-	X	X	X	-	X	-	X	-	X	-	-	X	X	-	X	-	X	-	-	-	-	-	-
6R-CC	-	-	-	-	X	-	-	-	-	-	-	X	-	-	-	-	-	-	-	-	-	-	-	-	-
7R-CC	-	-	-	-	-	-	-	-	X	-	-	-	X	-	-	-	-	-	-	-	-	-	-	-	-
8R-CC	-	-	-	-	-	-	-	-	X	-	-	X	X	-	X	-	X	-	-	X	-	-	-	-	-
139-855B-																									
2R-1, 0–1	-	-	-	-	X	-	X	-	X	-	-	-	-	-	X	-	-	-	-	X	-	-	-	-	-
2R-CC	-	-	-	-	-	-	X	-	X	-	X	-	X	X	X	-	-	-	-	X	X	-	-	-	-
4R-CC	-	-	-	-	-	-	-	-	-	-	X	-	-	-	X	-	X	-	-	-	-	-	-	-	-
5R-CC	-	-	-	-	X	-	-	-	-	-	X	-	-	X	-	-	-	-	-	-	-	-	-	-	-
6R-CC	-	-	X	-	-	-	X	-	-	-	-	-	-	-	-	-	X	-	-	X	-	-	-	-	-
139-855C-																									
1R-1, 0–1	-	-	-	-	-	-	-	X	X	-	-	X	X	-	-	X	-	-	-	-	-	-	-	-	-
1R-CC	-	-	-	-	-	-	X	-	-	-	-	-	X	-	-	-	-	-	-	-	-	-	-	-	-
2R-CC	-	-	-	-	-	-	X	X	-	-	-	X	X	-	-	-	X	-	-	X	-	-	-	-	-
3R-CC	-	-	-	-	X	-	-	X	X	-	X	-	X	-	X	-	X	-	-	X	-	-	-	-	-
4R-CC	-	-	-	-	X	-	-	X	-	-	X	-	X	-	-	-	-	-	X	X	-	-	-	X	-
5R-CC	-	X	-	-	X	X	-	X	-	-	-	-	X	-	X	-	X	-	X	X	-	-	-	-	-
6R-CC	-	-	-	-	-	-	-	-	-	-	-	-	-	-	-	-	X	-	-	-	-	-	-	-	-
7R-CC	-	-	-	-	-	-	-	-	-	-	-	-	-	-	-	-	-	-	-	-	-	-	-	-	-
8R-CC	-	-	-	-	-	-	-	-	-	-	-	-	-	-	-	-	-	-	-	-	-	-	-	-	-
9R-CC	X	-	-	-	X	-	-	-	-	X	-	-	-	-	-	-	X	-	-	-	-	-	X	-	-
10R-CC	-	-	-	-	-	-	-	-	-	-	X	-	-	-	-	-	-	-	-	-	-	-	-	-	-
11R-CC	-	-	-	-	X	-	-	-	-	-	X	-	-	-	-	-	-	-	-	X	-	-	-	-	-
139-855D-																									
3R-CC	-	-	-	-	-	-	-	-	-	-	X	-	-	-	-	-	-	-	-	-	-	-	-	-	-
4R-CC	-	-	-	-	-	-	-	-	-	-	-	-	-	-	-	-	-	-	-	-	-	-	-	-	-

in the magnitude of the diffusive flux. For example, the concentration of phosphate decreases by a factor of four between 20 to 30 mbsf, compared with 5- and 10-fold decreases in alkalinity and ammonium, respectively, at depths greater than 30 mbsf. This difference may result from uptake of phosphate on manganese- and iron-oxide surfaces, whereas alkalinity and ammonium may be released or nonreactive in the lower section of the sediment column. Oxide surfaces may form from the oxidation of dissolved iron and manganese, which are released to pore water during bacterial degradation of organic matter in the upper tens of meters of the sediment column. In Holes 855C and 855D, removal of phosphate lowers its concentration to values below that in bottom seawater.

The concentration of dissolved silica increases with depth in the upper part of the sediment column because of dissolution of amorphous silica (Fig. 20). The concentration generally increases downhole except within the lowermost 20 m of the sediment column, where dissolved silica may be removed by precipitation of silica-rich minerals or by a diffusive flux to basaltic basement. Such a diffusive flux would require that the concentration of silica in the water in the underlying basalt is similar to that in bottom seawater. Initial visual examination of the sediment (see "Sedimentology and Lithostratigraphy" section, this chapter) does not support the formation of silica-rich minerals. On the basis of other chemical profiles, we suggest that the water in the underlying basalt has a concentration of dissolved silica similar to that in bottom seawater.

The concentration of calcium in pore water at Site 855 (Fig. 19) is changed from that in bottom seawater by reaction with sediment. Most reaction probably is with carbonate, clays, and detrital igneous minerals. Plagioclase feldspar especially is abundant in the turbidite-rich sediment. The concentration of dissolved calcium remains nearly constant over the upper 15 to 20 mbsf, but this lack of change probably results from a balance between loss and gain from solution rather than from nonreaction. Calcium may be lost from solution as a result of bacterial oxidation of organic matter utilizing dissolved sulfate. This reaction produces alkalinity in an amount equivalent to the sulfate loss. The general reaction is:

$$2\ CH_2O + SO_4^{2-} = H_2S + 2\ HCO_3^{2-}.$$

Table 4 (continued).

Sample	*Nonionella turgida*	*Nonionella* spp.	*Oridorsalis tener*	*Pullenia bulloides*	*Pullenia quinqueloba*	*Pullenia salisburyi*	*Reussella* sp. A	*Rosalina* cf. *R. columbiensis*	*Rutherfordoides* sp. A	*Sphaeroidina bulloides*	*Sphaeroidina* spp.	*Stainforthia complanata*	*Stainforthia rotunda*	*Uvigerina dirupta*	*Uvigerina senticosa*	*Valvulineria laevigata*	*Valvulineria* sp. A	*Valvulineria* sp.	Others:	*Arachinodiscus*	Brown glass	Celadonite	Clay lumps	Diatoms	Mica	Mineral grains
139-855A-																										
1R-1, 0–1	-	-	-	X	-	-	-	-	-	-	-	-	-	X	X	-	X	-		-	-	-	-	A	-	-
1R-CC	-	-	-	X	X	-	X	-	-	-	-	-	-	X	X	X	X	-		-	-	R	-	C	-	R
2R-CC	-	-	-	X	-	X	-	-	-	X	-	-	-	-	-	X	-	-		-	-	-	-	-	-	A
3R-CC	-	-	-	-	-	-	-	-	X	-	-	X	X	-	X	-	X	-		R	-	-	-	-	A	-
4R-CC	-	-	X	-	-	X	-	-	-	-	-	-	-	-	-	-	X	-		-	-	R	-	-	-	A
5R-CC	-	-	-	X	X	X	-	X	-	X	-	X	X	-	X	-	-	-		-	-	F	A	-	C	F
6R-CC	-	-	-	-	-	-	-	-	X	-	-	X	X	-	-	-	-	-		-	-	-	A	R	A	-
7R-CC	-	-	-	-	-	-	-	-	-	X	-	-	-	-	-	-	-	-		-	-	-	F	-	-	-
8R-CC	-	-	X	-	-	-	-	-	X	-	X	-	-	-	X	-	-	-		-	A	-	-	C	-	A
139-855B-																										
2R-1, 0–1	-	-	-	X	-	-	-	-	-	-	-	X	-	-	X	-	-	-		-	-	-	A	-	A	A
2R-CC	-	X	-	-	-	-	-	-	-	-	-	X	-	-	X	-	X	-		-	-	-	A	-	-	C
4R-CC	X	-	-	X	-	-	-	-	-	-	-	X	X	-	X	-	X	X		-	-	-	-	R	A	A
5R-CC	-	-	-	-	X	-	-	-	-	-	-	-	-	-	-	-	-	-		R	-	-	C	R	A	A
6R-CC	-	-	-	-	-	X	-	-	-	-	-	X	-	-	-	-	X	-		-	-	-	A	-	-	-
139-855C-																										
1R-1, 0–1	-	-	-	X	-	X	-	-	-	-	-	X	-	X	X	-	X	-		-	-	-	A	-	-	-
1R-CC	-	-	-	-	-	-	-	-	-	-	-	X	-	-	X	-	X	-		-	-	-	-	-	A	C
2R-CC	-	-	-	-	-	-	-	-	-	X	-	X	-	-	X	-	-	-		-	-	-	-	-	-	-
3R-CC	-	-	-	X	-	-	-	-	-	X	-	-	-	-	X	-	X	-		-	-	-	A	-	-	-
4R-CC	-	-	-	X	-	X	-	-	X	-	-	-	-	-	X	-	X	-		-	-	-	A	-	C	-
5R-CC	-	-	X	-	-	X	-	-	-	-	-	X	-	-	X	-	-	-		-	-	F	A	-	-	A
6R-CC	-	-	-	-	-	-	-	-	X	-	-	-	-	-	-	-	X	-		-	-	-	C	-	A	-
7R-CC	-	-	-	-	-	-	-	-	-	-	-	-	-	-	-	-	-	-		-	-	-	F	-	A	-
8R-CC	-	-	-	-	-	-	-	-	-	-	-	-	-	-	-	-	-	-		-	-	-	C	-	-	-
9R-CC	-	-	-	-	-	-	-	-	-	X	-	-	-	-	-	-	-	-		R	-	-	-	-	A	-
10R-CC	-	-	-	-	-	-	-	-	-	-	-	X	-	-	-	-	-	-		-	A	-	-	-	A	-
11R-CC	-	-	-	-	-	-	-	-	-	-	-	-	-	-	-	-	-	-		-	-	-	-	-	A	A
139-855D-																										
3R-CC	-	-	-	-	-	-	-	-	-	-	-	-	-	-	-	-	-	-		-	-	-	-	-	A	-
4R-CC	-	-	-	-	-	-	-	-	-	-	-	-	-	-	-	-	-	-		-	-	-	A	-	-	-

Sulfate decreases sharply over the upper 15 to 20 mbsf, by about 13 meq/kg, while alkalinity increases by only about 8 meq/kg. The difference of 5 meq/kg alkalinity is probably removed by precipitation of calcium carbonate:

$$2\ HCO_3^{2-} + Ca^{2+} = CaCO_3 + H_2O + CO_2,$$

although no overgrowths were observed on foraminifers and nannofossils in the sediment from this interval. The removal of 5 meq/kg calcium from solution is apparently balanced by an equivalent supply from reaction with silicates or from diffusion. The reactive source is apparent in the increase in dissolved calcium with depth below 15 to 20 mbsf. This increase reaches a maximum in Hole 855A at a depth of 36 mbsf; at greater depths in this hole calcium decreases to a projected concentration of about 10.5 mmol/kg at the sediment-basalt interface. This is close to the value of 10.2 mmol/kg in bottom seawater. A maximum in the concentration of calcium in pore water from Hole 855C exists at 59 mbsf, below which the concentration generally decreases except for the deepest two samples. The deepest samples in both Holes 855C and 855D have about 12.2 mmol/kg calcium, implying that the water in the underlying basalt has a greater calcium concentration than that of bottom seawater.

The difference in the inferred concentration of calcium in water in the underlying basalt in Hole 855A vs. Holes 855C and 855D can be explained if bottom seawater is entering the crust along the fault. The downwelling seawater still retains its composition at the location of Hole 855A, which was drilled directly into basalt along the fault plane itself. This seawater then flows away from the fault and reacts with the basalt before it reaches the location of Holes 855C and 855D. The longer flow path inferred would also allow greater diffusive input of calcium from the sediment pore water into water in the underlying basalt. Other explanations for the different calcium concentration in water in the underlying basalt are differences in the magnitude of the squeezing artifact and in the extent of reaction at the interface. The

Table 4 (continued).

Sample	Ostracodes	Pine pollen	Pipe rust	Pyrite	Radiolarians	Sponge spicules	Test fragments	Unknown substance	Urchin spines
139-855A-									
1R-1, 0–1	-	-	C	-	A	C	-	-	-
1R-CC	-	-	-	-	C	F	-	-	-
2R-CC	-	-	F	-	C	-	-	-	-
3R-CC	-	-	R	F	-	C	-	-	-
4R-CC	R	-	-	-	-	R	-	-	-
5R-CC	-	-	-	-	A	A	-	-	-
6R-CC	-	-	-	R	R	C	-	-	-
7R-CC	R	-	-	C	-	-	-	A	-
8R-CC	-	-	-	-	C	A	-	-	-
139-855B-									
2R-1, 0–1	-	-	-	-	-	C	-	-	-
2R-CC	-	-	-	-	C	F	-	-	R
4R-CC	-	R	-	-	R	C	-	-	-
5R-CC	-	R	-	-	-	C	-	-	-
6R-CC	-	-	-	F	A	C	A	-	-
139-855C-									
1R-1, 0–1	-	-	-	-	C	F	-	-	-
1R-CC	R	-	-	-	C	A	A	-	-
2R-CC	-	-	-	-	-	-	-	-	-
3R-CC	-	-	-	-	-	-	-	-	-
4R-CC	-	-	-	-	F	-	A	-	-
5R-CC	-	-	-	F	-	-	-	-	-
6R-CC	-	-	-	A	R	-	-	-	-
7R-CC	-	-	-	-	-	A	-	-	-
8R-CC	-	-	-	-	-	-	-	-	-
9R-CC	-	-	-	-	R	-	-	-	-
10R-CC	-	-	-	A	-	-	-	-	-
11R-CC	-	-	-	A	-	-	-	-	-
139-855D-									
3R-CC	-	R	-	C	-	-	-	-	-
4R-CC	-	-	-	A	-	-	-	-	-

Table 5. Comparison of sequences zoned for calcareous nannofossils (Martini, 1971; Gartner, 1977) and for planktonic foraminifers (Lagoe and Thompson, 1988).

Sample	Depth (mbsf)	Age	Foraminifer zone	Nannofossil zone
Hole 855A				
1R-1, 0–1 cm	0.0	Holo.	CD1	NN21
1R-CC	7.6			
2R-CC	16.6	late Pleistocene	CD2?	
3R-CC	26.0			
4R-CC	35.5			
5R-CC	45.5			
6R-CC	55.1			
7R-CC	64.8			
8R-CC	74.3			
Hole 855B				
2R-1, 0–1 cm	5.7	late Pleistocene	CD2?	NN21
2R-CC	15.1			
4R-CC	34.0			
5R-CC	43.9			
6R-CC	48.6			
Hole 855C				
1R-1, 0–1 cm	0.0	Holo.	CD1	NN21
1R-CC	8.7	late Pleistocene	CD2?	
2R-CC	17.7			
3R-CC	27.1			
4R-CC	36.6			
5R-CC	46.5			
6R-CC	56.1			
7R-CC	65.7			
8R-CC	75.2			
9R-CC	84.9			
10R-CC	94.6	Pleis.		?
11R-CC	101.2			
Hole 855D				
3R-CC	104.3	Pleis.	CD2?	NN19–NN21
4R-CC	108.5			

temperature difference at the base of Holes 855A, 855C, and 855D is about 30°C, based on an extrapolation of surficial heat flow (see "Heat Flow" section, this chapter). If this temperature difference produces a 20% difference in the calcium concentration on squeezing, then similar artifacts should be observed in other holes with similar temperature differences; such artifacts are not observed. The alkalinity and sulfate profiles from Holes 855A, 855C, and 855D, and visual observations of core from these holes, do not support differential reaction involving carbonates or anhydrite near the sediment-basalt interface. Thus the first explanation is preferred.

Profiles of magnesium at Site 855 are controlled by reaction and diffusion in the sediment (Fig. 19). The magnesium concentration decreases downhole as a result of removal into alteration products, probably clay minerals, and reaches a minimum at depths ranging from 20 to 65 mbsf. At greater depth it increases to concentrations near that in bottom seawater. As was the case for calcium, the magnesium concentration at the sediment-basalt interface approaches that of bottom seawater more closely in Hole 855A than in Holes 855C and 855D.

Profiles of chlorinity provide a limiting constraint on vertical fluid velocity through the sediment and a measure of artifacts induced by sampling (Fig. 18). Vertical fluid velocity is estimated using the glacial-to-interglacial variability in the chlorinity of bottom seawater. At the peak of the last glacial period, the chlorinity of bottom seawater was about 4% greater than the present-day value (Imbrie et al., 1984). This difference should produce a chlorinity maximum at 20 to 40 mbsf that is about 2% greater than the present-day value, but only in areas where vertical fluid velocities are less than about 1 mm/yr. If vertical fluid flow is faster than several mm/yr, then chlorinity should be uniform with depth. The uniform value would be that of bottom seawater if water is downwelling through the sediment, and that of basement water if water is upwelling. A maximum in the chlorinity profiles is observed at Site 855, implying that vertical fluid velocities have been less than about 1 mm/yr throughout the past 20 ka. None of the other chemical profiles supports the presence of flow through the sediment.

Profiles of chlorinity also provide a clear measure of artifacts induced by coring and sampling, because chlorinity is nonreactive. One quarter-round sample clearly shows evidence of evaporation (Sample 139-855B-4R-5, 132–147 cm). The chemical data from this sample are adjusted to a chlorinity of 547.9 mmol/kg in Figures 18 to 20 to account for evaporation. Some whole-round samples have probably been disturbed by drilling,

Table 6. Range chart of calcareous nannofossils and their abundance and preservational state plotted with zonal assignments and ages of samples.

Hole 855A	Depth (mbsf)	Age	Nannofossil zonation	Abundance	Preservation	*Emiliania huxleyi*	*E. pujosae*	small *Gephyrocapsa*	*G. caribbeanica*	*Calcidiscus leptoporus*	*Coccolithus pelagicus*	*Braarudosphaera bigelowii*	*Syracosphaera pulchra*	*Pontosphaera japonica*	*Thoracosphaera* sp.	*Umbilicosphaera mirabilis*
1R-1, 0–1 cm	0	late Pleistocene – Holocene	NN21	A	M	F		C		C	C		R			
1R-CC	7.6			A	M	C	F	C	F	R	C	R	R	R	R	R
2R-CC	16.6			C	P	F	F	C	F		C	R				
3R-CC	26.0			C	P	R		C	R		F		R			
4R-CC	35.5			F	P			F		R	C		R			
5R-CC	45.5			C	P	R		C	R		F	R				
6R-CC	55.1			F	P			F	R	R	R					
7R-CC	64.8			C	P			C	R	R	R					
8R-CC	74.3			A	P	R		A	R	F	F		R			

Hole 855B	Depth (mbsf)	Age	Nannofossil zonation	Abundance	Preservation	*Emiliania huxleyi*	*E. pujosae*	small *Gephyrocapsa*	*G. caribbeanica*	*Calcidiscus leptoporus*	*Coccolithus pelagicus*	*Braarudosphaera bigelowii*	*Syracosphaera pulchra*	*Pontosphaera japonica*	*Thoracosphaera* sp.	*Umbilicosphaera mirabilis*
2R-1, 0–1 cm	0	l. Pleistocene –Holocene	NN21	C	M	F	R	C	R		R					
2R-CC	15.1			C	P	R		C			F					
4R-CC	34.0			R	P	R		R			R					
5R-CC	43.9			F	P	R		R			R					
6R-CC	48.6			F	P	R		F			F					

Hole 855C	Depth (mbsf)	Age	Nannofossil zonation	Abundance	Preservation	*Emiliania huxleyi*	small *Gephyrocapsa*	*G. caribbeanica*	*Calcidiscus leptoporus*	*Coccolithus pelagicus*	*Braarudosphaera bigelowii*	*Syracosphaera pulchra*	*Umbilicosphaera mirabilis*	*Rhabdosphaera claviger*
1R-1, 0–1 cm	0	late Pleistocene – Holocene	NN21	A	M	F	A	R	R	C		R		
1R-CC	8.7			F	P	R	F	R	R	C		R	R	
2R-CC	17.7			A	M	R	A			C	R			
3R-CC	27.1			C	P	R	C	R	R	F		R		R
4R-CC	36.6			F	P		F			F				
5R-CC	46.5			A	P	R	A			C				
6R-CC	56.1			C	M	R	C	R		R	R			
7R-CC	65.7			F	P	R	F			R				
8R-CC	75.2			R	P		R							
9R-CC	84.9	Pleis.	?	C	P	R	C	R		R				
10R-CC	94.6			C	P		C			R				
11R-CC	101.2			R	P		R			R				

Hole 855D	Depth (mbsf)	Age	Nannofossil zonation	Abundance	Preservation	small *Gephyrocapsa*	*G. caribbeanica*	*Coccolithus pelagicus*
3R-CC	104.3	Pleis.	NN19–NN21	F	P	F	R	F
4R-CC	108.5			B				

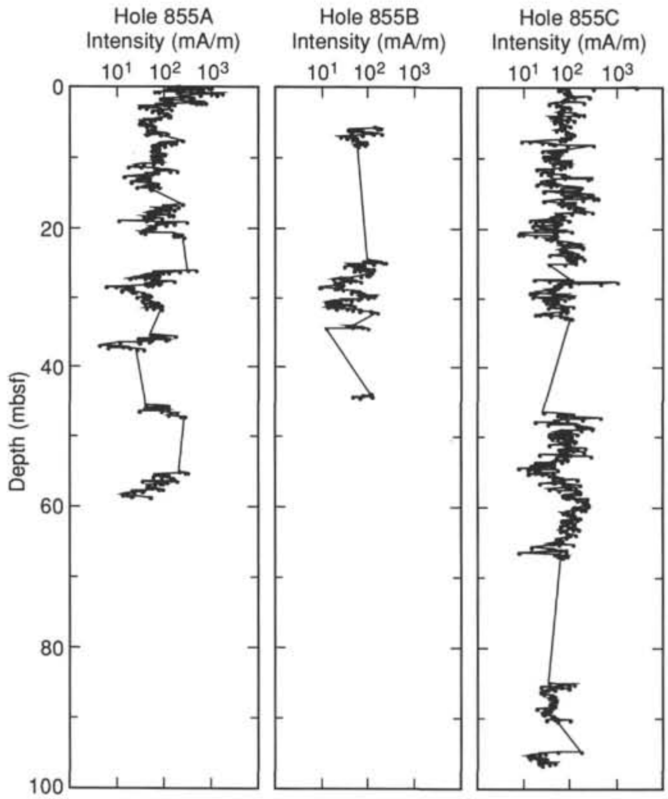

Figure 11. NRM intensity vs. depth for Holes 855A, 855B, and 855C.

Table 7. Inclination (*I*), natural remanent magnetization intensity (J_0), and median destructive field (MDF) for discrete samples.

Core, section, interval (cm)	Depth (mbsf)	*I* (degrees)	J_0 (mA/m)	MDF (mT)
139-855A-				
1R-1, 83–85	0.83	13	45	30
2R-2, 128–130	10.38	42	92	29
4R-2, 49–51	27.99	–6	22	26
139-855B-				
4R-1, 112–114	25.62	–60	29	28
4R-2, 40–42	26.40	–77	62	30
4R-2, 123–125	27.23	–9	18	24
139-855C-				
1R-3, 60–62	3.60	42	55	27
2R-3, 62–64	12.32	42	48	30
4R-1, 62–64	27.72	52	64	30
4R-1, 117–119	28.27	–27	38	28
6R-1, 105–107	47.55	–48	62	23

Note: All samples were AF demagnetized.

resulting in contamination from the low-chlorinity surface seawater used as drilling fluid. Samples probably disturbed by drilling include intervals 139-855C-6R-1, 140–150 cm (48 mbsf); -6R-6, 140–150 cm (55 mbsf); and -9R-1, 0–5 cm (75 mbsf). Data from these samples are not corrected in Figures 18 to 20. One of the WSTP samples (139-855D-1I-1) has low chlorinity and a disturbed temperature record, indicating contamination with drilling fluid. The data for this sample are adjusted in Figures 18 to

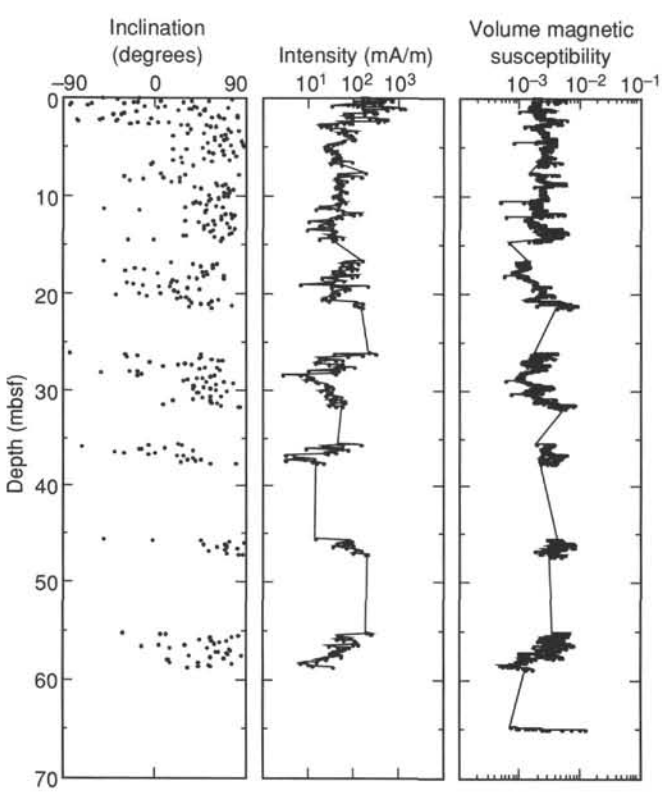

Figure 12. Inclination and intensity, after 15-mT AF demagnetization, and volume magnetic susceptibility vs. depth for Hole 855A.

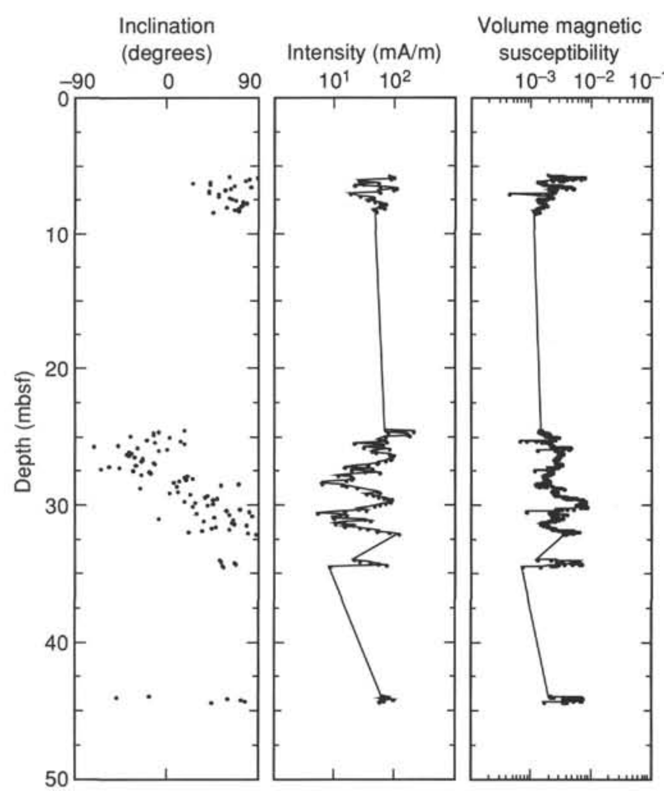

Figure 13. Inclination and intensity, after 15-mT AF demagnetization, and volume magnetic susceptibility vs. depth for Hole 855B.

20, to a chlorinity of 540 mmol/kg, assuming mixing either with surface water or with distilled water that was not completely flushed from the sample coil. Another WSTP sample (139-855C-5I-1) may be contaminated but is not adjusted in Figures 18 to 20.

The concentration of potassium in pore water near the sediment-water interface at Site 855 is greater than that in bottom seawater (Fig. 19), presumably as an artifact of squeezing. This method of separating pore water from sediment is known to increase the concentration of dissolved potassium above that measured in waters separated *in situ*. At Site 855, potassium decreases with depth to a concentration close to that in bottom seawater. This decrease may reflect a decrease in the squeezing artifact with increasing *in-situ* temperature. Alternatively, the potassium decrease may be a product of low-temperature (<150°C) reaction of pore water with sediment or the underlying basalt.

The pH of pore water from Site 855 ranges from 7.6 to 8, typical of pore waters in marine settings (Fig. 18). Profiles of dissolved sodium are calculated by charge balance and closely parallel those of chlorinity (Fig. 18).

Conclusions

Chemical profiles of sediment pore water from Site 855 indicate that interstitial water in basement is similar to bottom seawater, especially in the holes nearer to the rift-bounding fault. Farther from the fault, calcium and magnesium are slightly changed. We suggest that bottom seawater enters basement along the fault and flows outward from it, reacting as it goes. There has been no vertical flow of pore water through the sediment at this site faster than about 1 mm/yr since the last glacial maximum, about 20 ka ago.

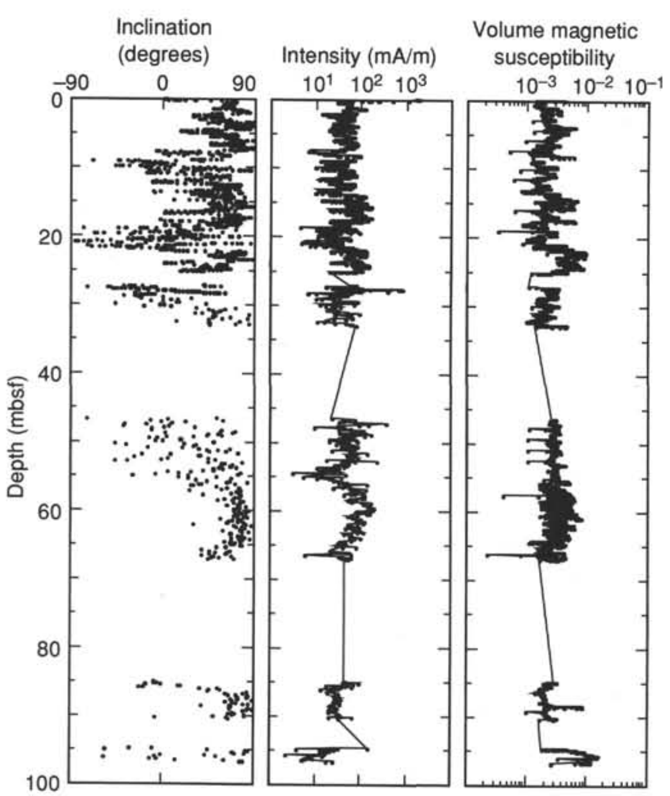

Figure 14. Inclination and intensity, after 15-mT AF demagnetization, and volume magnetic susceptibility vs. depth for Hole 855C.

ORGANIC GEOCHEMISTRY

Shipboard organic geochemical analyses of sediments from Holes 855A, 855B, 855C, and 855D included inorganic carbon, total carbon, hydrogen, nitrogen, sulfur, volatile hydrocarbon and non-hydrocarbon gases, organic matter fluorescence estimation, and total hexane soluble lipid/bitumen analysis. The instrumentation, operating conditions, and procedures are summarized in the "Explanatory Notes" chapter (this volume).

Volatile Gases

Volatile gases (hydrocarbons, CO_2, H_2S, N_2, CS_2, O_2) were continuously measured by gas chromatography in the sediments at Site 855 as part of the shipboard safety and pollution monitoring program. We used the headspace technique, in which a sediment plug is heated in a sealed vial to drive off gases (Emeis and Kvenvolden, 1986). The results are listed in Table 9. The methane concentrations in the headspace volumes range between 2 and 6 ppm (volume/volume, or v/v), which are slightly greater than the laboratory background level of 2 ppm. No ethane or higher hydrocarbons, nor H_2S, were detected. The overall low methane contents in these sediments suggest that environmental conditions were not favorable for methanogenesis. Methanogenic bacteria are generally active only after complete sulfate depletion by sulfate-reducing bacteria (Claypool and Kaplan, 1974). The concentrations of sulfate in interstitial waters at Site 855 decrease to a minimum of 21 mmol/kg at 10 to 20 mbsf, then increase again with depth, but the minimum represents only a 25% depletion from seawater (see "Inorganic Geochemistry" section, this chapter). Therefore, methanogenesis via CO_2 reduction, the major process by which microbial methane is produced in deep-sea sediments, was probably not possible.

Carbon dioxide was present at concentrations of 2% to 7% in gases desorbed from the sediments by the headspace method (Fig. 21, Table 9). Even higher amounts of free CO_2 could have been present in the sediments and pore waters before the depressurization that occurs during core retrieval. These amounts must be less than the concentration at saturation solubility in water at 1 atmosphere (atm) (1437 cm^3 or 2.82 g of CO_2 per liter [L] of seawater at 0°C and 1 bar; Broecker and Peng, 1982), as no gas pockets or cracks were observed in the cores as they were brought on deck. For 5 cm^3 of sediment and a headspace volume of 15 cm^3, and assuming that all of the CO_2 present in the sediment is driven into the gas phase during heating at 60°C, the approximate concentration of CO_2 dissolved in the sediment and its associated pore water as the core arrived on deck can be estimated by rearranging the ideal gas equation, $pv = nRT$:

$$\text{Wt of } CO_2(g) = \frac{44\text{ (g/mol) (1atm) (0.015 L headspace} \times 0.07\ CO_2)}{(0.082\ [\text{1atm/°C mol}])\ (300°C)}$$

This calculation gives 0.5- to 1.9-mg CO_2 as the range of weights of CO_2 initially present in 5 cm^3 of sediment, or 0.12 to 0.37 g CO_2/L sediment. Assuming a porosity of 60%, this concentration of CO_2 would represent about 7% to 22% of the saturation value, at 0°C and 1 bar, in the pore waters of these sediments.

Fluorescence

The extract colors progressed from pale yellow-green to pale yellow to colorless with increasing depth in each hole. The concentrations of extractable organic matter are extremely low, based on the color and fluorescence intensities. Nevertheless, weak fluorescence was observed from 35 to 65 mbsf in Hole 855A (yellow), at 44 mbsf in Hole 855B (white), and from 56 to 101 mbsf in Hole 855C, where the fluorescence color changed from yellow to white at 85 mbsf. Yellow fluorescence is interpreted as thermal maturation of bitumen

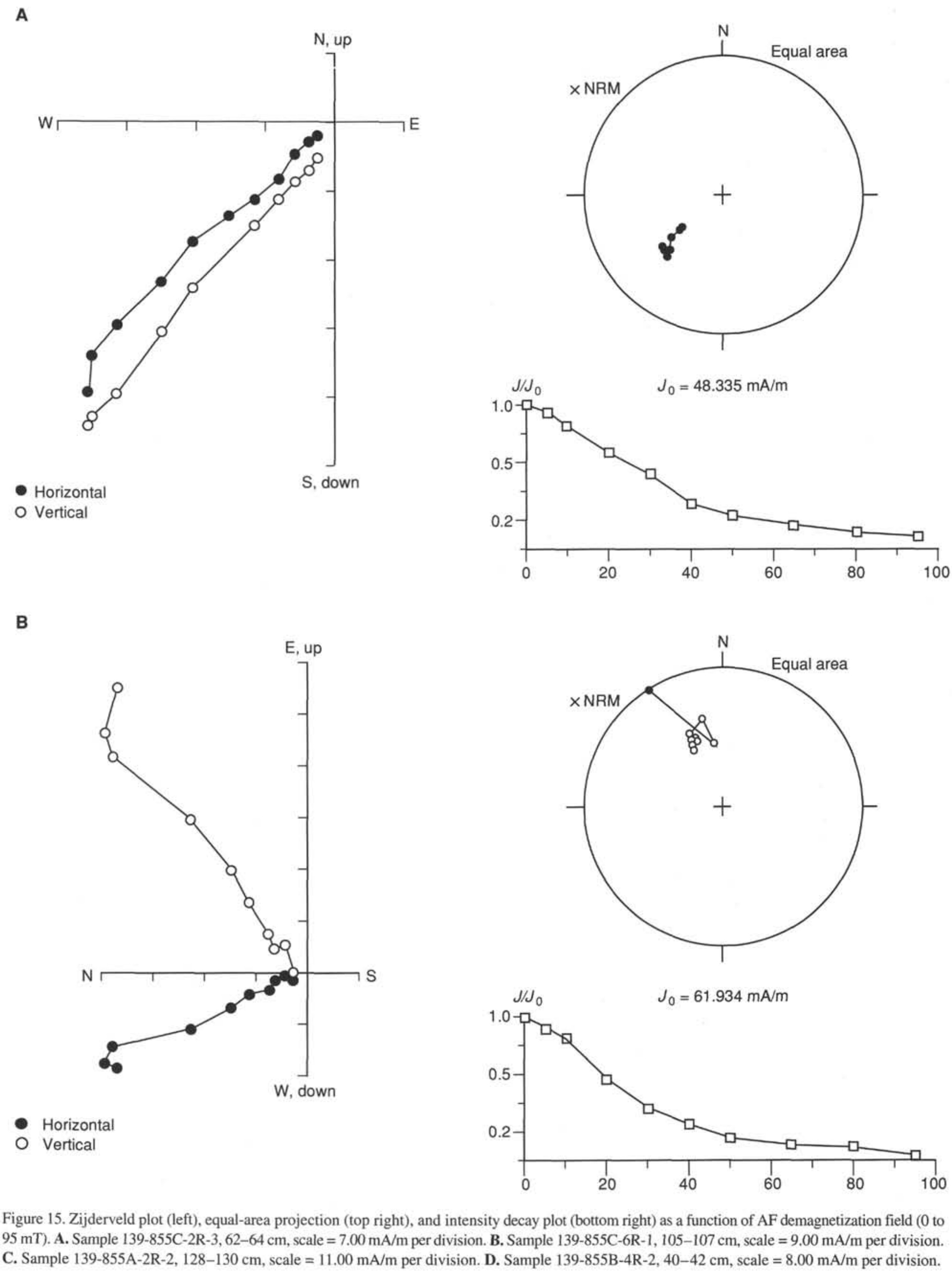

Figure 15. Zijderveld plot (left), equal-area projection (top right), and intensity decay plot (bottom right) as a function of AF demagnetization field (0 to 95 mT). **A.** Sample 139-855C-2R-3, 62–64 cm, scale = 7.00 mA/m per division. **B.** Sample 139-855C-6R-1, 105–107 cm, scale = 9.00 mA/m per division. **C.** Sample 139-855A-2R-2, 128–130 cm, scale = 11.00 mA/m per division. **D.** Sample 139-855B-4R-2, 40–42 cm, scale = 8.00 mA/m per division.

C

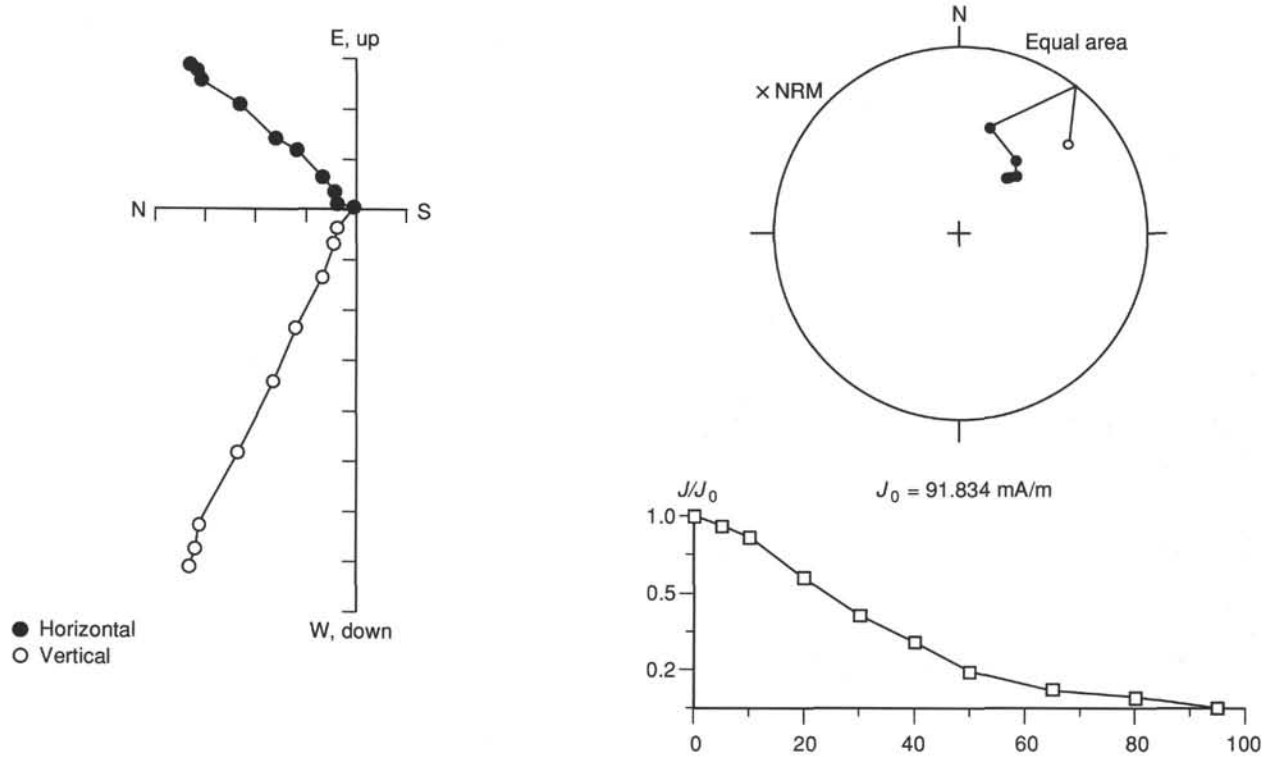

D

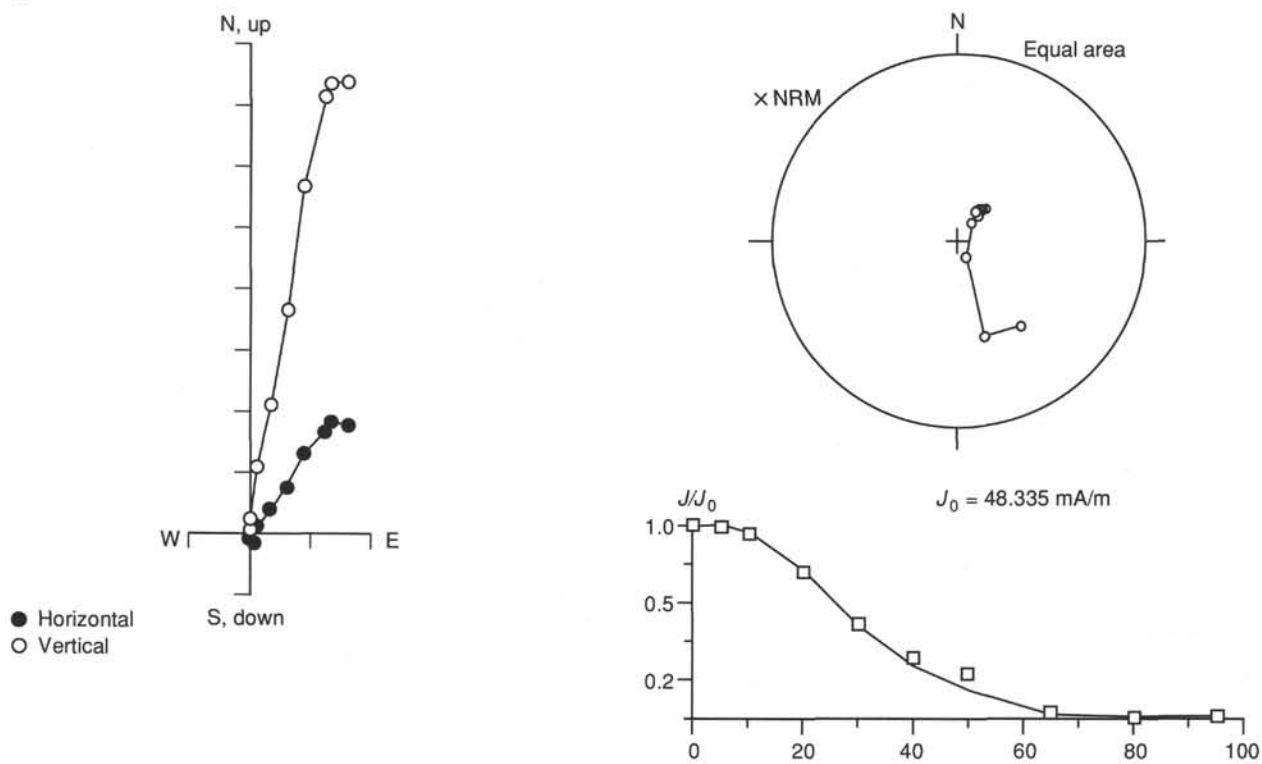

Figure 15 (continued).

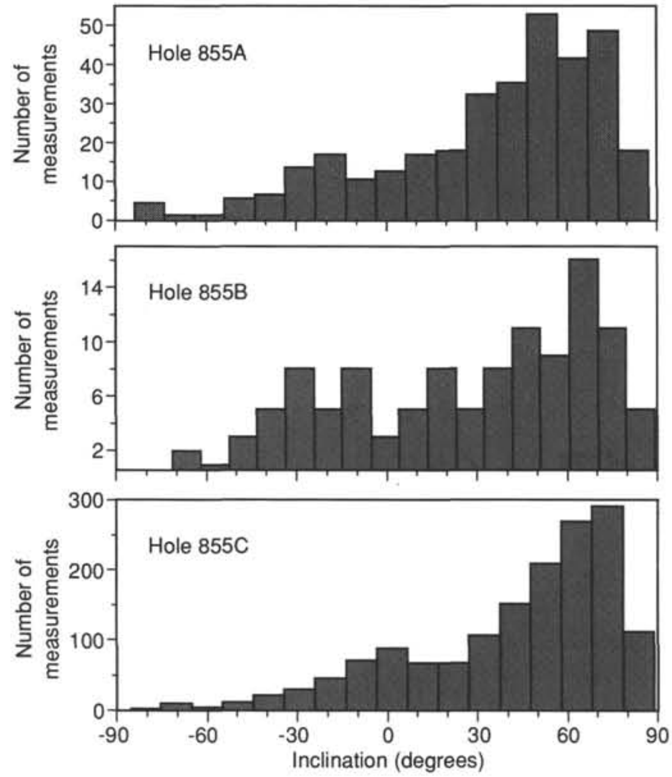

Figure 16. Histograms of inclination after 15-mT AF demagnetization for Holes 855A, 855B, and 855C.

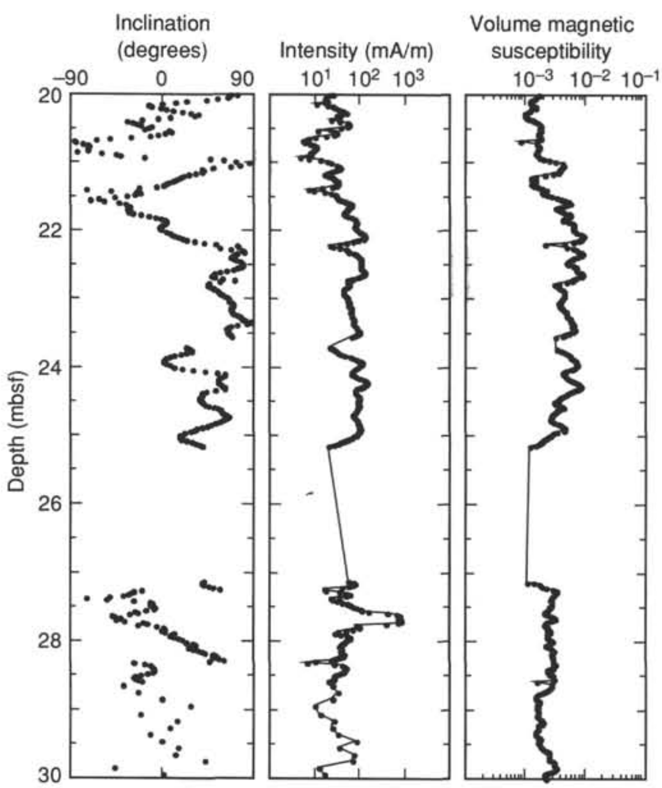

Figure 17. Expanded depth-scale plots of inclination and intensity after 15-mT AF demagnetization and volume magnetic susceptibility for Hole 855C from 20 to 30 mbsf.

to the mature stage and white fluorescence is overmature bitumen enriched in polynuclear aromatic hydrocarbons (PAH) (Shipboard Scientific Party, 1982).

Bitumen Analyses

The hexane extracts (500 µL) of the samples from the fluorescence assessment or subsamples of freeze-dried sediments were concentrated under a stream of nitrogen to about 10–40 µL. These concentrates were analyzed by high-resolution gas chromatography and examples of traces are shown in Figure 22. The dominant compound series in the total extracts are hydrocarbons ranging from n-C_{15} to n-C_{35} with pristane ($C_{19}H_{40}$) as the major isoprenoid alkane. The bitumen parameters for maturation and organic matter sources are listed in Table 10. The n-alkanes $>C_{26}$ have a significant predominance of odd carbon numbers (carbon preference index, CPI, >1.0), typical for immature hydrocarbons that originate from terrestrial higher plants (Simoneit, 1977, 1978). The CPI for the range C_{26}–C_{35} (n-C_{25} coelutes with a solvent contaminant; thus, the CPI is calculated for $>C_{26}$) decreases variably vs. sub-bottom depth and increasing thermal alteration from 3.2 to 1.6, where the latter value is for the strongly fluorescing bitumen in Sample 139-855C-10R-CC (Table 10). Maturation is also evident in the isoprenoid to normal hydrocarbon ratios (Pr/n-C_{17} range 5.0 to 0.2, Ph/n-C_{18} range 1.3 to 0.4, Table 10). The pristane to phytane ratios (Pr/Ph) vary from 5.0 to 0.8 (Table 10) with depth, possibly reflecting varying thermal stress. The n-alkane patterns $<C_{24}$ with the unresolved complex mixture (UCM) of branched and cyclic compounds and the relative yields (Table 10) are typical for autochthonous marine bitumen derived from alteration of microbial lipids (Simoneit, 1977, 1978).

The lipids of Sample 139-855D-4R-CC (Fig. 22C) have a similar composition of marine and terrestrial components, with a major contribution of alkenones from marine algae such as coccolithophorids (e.g., Marlowe et al., 1984; Volkman et al., 1980). The n-alkanes range from C_{14} to C_{35}, with maxima at C_{20} and C_{29}, and $CPI_{26-35} = 2.7$. The marine components are in the range $<n$-C_{22} and the terrestrial plant wax influx is represented by the homologs $>n$-C_{23}. The isoprenoid ratios are: Pr/Ph = 2.5, Pr/n-C_{17} = 1.8 and Ph/n-C_{18} = 0.7, indicating significant maturation. The U^K_{37} index (e.g., Marlowe et al., 1984) for the alkenones as defined here ($[C_{37:2}]/[C_{37:2} + C_{37:3}]$) is 0.17 for this sample, indicating quite cold climatic conditions in the water column before deposition.

The hydrocarbon signature of these sediments is quite similar to those reported for shallow gravity cores taken near the Middle Valley hydrothermal vents (Simoneit et al., in press). These hydrocarbon mixtures have matured rapidly because of the high regional heat flow, which has accelerated diagenesis. Furthermore, these data can be compared to profiles obtained from the Alaskan North Slope Ikpikpuk well (Farrington et al., 1988), where Pr/n-C_{17} decreased linearly over a 1000-m interval, from values of 2.5 to 0.25 over a very narrow vitrinite reflectance range of about 0.6% to 0.8%. Thus, in the Ikpikpuk well, a large and relatively linear change in the Pr/n-C_{17} ratio over a narrow maturation range corresponded roughly to temperatures in the beginning of the oil window in the range of about 50° to 60°C. At Site 855, a higher initial Pr/n-C_{17} value and a smaller range is observed (5.0 to 1.3), consistent with either a different source type of organic matter with a higher initial ratio or a lower initial temperature at this site in comparison to the lowest values estimated for the Ikpikpuk well.

At Site 855, the present bottom-water temperature is about 2°C and the sedimentary geothermal gradient is near 0.33°C/m, suggesting a maximum present-day temperature of about 33°C in the deepest interval penetrated at about 100 mbsf. This temperature is too low to have produced any change in Pr/n-C_{17} ratios with depth at Site 855 and suggests that the geothermal gradient was higher in the past. The strongly fluorescing bitumen in Core 139-855C-10R is also consistent with the deepest sediments at this site having pre-

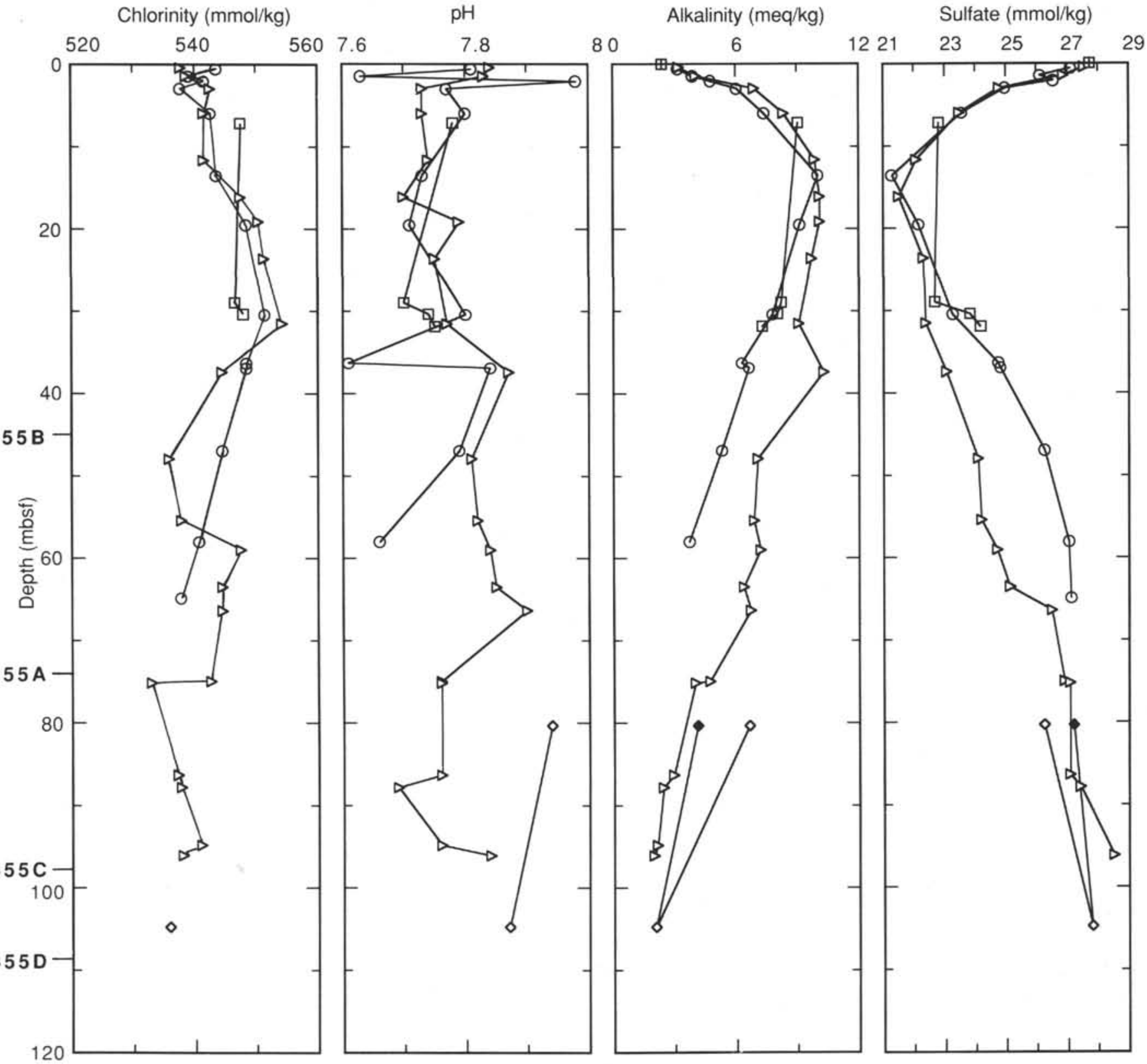

Figure 18. Composition of pore water from sediments at Site 855. Hole 855A = circles; Hole 855B = squares; Hole 855C = triangles; Hole 855D = diamonds. The depth at which basalt was encountered is labeled for each of the holes and the plus inside a square at 0 mbsf denotes bottom seawater. Two diamonds are plotted at 80 mbsf for the WSTP sample from Hole 855D. These represent corrected values assuming that this sample was contaminated either with surface seawater during collection (open), or with distilled water that was not completely flushed from the sample coil (solid).

viously been exposed to temperatures high enough to take them into the beginning of the oil window (50°C or slightly higher).

The trends in Pr/Ph and Ph/n-C_{18} at Site 855 are more difficult to interpret. Pr/Ph is highly formation dependent in the Ikpikpuk well, although it has been reported to respond to maturation (Simoneit et al., 1981), as well as anoxic conditions during sediment deposition (Didyk et al., 1978).

In one case of organic-lean sediments with a high proportion of terrigenous organic matter (East Cameron well in the Gulf of Mexico, J. Whelan et al., pers. comm., 1991), Ph/n-C_{18} decreased smoothly with increasing depth and maturation. However, in the Ikpikpuk well discussed above, the trend is just the opposite–a clear increase in Ph/n-C_{18} with depth is observed (Farrington et al., 1988). The differences may be due to preferential expulsion of the straight-chain (normal) over the branched-chain compounds (Pr and Ph) in the Ikpikpuk well. The sediments in the East Cameron well are too organic-lean to have undergone petroleum expulsion and are thus similar to the sediments of Site 855.

Elemental Analyses

Total C, H, N, and S were measured via a total combustion method in the presence of tin and vanadium pentoxide catalyst (see "Explanatory Notes" chapter, this volume). The calibrations for all four elements were linear over a wide range of concentrations, giving reliable values even for samples containing only small amounts of any of these elements.

Table 8. Composition of pore water in sediments from Site 855.

Sample[a]	Core, section, interval (cm)	Depth (mbsf)	Volume (mL)	Squeeze pressure (psi)	Salinity by refractive index (‰)	pH	Alkalinity (meq/kg)	Chlorinity (mmol/kg)	Sulfate (mmol/kg)	Na (mmol/kg)	K (mmol/kg)
Surface seawater (22 July 1991)									496.0		10.4
Core top water (Core 139-855A-1R)					33.0	7.64	2.140	512.5	26.44	438.0	
Bottom seawater (calculated for 541 mmol/kg chlorinity)							2.31	541.0	27.95	463.3	10.1
	139-855A-										
IW-1	1R-1, 55–70	0.63	21	12000	35.0	7.81	3.183	543.6	27.12	467.6	12.5
IW-2	1R-1, 144–150	1.47	39	12000	35.5	7.63	3.905	539.1	26.13	462.2	12.1
IW-3	1R-2, 53–67	2.10	16	5000	35.0	7.98	4.769	541.6	26.55	466.9	13.1
IW-4	1R-2, 144–150	2.97	50	5000	35.0	7.77	6.046	537.7	24.98	461.1	13.4
IW-5	1R-4, 144–150	5.97	22	5000	35.0	7.80	7.395	542.6	23.56	464.0	13.5
IW-6	2R-4, 140–150	13.55	39	8000	36.0	7.73	10.020	543.6	21.29	462.6	12.6
IW-7	3R-2, 140–150	19.55	49	10000	35.0	7.71	9.127	548.4	22.15	472.1	11.5
IW-8	4R-3, 140–150	30.45	44	12000	35.0	7.80	7.785	551.4	23.26	469.7	12.9
BC-9	5I-1, 74–97	36.35	10	—	36.0	7.61	6.291	548.4	24.75	466.4	11.6
[c]BO-9	5I-1, 74–97	36.35	125	—	35.0			382.4			11.6
IW-10	5R-1, 140–150	36.95	42	10000	36.0	7.84	6.641	548.4	24.82	469.5	11.0
IW-11	6R-1, 140–150	46.95	50	6000	35.5	7.79	5.319	544.5	26.25	465.0	10.0
IW-12	7R-2, 140–150	58.05	47	9000	35.0	7.66	3.712	540.7	27.05	461.5	9.6
IW-13	8R-1, 10–12	64.91	2	10000	35.5			537.7	27.12		10.6
	Depth to basalt	74									
	139-855B-										
IW-1	2R-1, 140–150	7.15	52	5000	35.5	7.78	9.051	547.5	22.81		
IW-2	4R-3, 140–150	28.95	46	5000	36.0	7.70	8.222	546.5	22.66	469.0	11.3
IW-3	4R-4, 130–144	30.37	14	16000	36.0	7.74	8.020	547.9	23.83	469.6	13.2
IW-4	4R-5, 132–147	31.90	12	12000	36.0	7.75	7.433	559.1	24.66	480.6	11.8
	Depth to basalt	45									
	139-855C-										
IW-1	1R-1, 40–52	0.46	16		35.5	7.84	3.225	537.8	27.56	466.0	12.3
IW-2	1R-1, 144–150	1.47	31	10000	35.5	7.83	4.043	538.7	26.88	462.9	12.9
IW-3	1R-2, 144–150	2.97	47	6000	35.5	7.73	6.905	542.6	24.79	468.1	11.1
IW-4	1R-4, 144–150	5.97	46	7000	35.0	7.73	8.354	541.6	23.49	465.0	12.6
IW-5	2R-2, 140–150	11.65	50	7000	35.0	7.74	9.872	541.6	22.08	463.4	12.6
IW-6	2R-5, 140–150	16.15	49	8000	34.5	7.70	10.110	547.5	21.52	470.9	11.9
IW-7	3R-1, 140–150	19.15	42	10000	36.0	7.79	10.104	550.4			
IW-8	3R-4, 140–150	23.65	49	10000	36.0	7.75	9.707	551.3	22.31	474.0	10.9
IW-9	4R-3, 140–150	31.55	49	7000	36.5	7.77	9.073	554.2	22.39	475.5	12.1
BC-10	5I-1, 74–97	37.45	10	—	36.0	7.87	10.306	544.5	23.07	468.8	10.3
[c]BO-10	5I-1, 74–97	37.45	>80	—	12.5	8.21	9.183	185.7	28.98	478.1	15.0
IW-11	6R-1, 140–150	47.95	50	5000	36.0	7.81	7.080	535.8	24.09	459.6	10.8
IW-12	6R-6, 140–150	55.45	44	8000	35.5	7.82	6.880	537.8	24.20	461.2	10.9
IW-13	7R-2, 140–150	59.05	50	10000	36.0	7.84	7.197	547.5	24.71	468.8	10.6
IW-14	7R-5, 140–150	63.55	42	10000	35.5	7.85	6.371	544.5	25.13	468.3	10.7
IW-15	8R-1, 70–75	66.43	40	7000	36.0	7.90	6.720	544.5	26.49	469.4	10.9
BC-16	9I-1, 74–97	76.05	10	—	36.0	7.76	4.712	542.6	26.91	468.5	10.1
[c]BO-16	9I-1, 74–97	76.05	>550	—	31.0	7.77	4.944	477.8	26.04	470.1	11.2
IW-17	9R-1, 0–5	75.23	11	7000	34.5	7.76	3.992	532.9	27.08		
IW-18	10R-2, 0–10	86.35	40	16000	35.5	7.76	2.951	537.2	27.08	457.8	9.1
IW-19	10R-3, 140–150	87.85	40	18000	35.0	7.69	2.418	537.7	27.42	457.0	8.5
IW-20	11R-1, 20–33	94.87	5	20000	34.5	7.76	2.134	541.0			10.1
IW-21	11R-2, 0–10	96.15	21	18000	36.0	7.84	1.979	538.0	28.52	460.7	9.8
	Depth to basalt	97.5									
	139-855D-										
BC-1	1I-1, 74–97	80.35	10	—	33.5	7.94	3.912	513.4	25.87	443.8	10.3
[c]BO-1	1I-1, 74–97	80.35	200	—	23.5	8.20	4.138	355.9	25.66	444.1	9.4
IW-2	4R-1, 45–50	104.78	28	17000	35.0	7.87	2.067	535.8	27.81	459.3	8.7
	Depth to basalt	108									

[a]IW = squeezed interstitial water sample; BC = interstitial water sample taken *in situ* with the WSTP; BO = overflow aliquot from the WSTP (diluted with distilled water).
[b]Ca and Mg have been corrected using the equations of Gieskes and Peretsman (1986).
[c]Concentrations in mmol/kg measured in overflow aliquots have been adjusted to the chlorinity of the prime aliquot.

The results are shown in Table 11 and in Figures 23 to 31. Total carbon (TC) values are generally about 0.5% for all three holes, with higher values up to 3.5% restricted mainly to the top 20 mbsf. All three holes show a systematic decrease with depth in TC within the top 20 mbsf (Figs. 23 to 25). This drop in TC within the uppermost sediments is due to decreases in both organic carbon with depth via microbial metabolism and to decreases in carbonate (Figs. 29 to 31).

Two maxima in inorganic carbon are apparent at depths of 12 to 18 mbsf and 25 to 30 mbsf in Hole 855A (Fig. 29). The maxima in the shallower interval is accompanied by high total organic carbon (TOC), while in the deeper interval, the TOC either remains approximately constant or decreases. The shallower peak in inorganic carbon is accompanied by a corresponding increase in the C/S ratio (Fig. 26). However, in Hole 855B, the C/S ratio correlates better with TOC rather than with inorganic carbon (compare

Table 8 (continued).

Sample[a]	Core, section, interval (cm)	Depth (mbsf)	Volume (mL)	Squeeze pressure (psi)	Mg[b] (mmol/kg)	Ca[b] (mmol/kg)	Si (µmol/kg)	NH_4 (µmol/kg)	Phosphate (µmol/kg)
Surface seawater (22 July 1991)					49.54				
Core top water (Core 139-855A-1R)					50.24	9.67	64.4	0	0.0
Bottom seawater (calculated for 541 mmol/kg chlorinity)					52.71	10.17	183		
	139-855A-								
IW-1	1R-1, 55–70	0.63	21	12000	50.47	9.97	501		10.8
IW-2	1R-1, 144–150	1.47	39	12000	50.36	10.08	458	47	10.3
IW-3	1R-2, 53–67	2.10	16	5000	49.61	10.09	418		10.8
IW-4	1R-2, 144–150	2.97	50	5000	49.42	10.07	488	252	
IW-5	1R-4, 144–150	5.97	22	5000	49.54	10.05	536	340	23.7
IW-6	2R-4, 140–150	13.55	39	8000	49.99	10.13	648	607	27.5
IW-7	3R-2, 140–150	19.55	49	10000	48.60	10.24	640	490	22.6
IW-8	4R-3, 140–150	30.45	44	12000	49.57	11.71	691	428	10.1
BC-9	5I-1, 74–97	36.35	10	—	50.50	12.49	768	187	
[c]BO-9	5I-1, 74–97	36.35	125	—	49.83	11.98	560		
IW-10	5R-1, 140–150	36.95	42	10000	49.76	12.21	744	250	8.4
IW-11	6R-1, 140–150	46.95	50	6000	51.37	12.24	824	164	3.8
IW-12	7R-2, 140–150	58.05	47	9000	52.08	11.59	935	57	2.8
IW-13	8R-1, 10–12	64.91	2	10000		11.14	712		
	Depth to basalt	74							
	139-855B-								
IW-1	2R-1, 140–150	7.15	52	5000	49.43	10.25	716		
IW-2	4R-3, 140–150	28.95	46	5000	48.91	10.78	636	321	18.5
IW-3	4R-4, 130–144	30.37	14	16000	49.07	11.26	664		10.7
IW-4	4R-5, 132–147	31.90	12	12000	50.14	11.57	618		7.3
	Depth to basalt	45							
	139-855C-								
IW-1	1R-1, 40–52	0.46	16		49.23	9.69	518		
IW-2	1R-1, 144–150	1.47	31	10000	50.49	9.81	366	86	7.5
IW-3	1R-2, 144–150	2.97	47	6000	49.86	9.90	475	296	28.7
IW-4	1R-4, 144–150	5.97	46	7000	49.80	9.66	573	386	33.6
IW-5	2R-2, 140–150	11.65	50	7000	49.91	9.65	607	499	29.0
IW-6	2R-5, 140–150	16.15	49	8000	48.97	9.64	695	509	34.6
IW-7	3R-1, 140–150	19.15	42	10000	48.46	10.25	614		
IW-8	3R-4, 140–150	23.65	49	10000	48.97	11.13	626	517	10.9
IW-9	4R-3, 140–150	31.55	49	7000	48.64	11.34	732	484	8.6
BC-10	5I-1, 74–97	37.45	10	—	48.92	11.80	503	467	9.2
[c]BO-10	5I-1, 74–97	37.45	>80	—	37.04	22.28	323		0.0
IW-11	6R-1, 140–150	47.95	50	5000	48.66	11.53	441	346	4.2
IW-12	6R-6, 140–150	55.45	44	8000	48.38	11.91	624	331	7.0
IW-13	7R-2, 140–150	59.05	50	10000	49.00	13.13	791	360	5.3
IW-14	7R-5, 140–150	63.55	42	10000	48.10	12.81	774	337	4.9
IW-15	8R-1, 70–75	66.43	40	7000	48.91	12.94	732	298	
BC-16	9I-1, 74–97	76.05	10	—	49.21	11.99	971	183	4.5
[c]BO-16	9I-1, 74–97	76.05	>550	—	45.79	13.35	947		
IW-17	9R-1, 0–5	75.23	11	7000	50.53	11.69	854		
IW-18	10R-2, 0–10	86.35	40	16000	51.70	11.96	327	55	0.6
IW-19	10R-3, 140–150	87.85	40	18000	52.82	11.93	244	36	0.3
IW-20	11R-1, 20–33	94.87	5	20000	50.80	12.26	147	40	
IW-21	11R-2, 0–10	96.15	21	18000	51.05	12.23	180	32	
	Depth to basalt	97.5							
	139-855D-								
BC-1	1I-1, 74–97	80.35	10	—	46.46	10.93	443	155	2.0
[c]BO-1	1I-1, 74–97	80.35	200	—	45.52	12.20	369		0.4
IW-2	4R-1, 45–50	104.78	28	17000	50.60	12.15	293	19	0.7
	Depth to basalt	108							

Figs. 27 and 30). In Hole 855C, inorganic carbon and TOC exhibit similar trends, after a rapid decrease in inorganic carbon within the top 10 mbsf (Fig. 31).

Percentages of H, S, and N are relatively consistent from hole to hole and constant with depth in all three holes below 20 mbsf. They generally are in the ranges of 0.4% to 0.6% for hydrogen (presumably derived mainly from water), 0.1 to 0.3% for sulfur, and 0.06 to 0.08% for nitrogen (Figs. 23 to 25). Values falling outside these ranges tend to appear either at the top or bottom of the sediment at each hole, near either the seafloor or the contact with basalt. Examples are the higher percentages of sulfur at the bottom of Hole 855A and of nitrogen in surficial sediments of Holes 855A and 855B. Nitrogen values are slightly higher throughout Hole 855C (0.06% to 0.11%) than in either of the other two holes. Maxima in both C and S are apparent at the bottom of Hole 855A, possibly due to enhanced productivity near the continental shelf; whereas, minima in the C, H, N, and S profiles are apparent in Hole 855C (Fig. 25).

Ratios of C/H, C/S, and C/N (Figs. 26 to 29) show higher values in surficial sediments (less than 20 mbsf) in Holes 855A and 855C. Closely spaced sampling reveals distinct minima and maxima for all three ratios in the upper 20 m of Holes 855A and 855C. All three ratios generally decrease with depth in the top 20 mbsf to reach relatively constant values at greater depths in both Holes 855A and 855C (Figs. 29 and 31). Higher values of C/N occur in the deepest intervals of Holes

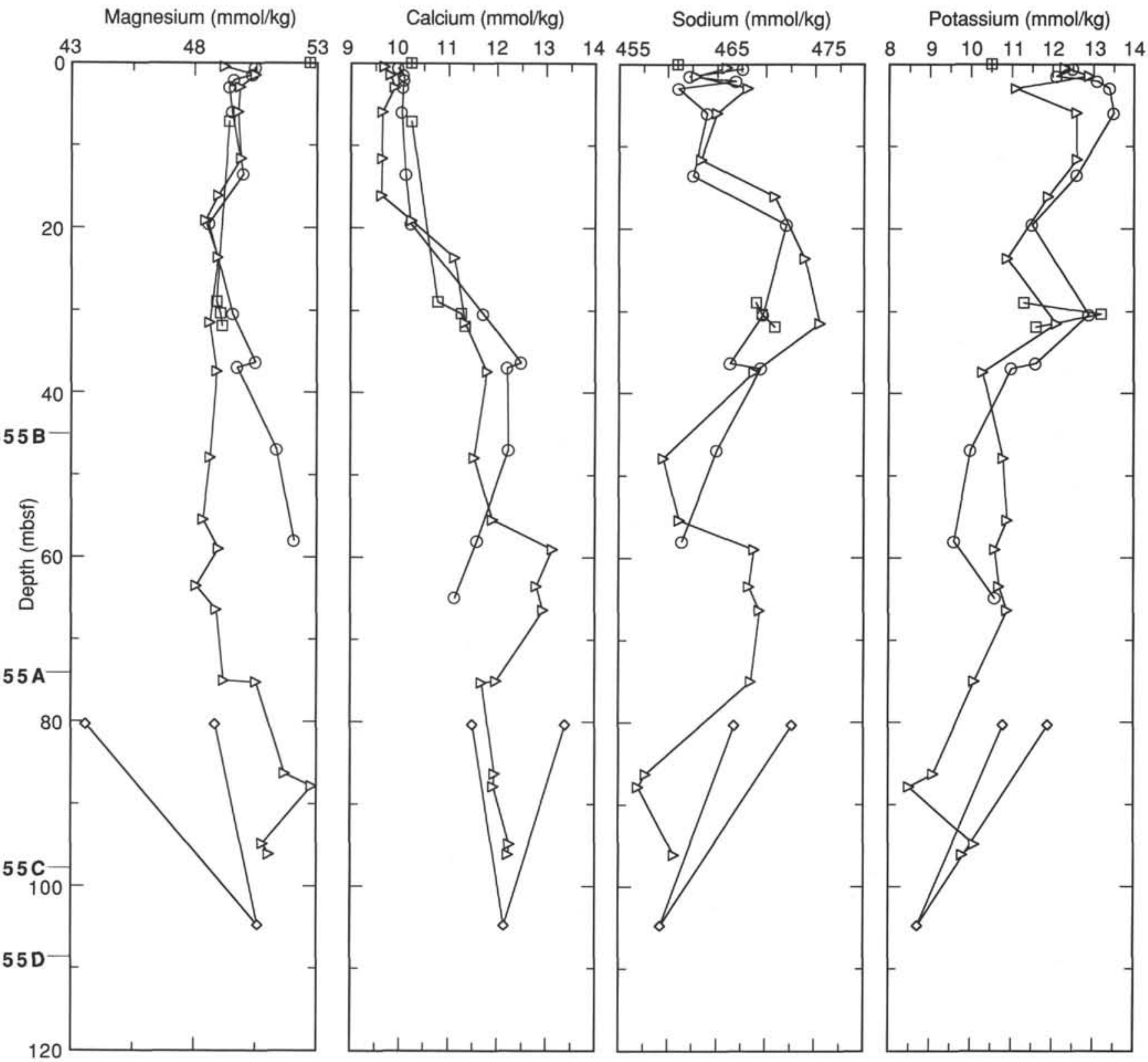

Figure 19. Composition of pore water from sediments at Site 855. Symbols as in Figure 18.

855A and 855C, and of C/H in Hole 855A. For Hole 855A, the ratios may reflect thermal effects due to the underlying basalt.

The percentage of CO_2 in the headspace gas is plotted along with the carbon data in Figures 30 and 31 for Holes 855B and 855C, respectively. The decrease in CO_2 in Hole 855B at 40 mbsf (Fig. 30) appears to be accompanied by a corresponding decrease in both inorganic and organic carbon. However, the case is not strong due to the limited CO_2 data set. A similar plot for Hole 855C (Fig. 31) does not show any significant correspondence between profiles of CO_2 vs. organic or inorganic carbon.

SEDIMENT GEOCHEMISTRY AND ALTERATION

Heat flow at Site 855 is lower than at the other Middle Valley drill sites. Therefore, the chemical and mineralogical changes that accompany enhanced thermal diagenesis and/or hydrothermal alteration are likely to be less important at this site. Sediment geochemistry from this site is considered to represent an "unaltered background" to which chemical alteration of sediment at other drill sites can be compared. Finer grained, homogeneous samples typically were selected for chemical analysis, thus biasing the geochemical sampling against the less abundant detrital sand component of the turbiditic sediment. Silt deposited by turbidity currents was sampled, as was silty clay and clay that came from both the finer grained upper portions of turbidites and the hemipelagic sediment that accumulated between turbidity-current deposition events. These two components cannot always be distinguished reliably by subtle color differences (see "Lithostratigraphy and Sedimentology" section, this chapter), and are therefore not differentiated in the geochemical data set presented.

The utility of this site as a "geochemical reference" site is somewhat compromised by the relatively thin sediment cover penetrated before reaching basement. Furthermore, core disturbance by rotary drilling and poor core recovery at this site make detailed lithologic correlation between this and the other Middle Valley sites difficult.

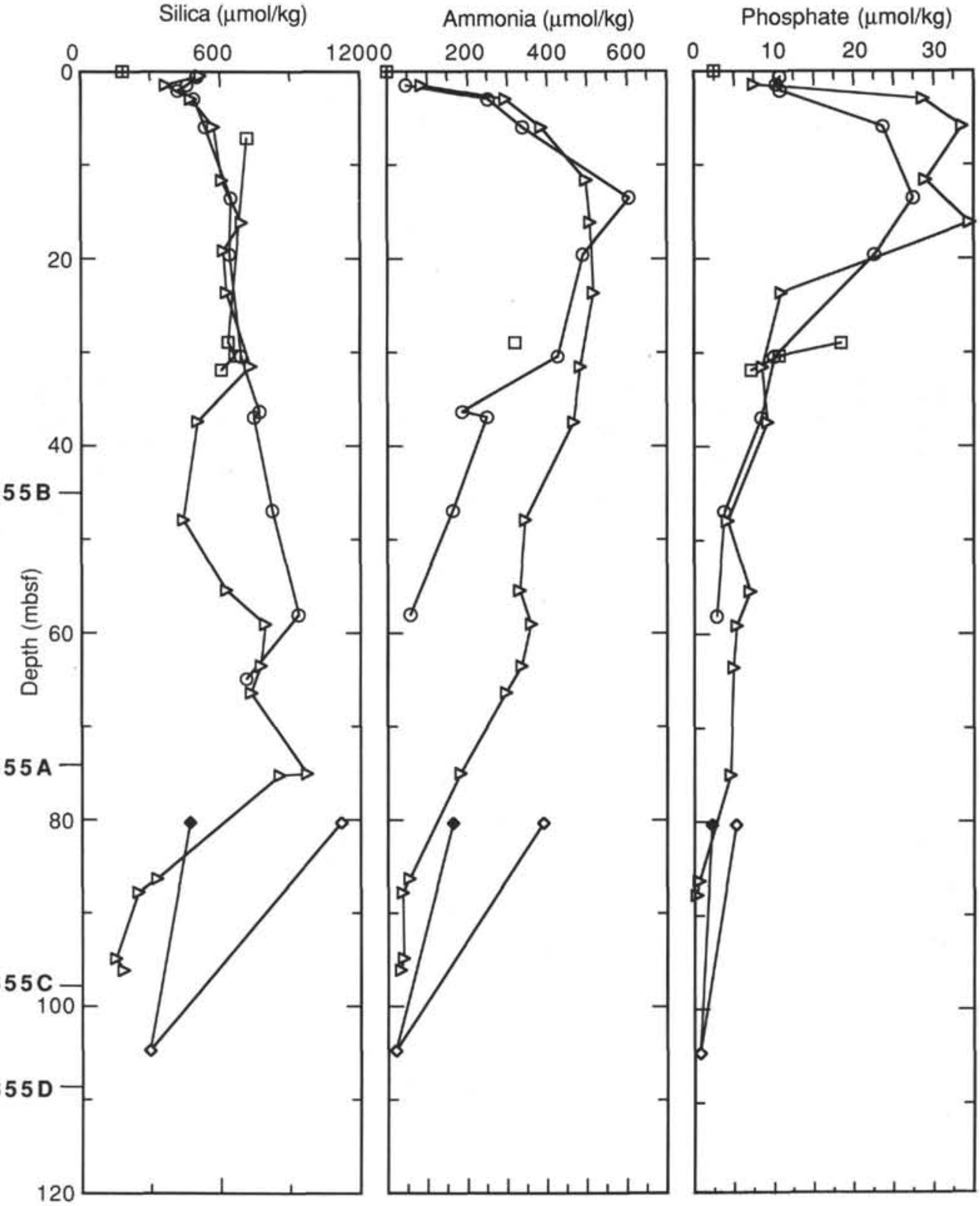

Figure 20. Composition of pore water from sediments at Site 855. Symbols as in Figure 18.

Correlation of geochemical variations between Holes 855A, 855B, and 855C is not possible because samples from corresponding depth intervals in each hole were not analyzed. The proximity of the holes to one another justifies treating the combined data set from Holes 855A through 855C as a vertical profile through the sediment, as a first approximation.

Smear-slide petrography and bulk-sediment X-ray diffraction (XRD) analysis indicate that the coarser grained sedimentary fraction consists predominantly of quartz and plagioclase feldspar, with subordinate amounts of chlorite, mica, amphibole, and clay. The clay-size fraction is composed predominantly of chlorite, illite, and quartz. Mineralogy of selected sediment samples, determined by XRD, is presented in Table 12. Major element chemical analyses are presented in Table 13 and minor element analyses are presented in Table 14. Analytical methods are presented in the "Sediment Alteration and Geochemistry" section, "Explanatory Notes" chapter (this volume). The average composition of the sediment is approximately 59% SiO_2, 16% Al_2O_3, 7.6% Fe_2O_3, 3.7% MgO, 4.0% CaO, 2.4% Na_2O, and 2.0% K_2O.

No systematic downhole variations in sediment geochemistry are apparent at Site 855. The exception is a decrease in inorganic carbon, interpreted to be dominantly biogenic calcium carbonate, below 20 mbsf (see "Organic Geochemistry" section, this chapter). The covariation of elements is interpreted to indicate an essentially binary mixing of a coarse clastic component, dominated by quartz and feldspar, and a clay-size component dominated by chlorite and mica. Interelement correlation between SiO_2, CaO, Na_2O, Sr, and Zr presumably relates to codeposition of quartz, plagioclase, and zircon in the coarser detritus of turbidites (Fig. 32). These elements are most enriched in the silt samples. Covariation of Al_2O_3, TiO_2, Fe_2O_3, MgO, K_2O, H_2O, Cu, and Zn is interpreted to represent the clay-size fraction of turbidite and hemipelagic units that are rich in clay minerals, and these elements are most enriched in the clay and silty clay samples (Fig 33). Most

Table 9. Composition of headspace gases in sediments from Site 855.

Sample (cm)	Depth (mbsf)	Methane[a] (ppm)	Ethane (ppm)	CO_2 (ppm)	CO_2 (%)	H_2S	Other
Lab air		3.0	0.0	n.d.	—	0.0	—
139-855A-							
5R-2, 0–5	37.05	4.0	0.0	n.d.	—	0.0	—
6R-2, 0–5	47.05	3.0	0.0	n.d.	—	0.0	—
7R-2, 0–5	56.60	3.0	0.0	n.d.	—	0.0	—
139-855B-							
2R-2, 0–5	7.20	4.5	0.0	60969	6.1	0.0	Air
4R-4, 0–5	29.00	4.0	0.0	n.d.	—	0.0	—
5R-5, 0–5	40.00	4.0	0.0	39090	3.9	0.0	Air
6R-1, 0–5	60.80	3.0	0.0	65000	6.5	0.0	Air
139-855C-							
2R-, 0–5	16.20	4.0	0.0	35000	3.5	0.0	Air
3R-3, 0–5	20.70	3.5	0.0	63647	6.4	0.0	Air
4R-3, 0–5	30.10	3.0	0.0	57595	5.8	0.0	Air
5R-CC	36.60	3.0	0.0	26732	2.7	0.0	Air
6R-7, 0–5	55.50	3.5	0.0	31432	3.1	0.0	Air
7R-6, 0–5	63.60	5.5	0.0	65161	6.5	0.0	Air
8R-2, 0–5	67.20	3.5	0.0	52089	5.2	0.0	Air
9R-1, 0–1	75.20	3.0	0.0	16448	1.6	0.0	Air
10R-3, 0–5	87.90	3.5	0.0	23700	2.4	0.0	Air
11R-1, 145–150	96.05	2.5	0.0	20700	2.1	0.0	Air
139-855D-							
1R-1, 0–5	79.55	3.2	0.0	21900	2.2		Air

Notes: All samples measured using the headspace technique. n.d. = not determined. — = not applicable.
[a]Concentrations of gases are by volume.

of the trace elements are correlated with the clay-size material, as is loss on ignition. Sediment from this site also appears to have a consistent Zn to Cu ratio of approximately 1.8:1 (Fig. 34). This parameter is potentially useful for evaluating the sediment contribution to the base metal values of the massive sulfide deposit drilled at Site 856.

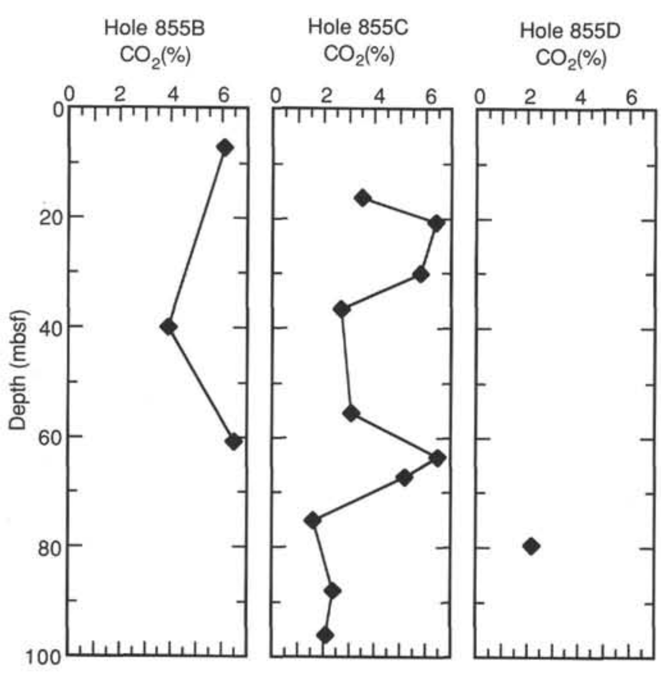

Figure 21. Concentrations of free carbon dioxide in headspace gas evolved at 60°C vs. depth for Holes 855B, 855C, and 855D.

IGNEOUS PETROLOGY AND GEOCHEMISTRY

Drilling penetrated basaltic rocks in Holes 855A, 855B, 855C, and 855D. The purpose of drilling at this site was to characterize the normal fault that forms the eastern topographic boundary of Middle Valley. This structure may localize either downflow or upflow of seawater. The average basalt recovery was only 8%, and much of this was small "rollers" that could have been from talus piles. With this proviso, a general correlation of samples among adjacent holes has been attempted. The distribution of the holes with respect to the fault and the recovered basalt is illustrated in Figures 35 and 36. The recovered samples are all remarkably fresh, retaining abundant fresh glass and having secondary minerals restricted to a few filled vesicles. The deepest rocks recovered from Hole 855D had fracture fill of greenschist mineralogy, but petrographic examination revealed no substantial penetrative metamorphism or replacement.

Distribution of Holes and Recovery of Basement

The four holes from Site 855 form a transect across the normal fault. The results from each hole are described from east to west (Fig. 35) and these results are summarized in Table 15. These two holes are separated by only 30 m and the recovered basalt samples are quite similar. Holes 855A and 855B terminated in basalt, presumably basement (Fig. 35). Hole 855B (Section 139-855B-8R-CC) intersected basement at 45 mbsf and continued to 63 mbsf for a total basement penetration of 18 m. A basalt fragment found at the top of Section 139-855C-1R-1 is considered part of Hole 855B, as it was likely lodged in the bit following drilling of the previous hole. Hole 855A intercepted basement at 74 mbsf (bottom of Section 139-855A-8R-1) and cored to 77 mbsf (Section 139-855A-9R-1) for a total penetration of 3 m into basement. The recovery of Section 139-855A-9R-1 was almost 16%, the highest of any basaltic core from this site.

Holes 855C and 855D are located 125 m west of the base of the fault scarp, and 55 m west of Hole 855A (Fig. 35). At Hole 855C, basement was intersected at 98 mbsf and cored to a depth of 106.9 mbsf for a total penetration of 9 m. Basalt was recovered only in the interval between 101 and 107 mbsf (Section 139-855C-12R-CC) with recovery of only 0.4% (a single piece). At Hole 855D, basalt was intersected at a depth of 108 mbsf (Section 139-855D-5R-1) and cored to a total depth of 118.6 mbsf (Section 139-855D-6R-1) for a total penetration of 11 m into basement. The recovery for these two basement cores, 139-855D-5R and -6R, was 4.4% and 10.6%, respectively.

Although coring in these four holes did not recover a large quantity of basement rocks, the variety of petrological types and the freshness of the rocks do permit petrologic characterization of the local basement. The typically small pieces and abundant rounded pebbles suggest that the piece numbers may not be in proper stratigraphic order. This is especially true for the core-catcher samples.

General Description and Lithologic Units

Lithologic units were distinguished on the basis of proportion of phenocryst phases; their distribution among the cores is summarized in Figure 36. Samples ranged from highly porphyritic basalt to aphyric basalt. Unit 1 was recognized in both of the eastern holes and is typified by samples from Sections 139-855A-8R-1 (Pieces 1–4), 139-855B-8R-CC (Pieces 1–2, 4–6), and 139-855C-1R-1 (Piece 1). This unit is composed of very fresh porphyritic basalt, with abundant large plagioclase and olivine phenocrysts. The rocks are classified as either highly or moderately phyric. The plagioclase phenocrysts are tabular to equant, present in abundances of 8%–25% and up to 4 mm in length. Olivine phenocrysts are conspicuous and form up to 10% of the rock by volume, and with crystals up to 3 mm in size. Olivine phenocrysts are less abundant than plagioclase, in proportions of 2–3:1. Large clinopyroxene phenocrysts are less abundant and less

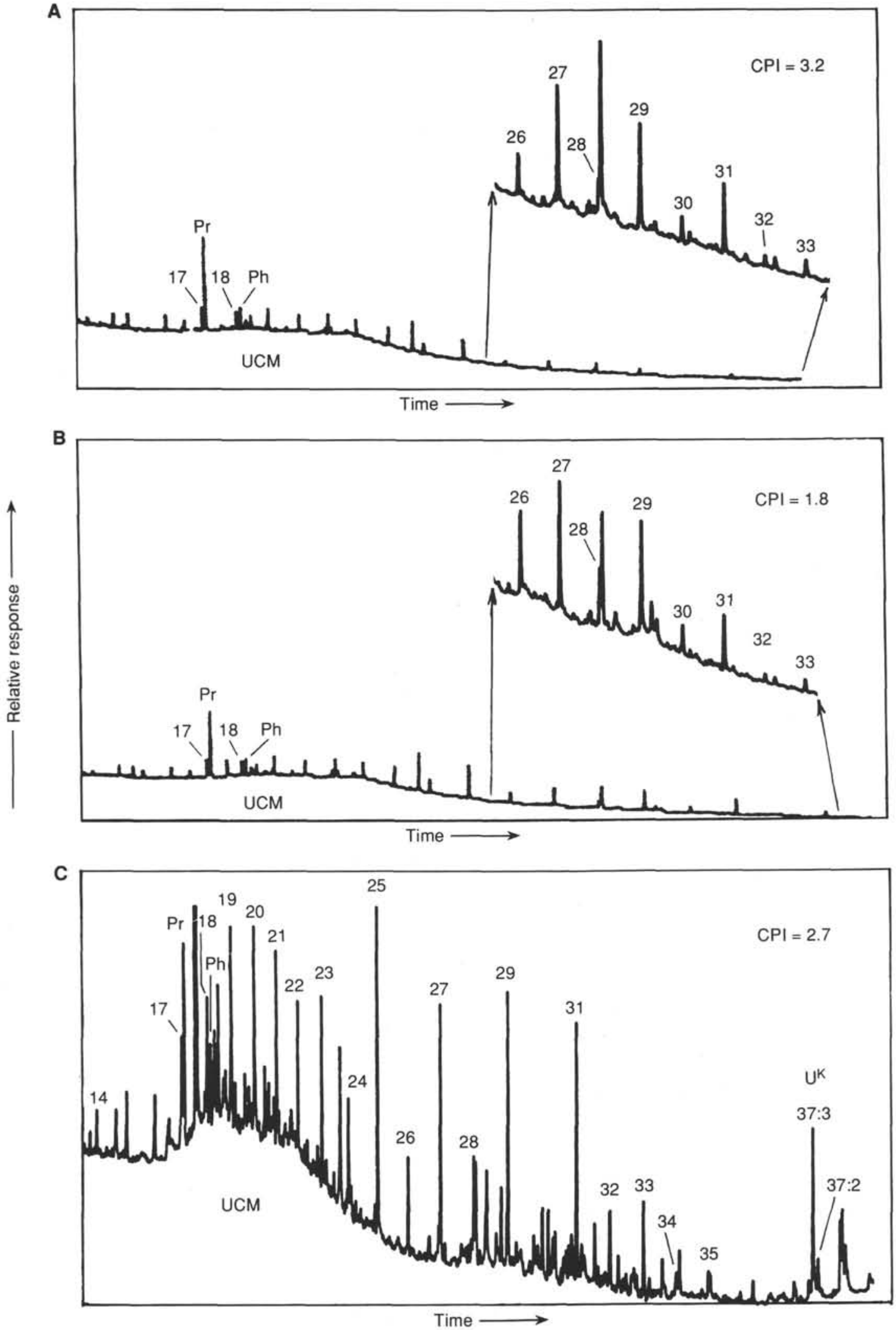

Figure 22. Gas chromatographic traces of the bitumen (hexane soluble matter) in sediments from Site 855. **A.** Sample 139-855A-6R-CC. **B.** Sample 139-855C-10R-CC. **C.** Sample 139-855D-4R-CC. Numbers refer to carbon chain length of *n*-alkanes. Pr = pristane, Ph = phytane, U^K = unsaturated ketones, 37:2 = C_{37} alkadien-2-one, 37:3 = C_{37} alkatrien-2-one, UCM = unresolved complex mixture of branched and cyclic compounds, CPI = carbon preference index.

Table 10. Various parameters for the solvent soluble organic matter in sediments from Site 855.

Core, section, interval (cm)	Depth (mbsf)	Relative yield ($\times10^6$)	Carbon maxima[a]	$CPI_{(26-35)}$	Pr/Ph	Pr/n-C_{17}	Ph/n-C_{18}	U^K_{37}
139-855A-								
1R-1, 77–79	0.78	58.0	17,29	2.97	1.13	0.45	0.67	0.32
1R-3, 114–116	4.15	27.6	17,31	3.03	1.78	0.67	0.68	0.22
2R-2, 106–108	10.17	20.8	17,29	2.49	2.31	0.37	0.47	0.30
3R-3, 78–80	20.39	15.1	17,27	1.90	2.50	0.50	0.42	n.d
4R-3, 31–33	29.32	35.3	17,29	2.91	1.70	0.56	0.73	0.31
5R-1, 100–103	36.52	39.9	17,29	1.71	1.21	0.40	0.43	0.31
6R-CC	55.10	26.4	Pr,27	3.20	5.00	4.21	1.29	n.a.
7R-3, 43–46	58.55	30.2	17,27	2.67	1.81	0.67	0.86	0.46
139-855B-								
4R-3, 99–102	28.51	16.5	17,29	2.77	1.56	0.50	0.62	0.30
6R-1, 25–29	44.17	48.6	17,27	2.12	1.45	0.48	0.87	0.29
139-855C-								
1R-1, 66–69	0.68	117.2	17,27	2.27	1.33	0.24	0.69	0.34
1R-5, 65–67	6.66	44.3	17,29	2.15	1.14	0.16	0.82	0.26
2R-4, 67–71	13.89	39.7	17,29	2.45	0.80	0.40	0.53	0.29
3R-4, 73–75	22.94	35.6	17,29	2.71	1.58	0.60	0.49	0.23
6R-CC	56.10	2.5	29,17	2.78	1.70	0.85	0.59	0.27
7R-4, 69–73	61.31	35.9	17,29	4.05	1.47	0.47	0.59	0.25
10R-3, 0–5	87.93	36.8	Pr,29	1.59	3.45	3.33	1.12	0.14
10R-4, 78–82	90.20	31.4	Pr,29	2.22	2.38	3.33	1.20	0.18
10R-CC	94.60	12.2	Pr,29	1.80	4.28	4.00	1.17	n.a.
11R-1, 145–150	96.08	5.9	17,29	1.80	1.79	0.92	1.16	0.23
139-855D-								
4R-1, 0–5	104.33	58.3	Pr,29	1.34	4.55	4.00	1.10	0.14
4R-CC	108.50	38.8	29,Pr	2.66	2.50	1.82	0.67	0.17

Notes: n.d. = not detected, n.a. = not analyzed.
[a]Major homologs are listed in decreasing order of intensity (C_{max}).

conspicuous than those of plagioclase or olivine. Clinopyroxene is observed as an oikocryst with included plagioclase as ellipsoidal, partially resorbed xenocrysts and in glomerocrystic aggregates with the other phenocrysts. Clinopyroxene is present in volumes less than 5%, and ranges in size from 0.5 to 3.5 mm. The sparse distribution of the larger pyroxene crystals limited the identification of this mineral in hand sample, and it may therefore be present in more of the Unit 1 samples than represented in the visual core descriptions. The matrix is typically aphanitic to fine-grained, with crystallites of plagioclase and Fe-Ti oxides. Many samples appear to be from either the glassy margin of pillows or massive flows, or the microcrystalline portion just below the margin.

Unit 2 is characterized by less abundant phenocrysts, much smaller olivine phenocrysts, and a more crystalline matrix compared to Unit 1. Some samples are megascopically aphyric. The rocks are classified as aphyric to slightly porphyritic basalts with plagioclase as the dominant phenocryst. In many samples, plagioclase is the only mega-scopically visible phenocryst; in general, plagioclase is more abundant than olivine by a ratio of 3:1. Samples included in this unit include Section 139-855A-8R-1, Piece 5, all of Section 139-855A-9R-1, the single piece from Section 139-855C-12R-CC, all of Section 139-855D-5R-1, and Section 139-855D-6R-1, Pieces 1–5. The grain-size range of the partly crystalline groundmass overlaps that of the phenocrysts, making the distinction between the two populations difficult. Olivine varies in size from 0.05 mm to 1 mm and is typically partially altered to carbonate and phyllosilicate minerals. It is present in volume percentages of 0%–2% based on megascopic description. The grains are rounded to anhedral. Plagioclase phenocrysts are present in quantities of 0%–5% and sized from 0.5–1.5 mm. The plagioclase phenocrysts are more sodic in composition than those from Unit 1, with a range of compositions from An_{50} (small grains in Section 139-855D-5R-1, Piece 8) to An_{80} (large tabular grains in Section 139-855A-9R-1, Piece 3). The crystals are typically tabular to lathlike, and generally overlap the microphenocrysts. Aphyric basalt samples have a groundmass of plagioclase microphenocrysts and microlites. Plagioclase is occasionally observed in glomerocrystic aggregates. Clinopyroxene is only rarely visible megascopically (e.g., Section 139-855A-9R-1, Piece 3) because it is small and sparse. It is anhedral and is found as rare oikocrysts with included plagioclase or as spherulitic aggregates in the groundmass. The groundmass texture is typically intersertal, with abundant microlitic or microcrystalline plagioclase, and with glass, clinopyroxene, and magnetite as mesostasis phases. The groundmass is cryptocrystalline to fine-grained.

Unit 3 is distinguished only in the lower half of Section 139-855D-6R-1 (Pieces 6–8). These rocks are plagioclase-phyric with prominent (1–2 mm) plagioclase phenocrysts as stubby laths or long thin blades. Plagioclase is present in volume percentages from 0.5%–2%. The matrix contains megascopically visible crystals of plagioclase, clinopyroxene, and oxide, probably magnetite.

Petrographic Descriptions

Three samples from Unit 1, three samples from Unit 2, and no samples from Unit 3 were selected for petrographic analyses. Modal proportions from representative samples are presented in Table 16. The samples from Unit 1 include two from Section 139-855A-8R-1 (Piece 1, 18–20 cm; Piece 2, 21–23 cm) and one from Section 139-855B-8R-CC (Piece 4, 17–19 cm). The samples studied are all fresh porphyritic basalts with large (1–3 mm) euhedral plagioclase and large (0.5–5 mm) ovoid to euhedral olivine crystals (Fig. 37). The matrix is fresh glass and plagioclase microlites or skeletal grains. The

Table 11. Elemental analyses of total C, H, N, and S for Site 855.

Sample (cm)	Depth (mbsf)	C (%)	H (%)	S (%)	N (%)	C/H[a]	C/N[a]	C/S[a]	Inorganic C (%)	TOC (%)
139-855A-										
1R-1, 77–79	0.79	1.32	0.52	0.34	0.120	2.54	11.0	3.9	2.40	0.00
1R-2, 104–106	2.54	0.93	0.57	0.11	0.068	1.63	13.7	8.5	n.d.	—
1R-2, 104–106	2.54	1.01	0.39	0.02	0.050	2.59	20.2	50.5	0.50	0.51
1R-3, 114–116	4.14	1.05	0.44	0.16	0.036	2.39	29.2	6.6	0.54	0.51
[b]1R-4, 111–114	5.61	0.94	0.56	0.10	0.069	1.68	13.6	9.4	0.36	0.58
1R-4, 111–114	5.61	0.77	0.56	0.18	0.051	1.38	15.1	4.3	0.38	0.39
1R-5, 38–40	6.38	1.08	0.51	0.29	0.089	2.12	12.1	3.7	0.57	0.51
2R-1, 35–38	9.45	1.65	0.54	0.17	0.071	3.06	23.2	9.7	0.87	0.78
2R-2, 43–45	9.53	0.72	0.50	0.17	0.083	1.44	8.67	4.2	0.34	0.38
2R-2, 43–45	9.53	0.68	0.38	0.17	0.032	1.79	21.3	4.0	0.34	0.34
2R-2, 106–108	10.16	0.99	0.65	0.22	0.160	1.52	6.2	4.5	0.47	0.52
2R-2, 106–108	10.16	0.87	0.42	0.15	0.084	2.07	10.4	5.8	0.47	0.40
[b]2R-3, 42–44	11.02	0.85	0.34	0.00	0.043	2.50	19.8	—	0.57	0.28
2R-3, 42–44	11.02	0.86	0.48	0.00	0.072	1.79	11.9	—	0.57	0.29
2R-3, 42–44	11.02	0.83	0.28	0.00	0.084	2.96	9.9	—	n.d.	—
2R-3, 42–44	11.02	0.86	0.40	0.00	0.049	2.15	17.6	—	n.d.	—
2R-4, 37–39	12.47	0.87	0.66	0.30	0.170	1.32	5.1	2.9	0.15	0.72
2R-4, 37–39	12.47	0.84	0.48	0.12	0.082	1.75	10.2	7.0	n.d.	—
2R-4, 111–113	13.21	0.86	0.43	0.30	0.150	2.00	5.7	2.9	0.43	0.43
2R-4, 111–113	13.21	0.75	0.31	0.19	0.050	2.42	15.0	4.0	n.d.	—
2R-5, 42–46	14.02	1.08	0.41	0.27	0.058	2.63	18.6	4.0	0.57	0.51
2R-5, 90–92	14.50	2.97	0.61	0.13	0.120	4.87	24.8	22.8	1.90	1.07
2R-5, 90–92	14.50	2.56	0.50	0.05	0.061	5.12	42.0	50.2	n.d.	—
3R-1, 79–81	17.39	1.88	0.50	0.18	0.160	3.76	11.8	10.4	1.33	0.55
3R-1, 79–81	17.39	1.80	0.47	0.05	0.064	3.83	28.1	35.3	n.d.	—
3R-2, 0–2	18.10	0.67	0.71	0.17	0.098	0.94	6.8	3.9	n.d.	—
3R-2, 80–82	18.90	0.58	0.59	0.18	0.046	0.98	13.0	3.2	0.12	0.46
3R-3, 78–80	20.38	0.47	0.53	0.31	0.070	0.89	6.7	1.5	0.03	0.44
4R-1, 46–48	26.46	0.69	0.61	0.22	0.065	1.13	10.6	3.1	0.32	0.37
4R-2, 29–32	27.79	n.d.	n.d.	n.d.	n.d.	—	—	—	1.12	—
4R-3, 31–33	29.30	0.43	0.31	0.20	0.044	1.39	9.8	2.2	1.39	0.00
4R-4, 65–67	31.15	0.77	0.48	0.21	0.100	1.60	7.7	3.7	0.22	0.55
5R-1, 100–103	35.60	0.46	0.55	0.18	0.079	0.84	5.8	2.6	0.10	0.36
6R-2, 34–37	47.34	0.46	0.40	0.26	0.071	1.15	6.5	1.8	0.14	0.32
7R-1, 102–104	56.12	0.39	0.43	0.10	0.052	0.91	7.5	4.1	0.14	0.25
7R-2, 113–116	57.73	1.82	0.56	0.61	0.078	3.25	23.3	3.0	1.17	0.65
7R-3, 43–46	58.53	1.56	0.60	0.66	0.063	2.60	24.8	2.4	0.66	0.90
139-855B-										
2R-2, 30–36	7.50	3.44	0.40	0.24	0.060	8.60	135.0	14.3	2.25	1.19
4R-1, 99–102	25.49	0.65	0.54	0.15	0.078	1.20	22.0	4.3	0.14	0.51
4R-2, 99–100	27.00	0.48	0.48	0.17	0.032	1.00	35.0	2.8	0.11	0.37
4R-4, 99–102	29.99	0.49	0.39	0.32	0.074	1.26	7.0	1.5	0.18	0.31
5R-1, 25–29	34.25	0.32	0.23	0.19	0.041	1.39	21.0	1.7	0.16	0.16
6R-1, 25–29	44.15	0.46	0.47	0.26	0.067	0.98	18.0	1.8	0.22	0.24
139-855C-										
1R-1, 66–69	0.66	1.38	0.53	0.26	0.100	2.60	34.0	5.3	0.75	0.63
1R-4, 65–67	5.15	1.41	0.41	0.32	0.082	3.44	43.0	4.4	0.86	0.55
1R-5, 65–67	6.65	1.20	0.47	0.24	0.080	2.55	37.0	5.0	0.65	0.55
2R-1, 69–73	9.39	1.29	0.52	0.03	0.070	2.48	39.0	39.1	0.59	0.70
2R-2, 70–74	10.90	0.78	0.47	0.14	0.066	1.66	26.0	5.6	0.22	0.56
2R-3, 79–83	12.49	0.85	0.49	0.26	0.100	1.73	21.0	3.3	0.15	0.70
2R-4, 67–71	13.87	0.87	0.44	0.12	0.052	1.98	36.0	7.3	0.38	0.49
2R-5, 70–74	15.40	0.83	0.45	0.20	0.085	1.84	26.0	4.2	0.35	0.48
2R-5, 70–74	15.40	0.80	0.40	0.16	0.049	2.00	34.0	5.0	0.35	0.45
2R-6, 71–75	16.91	0.74	0.40	0.07	0.067	1.85	24.0	11.4	0.30	0.44
3R-1, 59–61	18.29	1.32	0.55	0.04	0.080	2.40	38.0	36.7	0.58	0.74
3R-3, 70–72	21.40	0.58	0.51	0.24	0.110	1.14	14.0	2.4	0.10	0.48
4R-2, 130–132	29.90	0.56	0.42	0.27	0.090	1.33	17.0	2.1	0.23	0.33
4R-3, 110–112	31.20	0.51	0.44	0.22	0.060	1.16	21.0	2.3	0.13	0.38
6R-2, 77–79	48.77	0.68	0.48	0.28	0.100	1.42	18.0	2.4	0.19	0.49
6R-5, 76–80	53.26	0.50	0.41	0.20	0.057	1.22	23.0	2.5	0.16	0.34
6R-6, 69–71	53.69	0.61	0.40	0.28	0.090	1.53	18.0	2.2	0.25	0.36
7R-1, 76–80	56.86	0.41	0.63	0.28	0.075	0.65	15.0	1.5	0.06	0.35
7R-3, 79–83	59.89	0.54	0.49	0.29	0.075	1.10	19.0	1.9	0.12	0.42
7R-6, 78–82	64.38	0.88	0.51	0.31	0.100	1.73	22.0	2.8	0.45	0.43
8R-1, 44–46	66.14	0.44	0.54	0.21	0.068	0.81	17.0	2.1	0.07	0.37
8R-2, 33–36	67.53	0.43	0.48	0.22	0.053	0.90	22.0	2.0	0.10	0.33
10R-1, 74–78	85.64	0.76	0.52	0.17	0.120	1.46	17.0	4.5	0.27	0.49
10R-4, 78–82	90.18	0.69	0.64	0.26	0.084	1.08	22.0	2.7	0.23	0.46
10R-5, 43–47	91.33	0.70	0.55	0.24	0.066	1.27	28.0	2.9	0.23	0.47
11R-1, 67–70	95.27	0.32	0.25	0.18	0.026	1.28	30.0	1.8	0.21	0.11

Note: n.d. = not determined, — = not applicable.
[a]Calculated as percentage ratios.
[b]Washed.

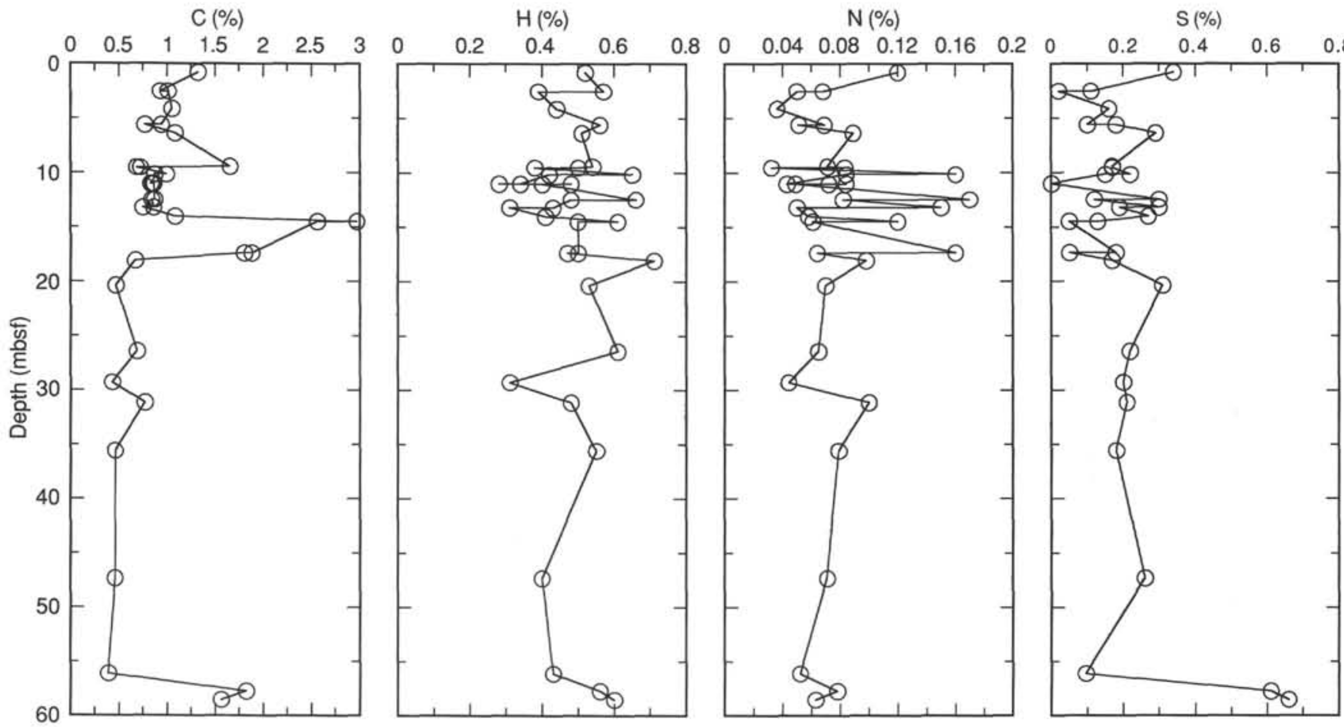

Figure 23. Total carbon, hydrogen, sulfur, and nitrogen vs. depth for Hole 855A.

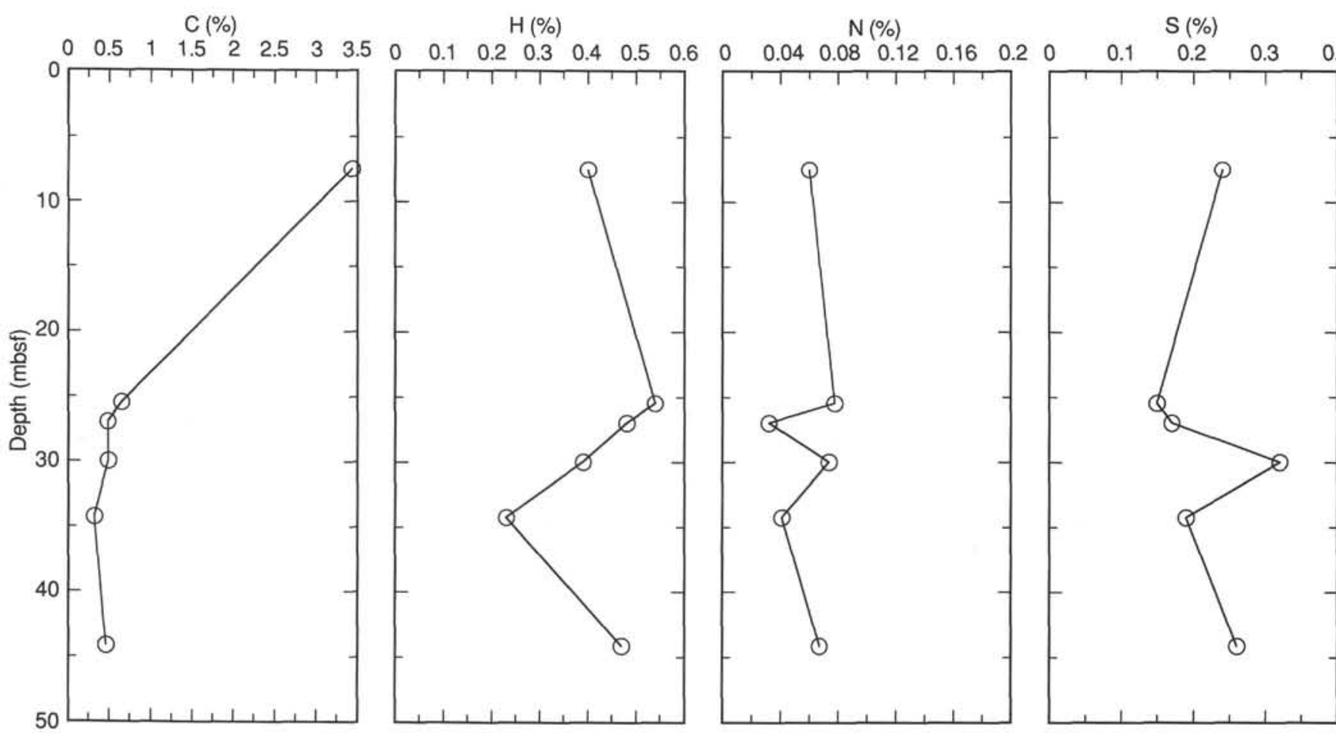

Figure 24. Total carbon, hydrogen, sulfur, and nitrogen vs. depth for Hole 855B.

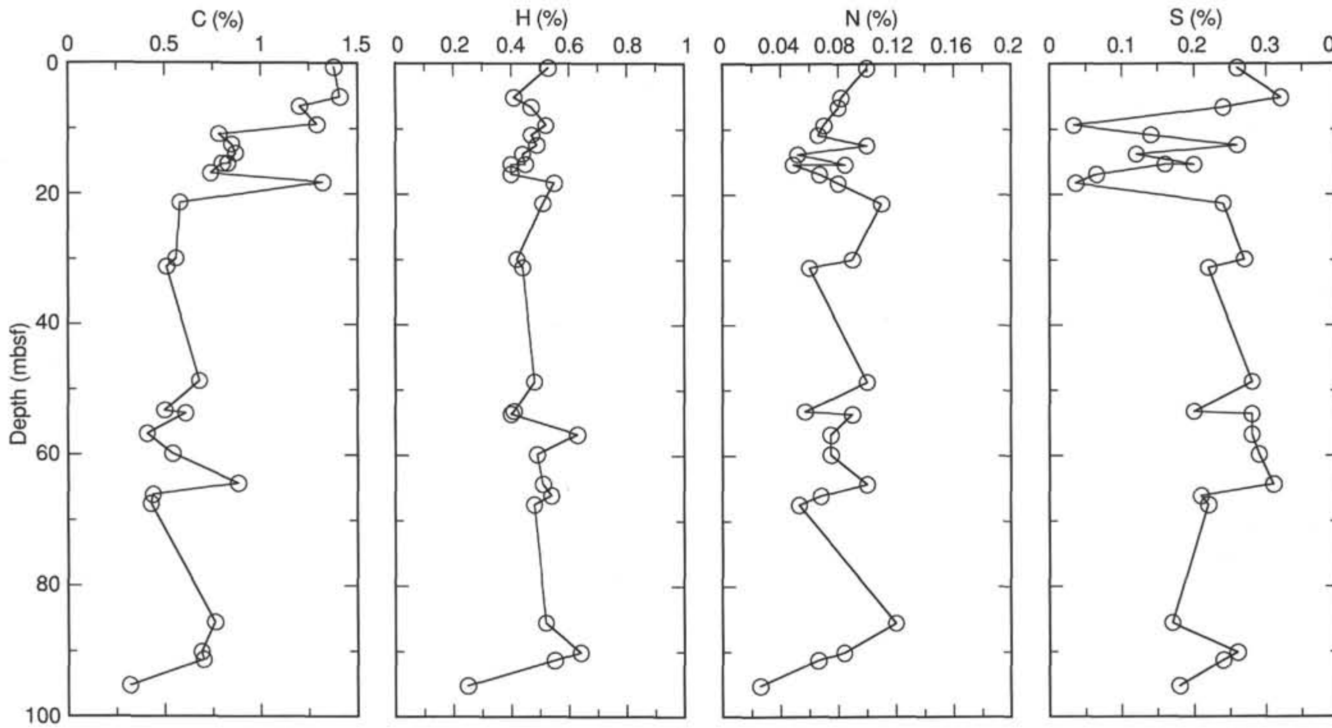

Figure 25. Total carbon, hydrogen, sulfur, and nitrogen vs. depth for Hole 855C.

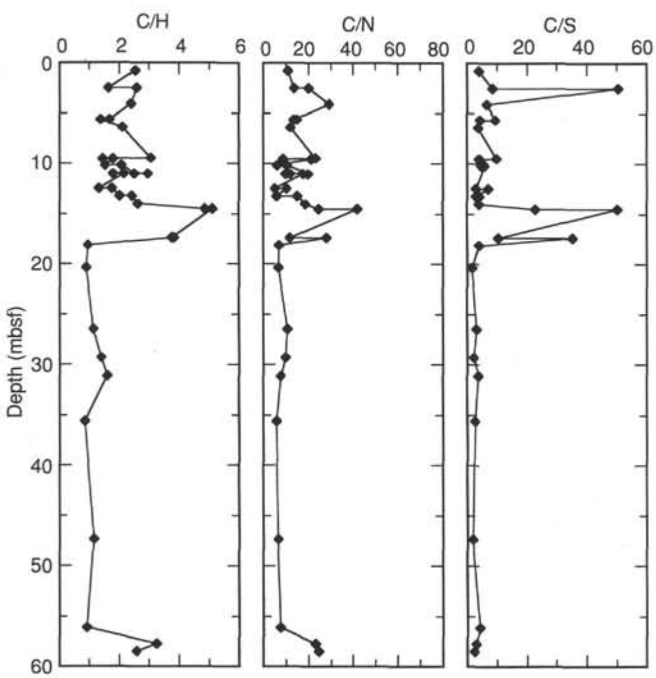

Figure 26. C/H, C/N, and C/S ratios vs. depth for Hole 855A.

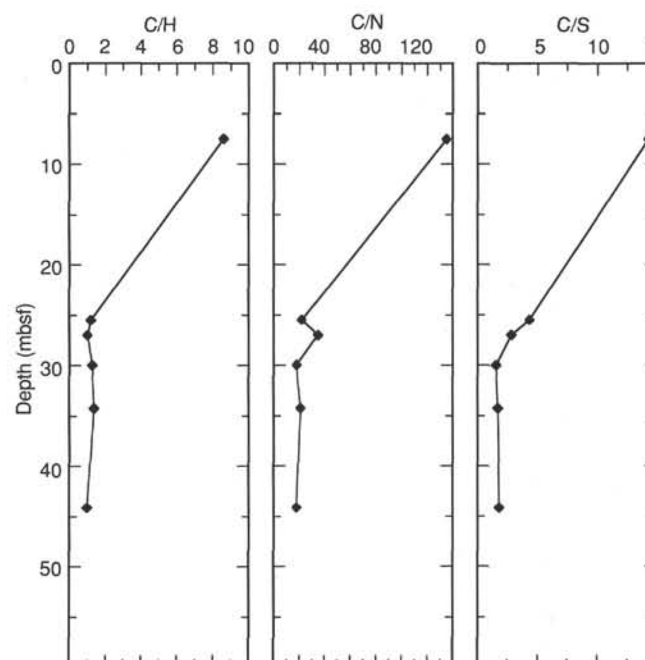

Figure 27. C/H, C/N, and C/S ratios vs. depth for Hole 855B.

plagioclase in the Hole 855A samples is very calcic (An_{78-90}) compared with that in the Hole 855B specimen. The large plagioclase grains in the latter sample, however, have concentric zonation and a composition similar to the groundmass phases (An_{70-75}) in the other two samples. This suggests that the plagioclase in the Hole 855B samples may have changed from an original calcic composition to a more sodic composition through reaction and reequilibration. In support of this hypothesis it is noted that most of the plagioclase phenocrysts in this sample have a thin sodic rim from reequilibration with the enclosing magma. All three samples have either glomerocrysts or poikilitic texture with plagioclase included in large clinopyroxene grains (Fig. 38). In addition the three samples have large (up to 3.5 mm) subhedral to anhedral clinopyroxene grains. The ovoid shape of the clinopyroxene grains (Fig. 39) is reminis-

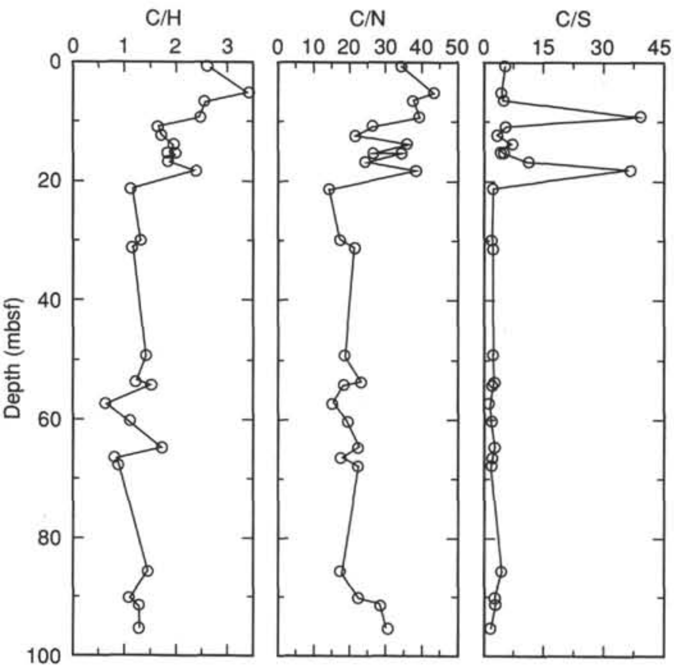

Figure 28. C/H, C/N, and C/S ratios vs. depth for Hole 855C.

cent of a xenocryst. In one sample (139-855A-8R-1, Piece 2, 21–23 cm) a large euhedral magnetite grain was found in an aggregate with a large pyroxene. Plagioclase is the only discernible groundmass phase in addition to a glassy mesostasis. Vesicles are small (0.5–0.8 mm) and uncommon (<3%).

Samples studied from Unit 2 include 139-855A-9R-1 (Piece 3, 23–26 cm), 139-855D-6R-1 (Piece 1, 8–10 cm), and 139-855D-5R-1 (Piece 8, 29–32 cm). Much of the phenocryst population included in the thin-section descriptions for Unit 2 is more appropriately considered microphenocrystalline in comparison with the large, well-formed crystals of Unit 1. All olivine was considered a phenocryst phase (as compared to groundmass) even where grain size was very small. The plagioclase microphenocrysts overlap groundmass phases in size and composition. Thus the thin-section descriptions suggest that there are more phyric rocks than can be discerned in megascopic examination. All three thin sections contain olivine and plagioclase phenocrysts. The olivine microphenocrysts vary in size from 0.05 to 1 mm and in abundance from 0% to 6%. Plagioclase phenocrysts and microphenocrysts can be up to 20% of the rock by volume, overlapping the population of smaller grained groundmass phases. More typical plagioclase phenocrysts are present in volume percentages of 0% to 5%. Some of the larger euhedral plagioclase phenocrysts exhibit distinctive concentric zonation (Fig. 40). The crystallinity of the groundmass is distinctive. Clinopyroxene forms spherulitic masses and bowtie structures with plagioclase. Granular magnetite dusts the grains. The magnetite is all less than 1 mm in size. The mesostasis is cryptocrystalline rather than hyaline.

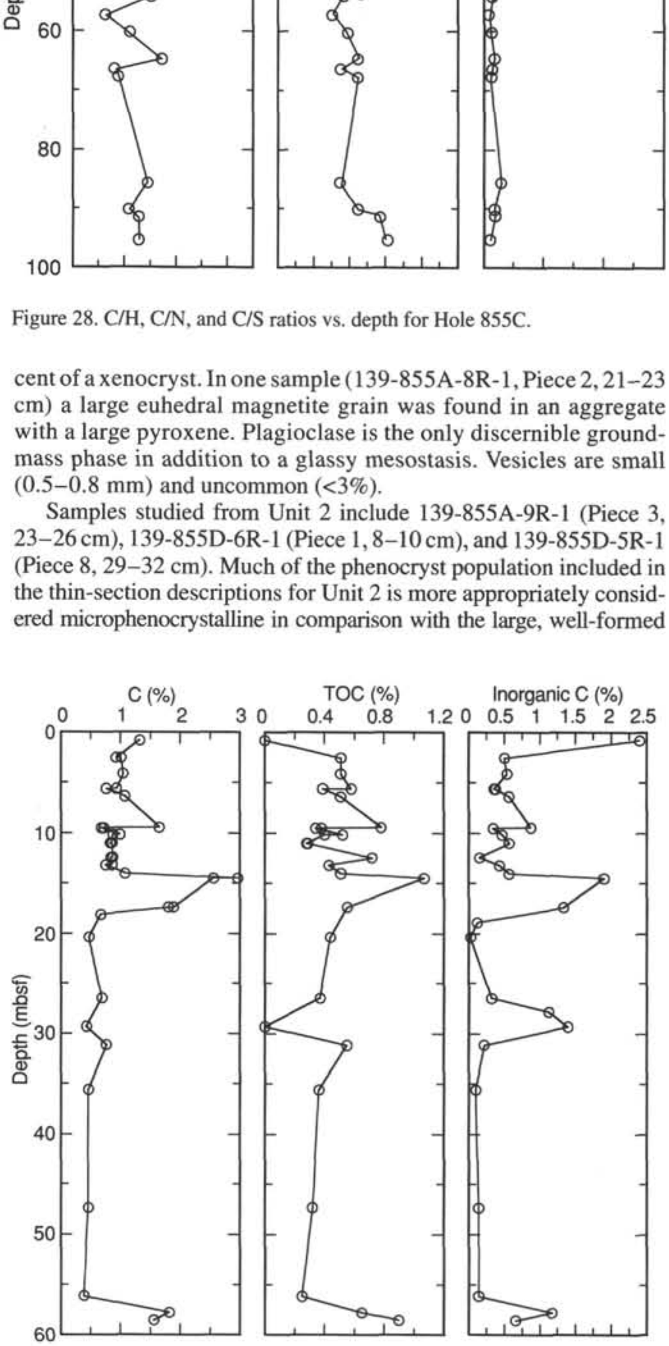

Figure 29. Total carbon, organic carbon (by difference), and inorganic carbon vs. depth for Hole 855A.

Alteration and Metamorphism

The samples from nearer the fault (Holes 855A and 855B) are notably fresh, with only trace amounts of secondary minerals observed in a few samples. Olivine is rarely altered, usually being replaced by a mixture of carbonate and saponite. More rarely, olivine is replaced by talc. Calcite, celadonite, and smectite are also common as vesicle fillings (Fig. 41). The samples farther to the west (Holes 855C and 855D) contain similarly limited quantities of smectite and carbonate. However, the individual pieces from Hole 855D are coated on several sides with a variety of greenschist to subgreenschist-grade minerals, including chlorite, quartz, epidote, and pyrite. These minerals are not visible in thin section. We presume that these coatings are the remnants of mineral-filled fractures that once enclosed these basaltic fragments. Most pieces from Hole 855D were observed to have a dark rind, presumably resulting from seafloor alteration or interaction with fluids percolating through the rocks.

Results of Geochemical Analyses

Data for four samples from Site 855 are presented in Tables 17 and 18. Major and trace elements (Table 17) were determined by X-ray fluorescence (XRF), and H_2O, CO_2, and sulfur by CHNS analyzer (see "Igneous Petrology and Geochemistry" section, "Explanatory Notes" chapter, this volume). CIPW normative calculations (Table 18) were done assuming that Fe^{2+} forms 90% of the total iron.

The samples are all fine-grained, variably porphyritic basalt. As shown petrographically, they have similar phenocryst compositions but variable phenocryst abundances. In spite of their variable phenocryst content, their chemical compositions vary only slightly. For example, silica varies only 1.44% (49.44%–50.88%). Alteration is minor, as noted petrographically, and is reflected in the low H_2O (0.39%–0.79%) and CO_2 (0.25%–0.40%) contents. The most intensely altered sample from petrographic observations (139-855A-9R-1, 26–28 cm) has the highest content of volatile elements. The contents of H_2O, CO_2, and S do not correlate with any of the major elements, indicating little or no exchange of major elements with seawater. The lack of major chemical exchange is reflected in the lack of corundum (Al_2O_3) in the norm (Table 18).

The analyzed samples are typical tholeiitic mid-ocean ridge basalt (MORB) (Fig. 42), but contain slightly higher Al_2O_3 contents for their specific MgO contents than typical basalt from the Juan de Fuca Ridge south of the Cobb propagator (Karsten et al., 1990). Their "immobile" minor and trace element compositions are clearly within the fields of ocean-floor basalts (Fig. 43). The major and minor element compositions of the Site 855 samples are indistinguishable from those of Endeavour Ridge segment basalts (Karsten et al., 1990; Fig. 44). The Endeavour segment of the Juan de Fuca Ridge is the unsedimented spreading center 20–40 km south of Site 855 (see Davis and Villinger,

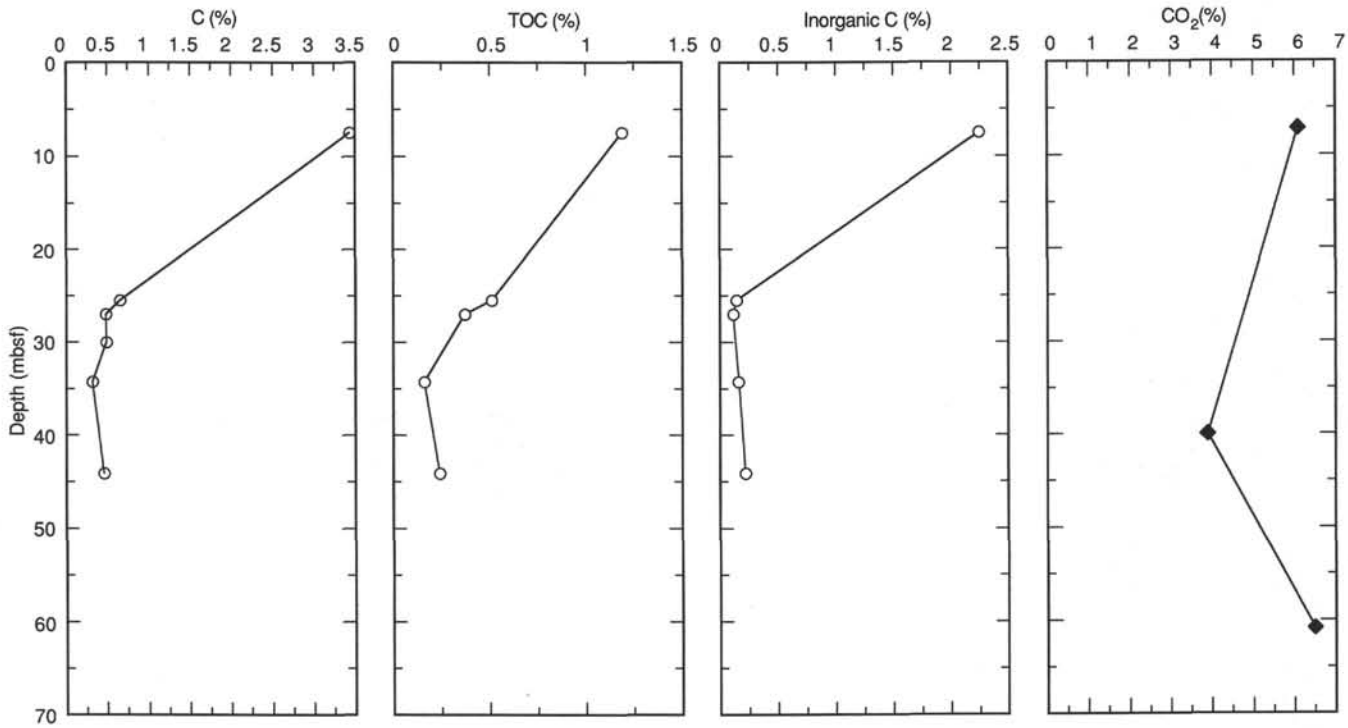

Figure 30. Total, inorganic, and organic carbon and free carbon dioxide vs. depth for Hole 855B.

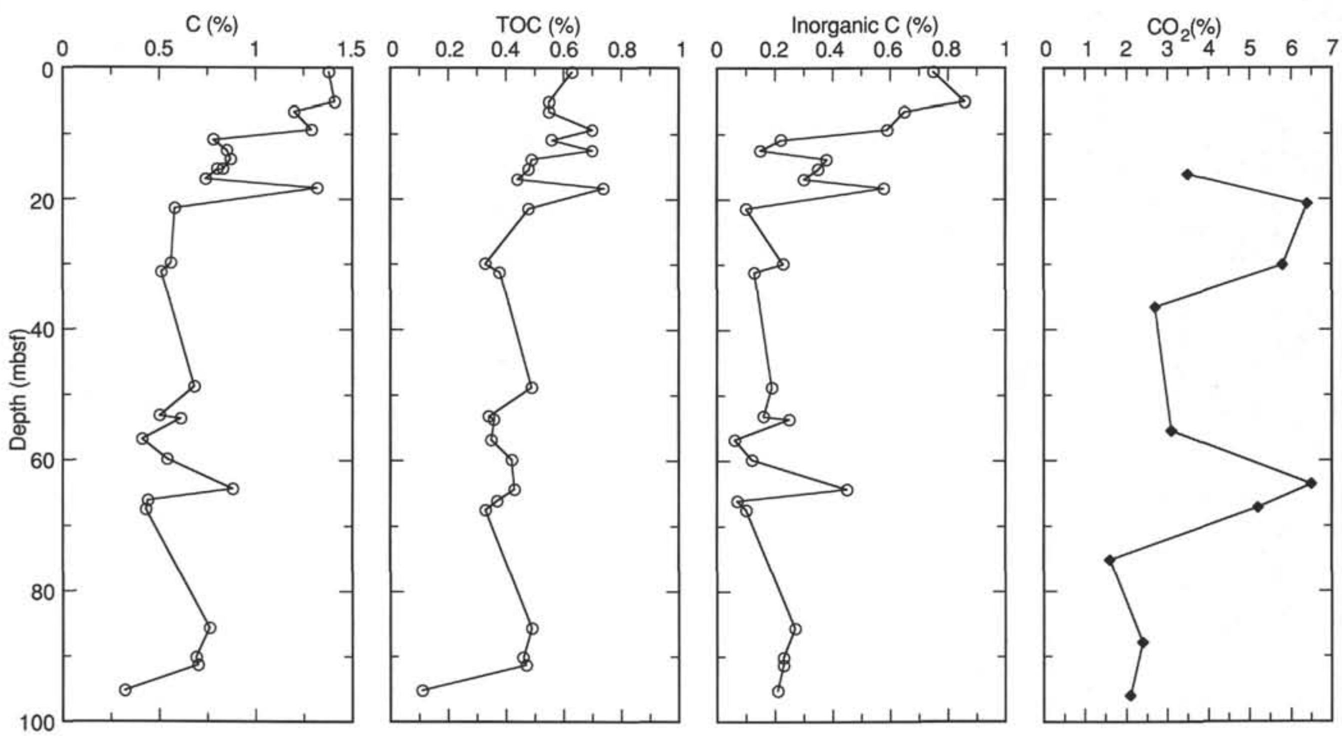

Figure 31. Total, inorganic, and organic carbon and free carbon dioxide vs. depth for Hole 855C.

this volume). The Site 855 samples lie compositionally almost at the centroid of the data presented by Karsten et al. (1990), but are slightly less evolved (higher Mg number) than about two-thirds of the Endeavour samples.

The sample from Unit 1 (139-855A-8R-1, 26–28 cm) has higher TiO_2, Zr, and P_2O_5, and a slightly lower Mg number than Unit 2. Unit 1 is therefore more evolved than Unit 2. Unit 1 samples also have higher Ni, Cr, and Al_2O_3 contents, reflecting their higher content of plagioclase phenocrysts, and possibly a higher content of olivine.

The variation in composition among the samples can be explained by fractional crystallization of olivine, clinopyroxene, and plagioclase, as illustrated by the linear variation in Ti vs. Zr (Fig. 42) and

Table 12. X-ray diffraction mineralogy for bulk samples from Holes 855A, 855B, and 855C.

Core, section, interval (cm)	Quartz	Feldspar	Hornblende	Chlorite	Mica	Calcite
139-855A-						
1R-4, 111–114	***	***	*	*	*	*
2R-3, 42–44	***	*	*	******	******	
3R-2, 80–82	***	***	*	*	*	
4R-3, 31–33	***	***	*	*	*	******
5R-1, 100–103	***	***	*	*	*	
6R-2, 34–37	***	***	*	*	*	
7R-2, 113–116	*	***	*	*		******
139-855B-						
2R-2, 30–36	*	*	*	*	*	******
4R-4, 99–102	***	******	***	*	*	
5R-1, 25–29	***	***	*	*	*	*
7R-2, 113–116	*	*	*	*	*	******
139-855C-						
3R-2, 80–82	***	***	*	*	*	
4R-3, 110–112	***	***	*	*	*	
6R-5, 76–80	***	******	*	*	*	
7R-1, 76–80	***	******	*	*	*	
8R-2, 33–36	***	******	*	*	*	
10-R, 43–47	***	***	*	*	*	
11-R, 67–70	***	******	*	*		

Notes: Relative mineral abundances were determined by peak heights and are indicated as follows: tr = *, *** = minor, ****** = major, and ******** = dominant. Because peak heights are determined by mineral morphology in addition to mineral abundance, this table cannot be used to quantitatively determine the relative abundances of different minerals. (See "Sediment Geochemistry and Alteration" section, "Explanatory Notes" chapter, for a description of X-ray diffraction methods.)

TiO_2 vs. Mg number (Fig. 45). In Figure 44, three of the samples form a near-vertical line, indicating that their compositional differences are primarily related to fractionation of plagioclase. The fourth sample (from Section 139-855A-8R-1), however, sits apart from the others and is the product of fractionation of Mg-rich minerals, probably olivine and lesser clinopyroxene.

In summary, the Site 855 samples are typical of lavas from the Endeavour segment area. They are moderately evolved and have undergone fractionation of plagioclase and olivine, with lesser clinopyroxene fractionation. They are only slightly altered and bear no information regarding proximity to the hydrothermal centers located about 4 km to the west.

The glomerocrysts and xenocrysts that are typical of Unit 1 basalt are likely artifacts of crystal fractionation that occurred somewhere in the crust before the eruption of these young, evolved magmas. This is in contrast to the microphenocrysts and quench crystals that grew *in situ,* in equilibrium with the glassy matrix. The ovoid, broken, and partially resorbed crystal shapes, as well as the sodic rims on the large plagioclase crystals, are evidence of such disequilibrium.

Conclusions

Drilling at Site 855 recovered a variety of fresh to slightly altered basaltic rocks. The youngest (freshest) basalts of Unit 1 are highly porphyritic to glomeroporphyritic. The glomerocrysts, large grain sizes, and occasional xenocrysts suggest that these lava flows came from magma bodies that had substantially crystallized. The evolved magma composition is reflected in the low Mg number and high FeO and TiO_2 contents. The increasing groundmass crystallinity of Units 2 and 3, and the decrease in phenocryst abundance and size, could

Table 13. Major element geochemistry (in wt%) for sediment samples from Holes 855A, 855B, and 855C.

Core, section, interval (cm)	Depth (mbsf)	Lithology	SiO_2	TiO_2	Al_2O_3	Fe_2O_3	MnO	MgO	CaO	Na_2O	K_2O	P_2O_5	LOI	Total	H_2O	CO_2
139-855A-																
1R-4, 111–114	5.61	Clay	56.13	0.85	16.43	8.11	0.14	3.89	5.00	2.27	2.22	0.20	4.75	98.48	5.04	1.32
2R-3, 42–44	11.02	Silt	61.24	0.78	15.80	5.92	0.10	2.88	4.32	1.76	2.57	0.18	4.46	97.83	3.42	2.09
3R-2, 80–82	18.90	Clay	56.86	0.91	17.08	8.58	0.12	4.61	3.04	2.04	2.20	0.19	4.36	99.90	5.31	0.44
139-855B-																
4R-4, 99–102	29.99	Clay	62.17	0.84	15.24	6.35	0.11	3.08	4.08	2.76	1.68	0.22	3.48	98.56	3.51	0.66
5R-1, 25–28	34.25	Silt	62.98	0.82	15.04	5.99	0.10	2.76	4.66	3.04	1.53	0.19	2.90	98.29	2.07	0.59
139-855C-																
6R-5, 76–80	53.26	Clay	58.98	0.89	16.57	7.63	0.13	3.81	3.80	2.42	1.97	0.20	3.62	98.52	3.69	0.59
7R-1, 76–80	56.86	Clay	53.96	0.90	15.98	11.85	0.13	4.57	2.81	2.07	2.07	0.18	5.49	96.87	5.67	0.22
8R-2, 33–36	66.78	Clay	60.03	0.91	16.60	7.24	0.13	3.73	3.82	2.55	1.90	0.20	2.90	98.37	4.32	0.37
10R-5, 43–47	89.83	Clay	55.33	0.95	17.37	8.50	0.11	4.70	3.33	2.22	2.26	0.22	5.00	98.66	4.95	0.84
11R-1, 67–70	95.27	Silt	64.03	0.82	14.75	5.78	0.09	2.76	4.70	3.16	1.38	0.18	2.35	98.63	2.25	0.77

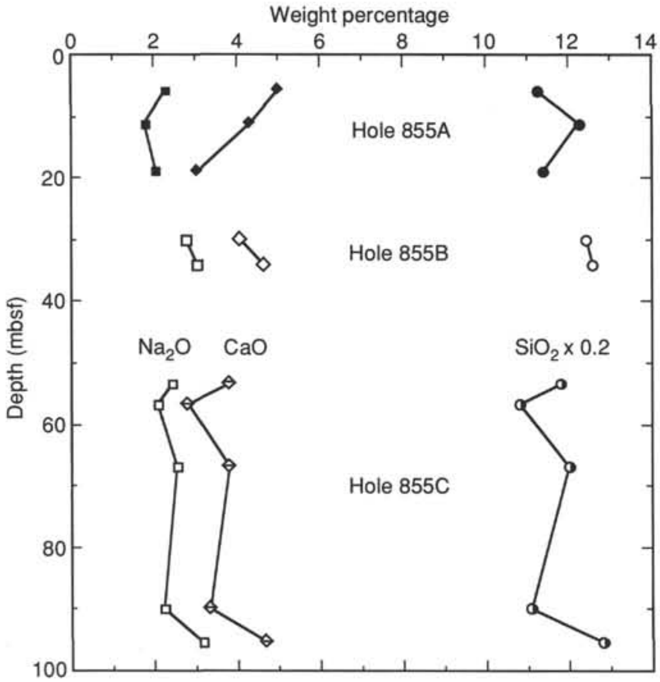

Figure 32. Na_2O (squares), CaO (diamonds), and $SiO_2 \times 0.2$ (circles) vs. depth for Holes 855A, 855B, and 855C. The covariation in these elements is interpreted to represent the abundance of plagioclase feldspar and quartz, which are more abundant in the coarser grained fraction of turbiditic sediment.

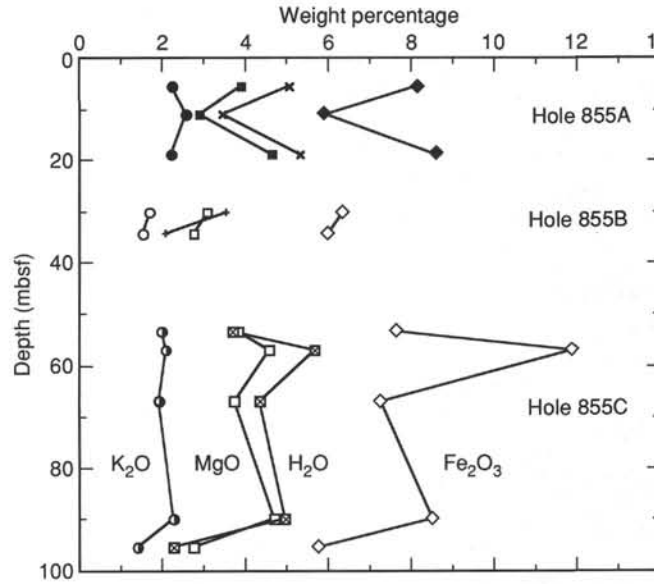

Figure 33. K_2O (circles), MgO (squares), H_2O (crosses, pluses, and squares with crosses), and Fe_2O_3 (diamonds) vs. depth for Holes 855A, 855B, and 855C. The covariation in these elements is interpreted to represent the abundance of illite and chlorite, which are more abundant in the finer grained portion of turbiditic sediment and in hemipelagic clay deposited between turbidites.

indicate that these samples come from a more interior portion of a large flow or from an earlier phase of a magmatic cycle. The well-defined quench margins, abundance of fresh glass, and characteristic spherulitic texture observed in many samples is suggestive of well-formed pillow basalts. The chemical composition of the basalt from this site is similar to that of igneous rock of the Endeavour Ridge segment, as characterized by dredges and submersible samples (Karsten et al., 1990; D. Stakes, unpubl. data, 1992). We conclude that the basalt from Site 855 was erupted at different stages of a magmatic cycle, and is typical of medium to slow spreading ridge axes. All of the samples can be correlated by fractional crystallization of olivine, clinopyroxene, and plagioclase.

Except for trace quantities of low-temperature vesicle fillings, the lack of alteration minerals does not contradict the model of recharge along the fault. Because of their small number and size, however, these samples cannot provide definitive evidence for or against this process. The samples from Hole 855D are of interest because of their conspicuous coatings of subgreenschist- to greenschist-grade minerals and more highly altered chemical compositions. The secondary minerals probably precipitated from warm to hot hydrothermal fluids that percolated through these basement samples. Additional

Table 13 (continued).

Core, section, interval (cm)	TOC	S	N
139-855A-			
1R-4, 111–114	0.49	0.14	0.060
2R-3, 42–44	0.28	0.00	0.062
3R-2, 80–82	0.46	0.18	0.046
139-855B-			
4R-4, 99–102	0.31	0.32	0.074
5R-1, 25–28	0.16	0.19	0.041
139-855C-			
6R-5, 76–80	0.34	0.20	0.057
7R-1, 76–80	0.35	0.28	0.075
8R-2, 33–36	0.33	0.22	0.053
10R-5, 43–47	0.47	0.24	0.066
11R-1, 67–70	0.11	0.18	0.026

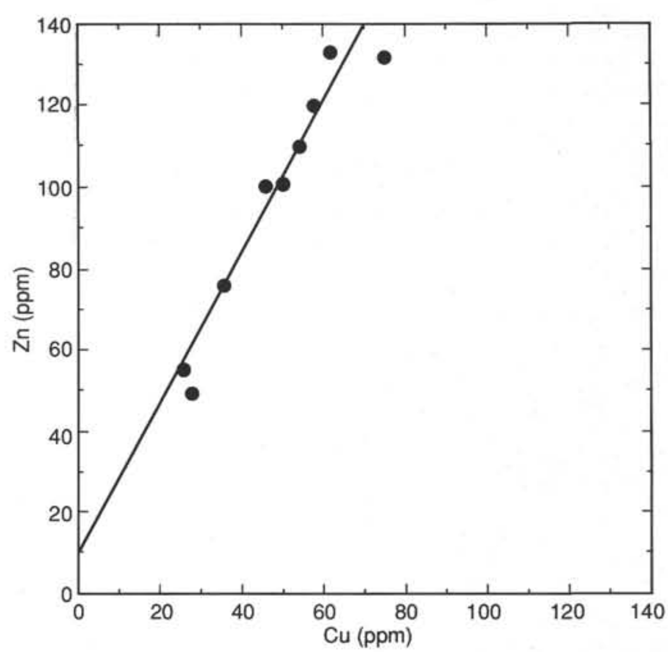

Figure 34. Zn vs. Cu for sediment samples from Holes 855A, 855B, and 855C. The linear regression line fitted to the data has a slope of 1.8 and a Y intercept of 10.5 ($r^2 = 0.905$).

Table 14. Minor element geochemistry (in ppm) for sediment samples from Holes 855A, 855B, and 855C.

Core, section, interval (cm)	Depth (mbsf)	Lithology	Ba	Ce	Cr	Cu	Nb	Ni	Rb	Sr	V	Y	Zn	Zr
139-855A-														
1R-4, 111–114	5.61	Clay	784	5	81	58	9	48	69	343	171	21	120	144
2R-3, 42–44	11.02	Silt	847	51	105	44	17	53	157	222	128	21	105	141
3R-2, 80–82	18.90	Clay	746	9	103	62	9	69	67	272	183	23	133	144
139-855B-														
4R-4, 99–102	29.99	Clay	568	8	95	36	10	48	50	354	147	22	76	201
5R-1, 25–28	34.25	Silt	507	12	78	26	9	36	38	386	146	23	55	217
139-855C-														
6R-5, 76–80	53.26	Clay	616	2	86	50	9	48	57	317	157	22	101	161
7R-1, 76–80	56.86	Clay	793	4	105	75	9	55	69	236	194	24	132	141
8R-2, 33–36	66.78	Clay	593	5	87	46	9	42	57	327	168	23	100	169
10R-5, 43–47	89.83	Clay	524	3	87	54	9	45	63	246	199	24	110	142
11R-1, 67–70	95.25	Silt	456	7	76	28	7	28	34	347	145	22	49	199

drilling is required to determine the relationship (if any) of these metamorphic minerals to the adjacent fault.

PHYSICAL PROPERTIES

Because the RCB was used in coring operations at all four holes, split sediment sections exhibited minor to severe drilling disturbance. The severity of the disturbance depended on the type of sediment recovered. Holes 855A and 855C were sampled in detail for physical properties (see Figs. 46 and 47); only a few measurements were made on samples from Hole 855B and none from Hole 855D because of low core recovery (see Fig. 48). The following discussion will focus on results from Holes 855A and 855C; results from Hole 855B are shown for completeness. Because of the anticipated core disturbance, only volume magnetic susceptibility was measured on all unsplit sections on the multisensor track in the hope that these measurements could be used for correlating parts of the section from hole to hole. Closely spaced physical properties measurements were made on discrete samples, taken at a typical frequency of two samples per section. All volume magnetic susceptibility data, given in SI, are not corrected for the core-to-coil diameter ratio of 0.825. Also no corrections have been applied to compensate for partially filled liners. None of the physical properties data shown are corrected for *in-situ* temperature, *in-situ* pressure, or rebound effects.

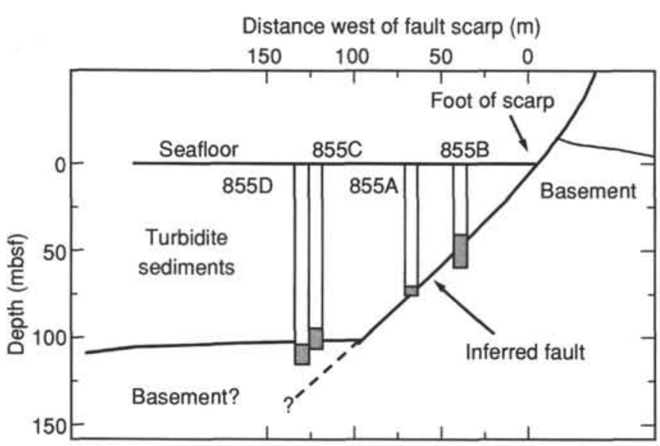

Figure 35. Regional distribution of core locations with respect to the fault scarp at Site 855. Shaded portion of each hole is the interval at which the drill penetrated basalt. Based on observations of unsedimented ridges, the fault may be a series of short offset steps. We have indicated the simplest of many possible profiles. Rock was recovered from all four holes, but recovery everywhere was less than 20%.

Volume Magnetic Susceptibility Measurements

The high volume magnetic susceptibility of about 0.001 to 0.002 measured on all cores from Holes 855A, 855B, and 855C is characteristic of hemipelagic and turbidite sediments with a large terrigenous component (Telford et al., 1976). The main source of the volume magnetic susceptibility signal is the high magnetite content of the sediments. A correlation of volumetric magnetite content with measured volume susceptibility is planned as a post-cruise study. The volume magnetic susceptibility variations with depth for Holes 855A, 855B, and 855C are shown in Figures 49A–C. The profiles from Holes 855A and 855C do not show distinct features that would permit hole-to-hole correlation. Superimposed on the slowly varying base level of volume magnetic susceptibility, which is most likely related to changes in sediment source area, are highly variable and frequent changes in volume magnetic susceptibility that correspond to turbidite units (see "Lithostratigraphy and Sedimentology" section, this chapter). The thicknesses of these turbidites, which are interbedded with hemipelagic sediments, ranges from 0.1 to 0.5 m. The volume

Table 15. Summary of basalt recovery and basement penetration.

Hole, core, section	Distance to base of scarp (m)	Basement intercept (mbsf)	Penetration to core bottom (mbsf)	Recovery (%)	Number of basalt pieces
139-855A-	70	74			
8R-1			74.8	3.5	5
9R-1			76.8	15.5	6
139-855B-	40	45			
8R-CC			63.3	n.a.	6
139-855C-	125	98			
12R-CC			106.9	n.a.	1
139-855D-	125	108			
5R-1			113.9	4.5	8
6R-1			118.6	10.7	8

Note: n.a. = not applicable.

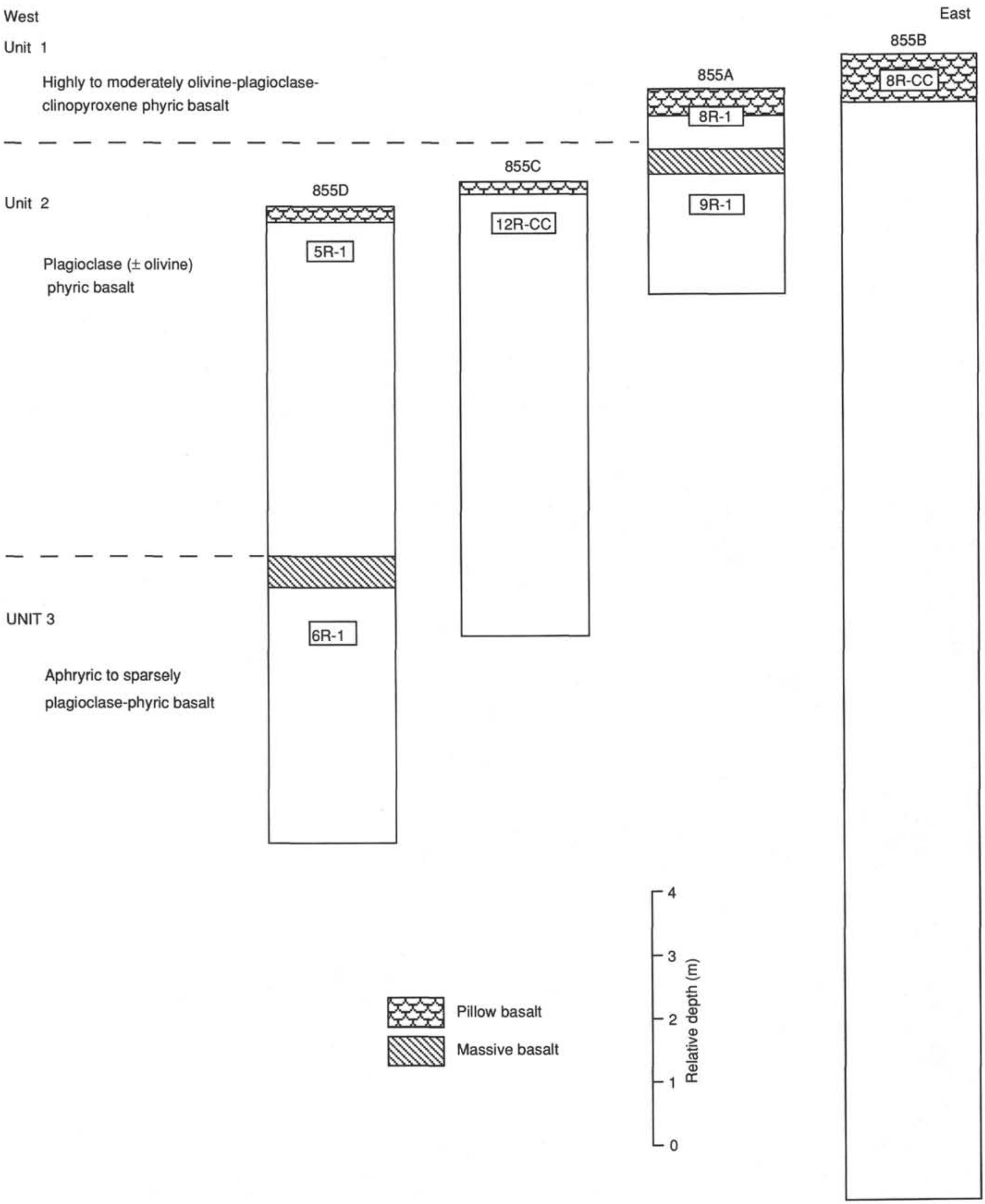

Figure 36. Basalt lithostratigraphy of Site 855. Column length is total core penetration into basement while patterned areas indicate recovery. Unit designations are based on phenocryst proportion, which is more ambiguous in massive, more crystalline units. Samples from core-catcher sections (CC) are pieces from the bottom of the core; there is no stratigraphic control among the pieces.

Table 16. Approximate modal compositions of some representative basalts from Site 855.

Sample 139-	855A-8R-1 18–20 cm Piece 1	855A-9R-1 24–26 cm Piece 3	855B-8R-CC 17–19 cm Piece 4	855D-5R-1 29–32 cm Piece 8
Primary minerals (%)				
Olivine	10	2	3	3
Plagioclase	27	48	55	45
Clinopyroxene	5	26		40
Titanomagnetite				3
[a]Mesostasis	57	20	42	9
Secondary minerals (%)				
Celadonite	1			
Smectite clays		3		
Carbonate		1		
Talc		trace		

[a]Interstitial or matrix glass. In Sample 139-855D-5R-1, 28–32 cm, the pyroxene is composed of crystallites and could also be considered mesostasis. All of the olivine, and some of the plagioclase and clinopyroxene, occur as phenocrysts.

magnetic susceptibility at the base of the turbidites is up to three times higher than the background level of volume magnetic susceptibility. The basalt recovered at the bottom of Holes 855A and 855C has a volume magnetic susceptibility of about one order of magnitude higher than the sediments, in the range of about 0.01 to 0.02.

Figure 50A shows a depth interval within Hole 855C that displays an exceptional change in volume magnetic susceptibility. A depth interval with low variability overlies an interval (55.5–67.1 mbsf) in which the volume magnetic susceptibility is up to twice as high within the base of turbidites as in the overlying section. The frequency of turbidites per recovered meter of core is substantially higher in the underlying interval. This change in character may reflect a dramatic change in the sedimentation source area over time. The deepest recovered part does not necessarily represent the end of this interval of frequent turbidites, and thus an estimate of the thickness of this sequence is not possible. The interval of increased turbidite occurrence in Hole 855C (55.5–67.1 mbsf) may correlate with an interval in Hole 855A (45.5–57.8 mbsf) that has been recovered only partially (Cores 139-855A-6R and -7R, see Fig. 50B). Both depth intervals show a similar signature of frequent and small turbidites. Unfortunately there is no sedimentological or stratigraphic infor-

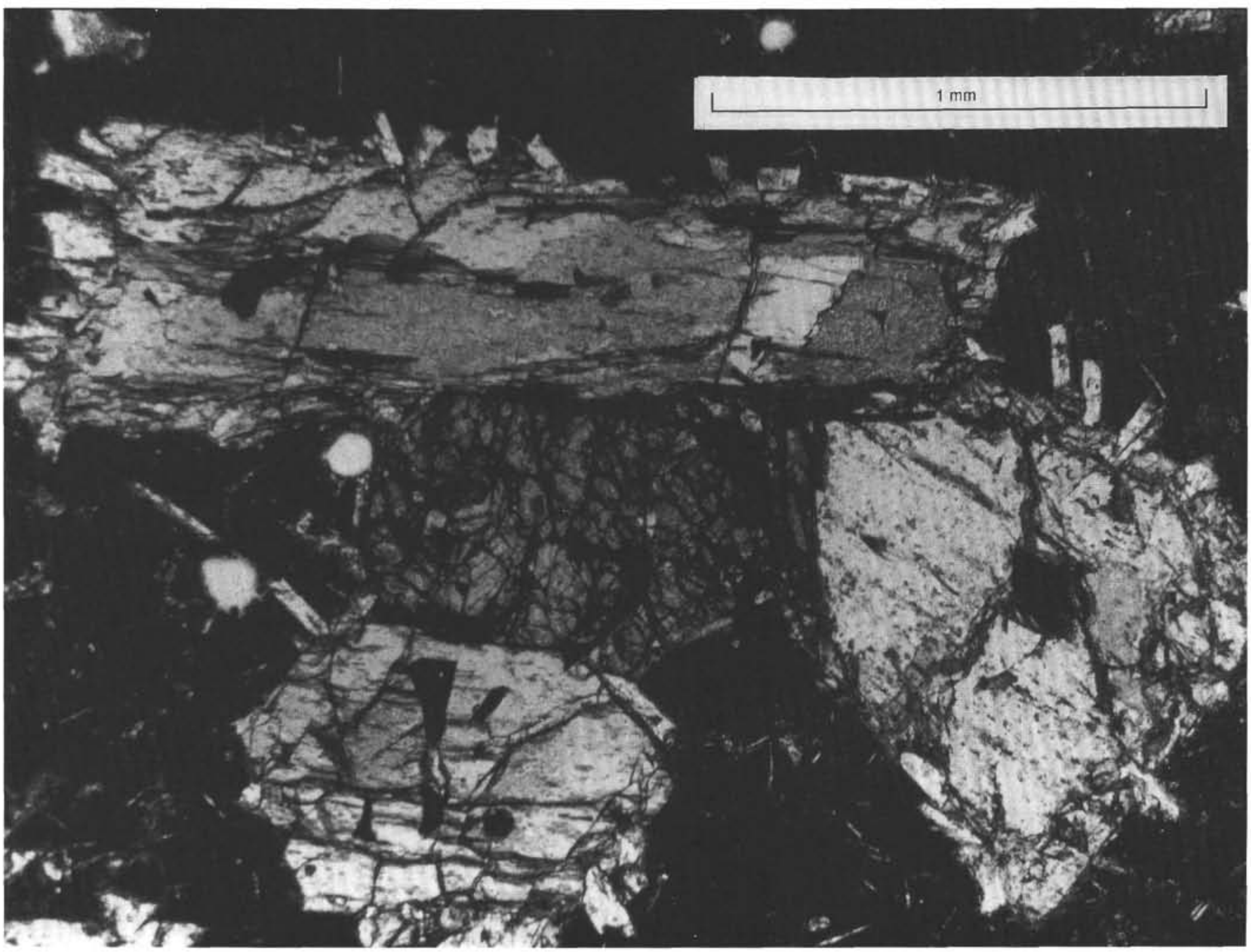

Figure 37. Sample 139-855A-8R-1, 21–23 cm (Piece 2). Large euhedral phenocrysts of olivine and clinopyroxene with smaller plagioclase in fresh, black glassy matrix. Transmitted light, 5×.

Figure 38. Sample 139-855A-8R-1, 18–20 cm (Piece 1). Large oikocryst of clinopyroxene with included grains of twinned plagioclase. Transmitted polarized light, 10×.

mation to support this correlation (see "Lithostratigraphy and Sedimentology" section, this chapter).

Index and Other Physical Properties

Index property samples were taken either directly at or close to the depths where thermal conductivity and acoustic measurements were made. An overview of the results can be found in Table 19. Figures 46 to 47 show the variation of all measured physical properties (except volume magnetic susceptibility) as a function of depth. All physical property measurements are listed in Tables 20 to 28.

In Hole 855A the wet-bulk density is locally variable throughout the hole, with values ranging from 1.51 to 1.93 g/cm^3. This variability is reflected in porosity and water content values. No systematic variation with depth is present on a large scale. The grain density is remarkably uniform and has a value of 2.78 ± 0.04 g/cm^3, which is slightly higher than expected for hemipelagic sediments (Hamilton, 1976). The thermal conductivity in general reflects the variations in porosity and water content, with large variations present locally and little variation with depth in the hole.

Results from Hole 855C are similar to those from Hole 855A (Table 19), although in the former there is a small decrease in porosity and water content with depth. This decrease becomes more pronounced below 80 mbsf as the sediments become more indurated. The induration affects the thermal conductivity as well as the compressional wave velocity. The compressional wave velocity in both holes is in the range of 1500 to 1600 m/s and increases to about 1700 m/s as the sediments become more indurated below a depth of 80 mbsf in Hole 855C.

There are a number of pronounced local variations in the physical properties of sediments in Hole 855A (Figs. 46 to 47) to a depth of about 75 mbsf. In most cases coherent changes are seen in all measured physical properties, which points to a real sedimentological cause for these signals. However, the signals observed could also be caused entirely by the coring process, as they are also correlative with individual core boundaries. A final answer to this question will be possible only after the completion of post-cruise grain-size and compositional analyses that are planned for index property residues.

The average thermal conductivity, porosity, and grain density in Holes 855A and 855C are virtually identical. This allows us to estimate the grain thermal conductivity from the porosity for both holes. Assuming a thermal conductivity of seawater of 0.6 W/(m·K) and using the average values of porosity and thermal conductivity from Holes 855A and 855C (see Table 19), the resulting computed geometric mean grain thermal conductivity is 3.4 W/(m·K). This fairly high thermal conductivity of the grains can be explained by a volume ratio of 39% quartz to about 61% clay in the sedimentary matrix, using a thermal conductivity of 7.7 W/(m·K) for quartz and

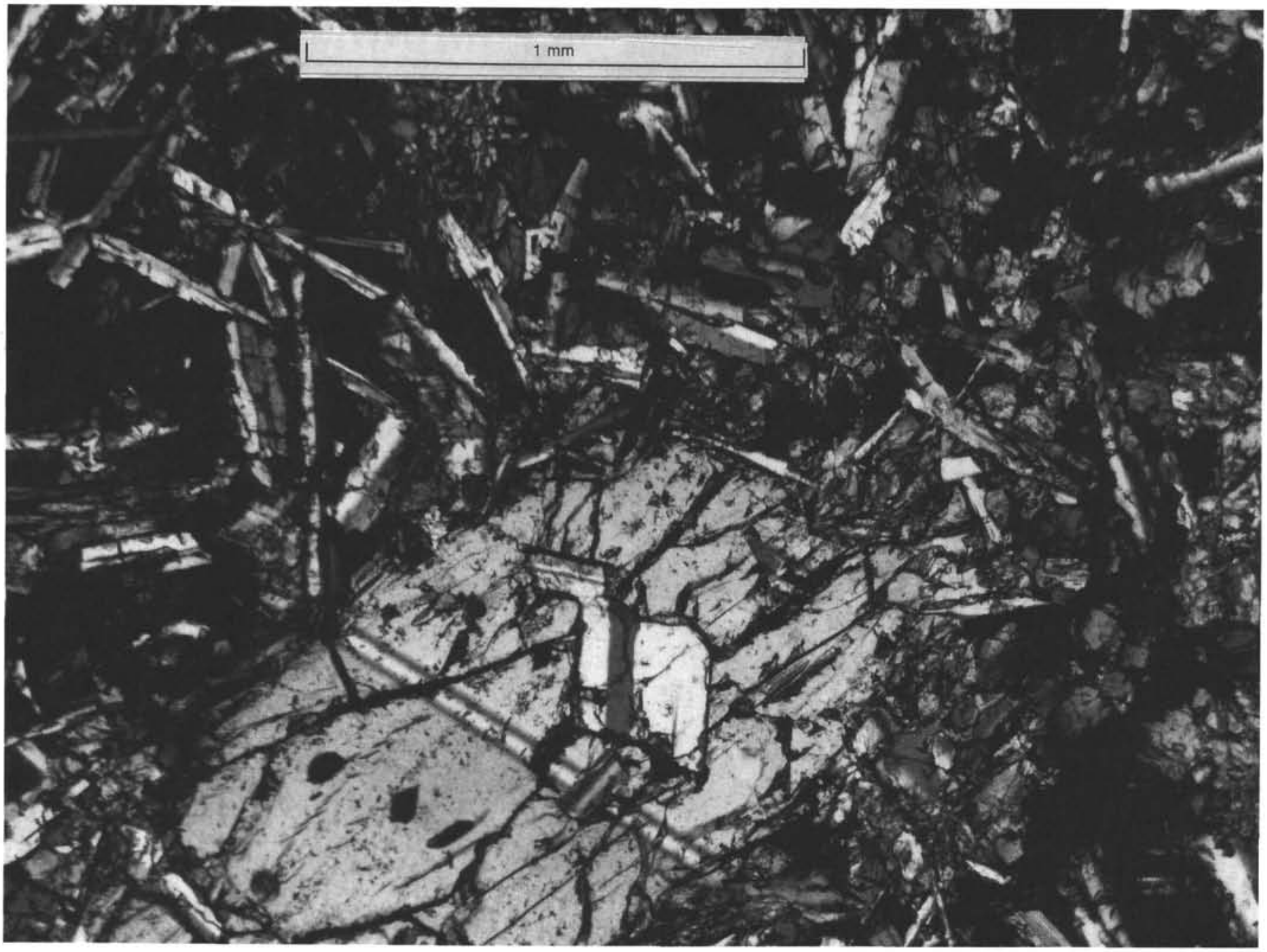

Figure 39. Sample 139-855A-9R-1, 24–26 cm (Piece 3). Ovoid, twinned clinopyroxene grain with an included grain of twinned plagioclase inferred to be a xenocryst. Note spherulitic texture and fresh glass in surrounding groundmass. Plane transmitted light, 5×.

2.0 W/(m·K) for clay (Brigaud and Vasseur, 1989). A similar volume ratio of quartz to clay is observed in smear slides (see Section 4, this volume). The surprisingly high value for the grain thermal conductivity is supported by the relationship between porosity and thermal conductivity, as shown in Figure 51 for the upper 40 m of Hole 855A. This depth interval was chosen because it has large changes in porosity that correlate well visually with the measured thermal conductivity. The dashed lines in Figure 51 represent calculated thermal conductivities as a function of porosity for grain thermal conductivities of 2.5 and 5.0 W/(m·K). The solid line is obtained by a least-squares fit of thermal conductivity to porosity, assuming a geometric mean model with the grain thermal conductivity as the parameter to be fitted. The resulting best-fit grain conductivity is 3.6 W/(m·K). This value agrees well with the estimated grain thermal conductivity obtained from average values of porosity and thermal conductivity.

HEAT FLOW

Operations

The WSTP was deployed six times at Site 855 (Table 29). All temperature records from the data loggers display occasional electronic noise (isolated spikes) of unknown origin, but the records are otherwise clear. Each station which resulted in a consistent temperature-time curve following probe penetration was processed by fitting the measured temperatures to modeled temperatures, as described in the "*In-situ* Temperatures" section, "Explanatory Notes" chapter (this volume). The data were hand-filtered before processing to remove recorder noise.

The tool was first deployed following collection of Core 139-855A-4R at 36.6 mbsf, but returned no data because the battery was miswired. No attempt was made to measure temperatures in Hole 855B because we expected to encounter basement at an extremely shallow depth and did not wish to risk damaging the tool.

The tool was run next following recovery of Core 139-855C-4R at 37.7 mbsf, and it produced a good record (Fig. 52). After penetration, recorded temperatures follow a typical cooling curve for the first part of the station, but temperatures rise toward the end (Fig. 52A). This result suggests that either (1) the probe was in material that was somewhat cooler than the surrounding rock (fill) but was warming with time, or (2) the probe continued to sink into the sediments during the station. If the probe was in fill, then the estimated temperature resulting from this run is a lower boundary to the *in-situ* temperature. Extrapolation of the first part of the cooling curve to infinite time yields a temperature of 7.9°C, with an estimated error of ±0.3°C.

Three more runs were completed in Hole 855C, following collection of Cores 139-855C-6R, -8R, and -10R, at depths of 57.2, 76.3, and 95.7 mbsf, respectively. The deployment following Core 139-855C-6R yielded a record typical of a warm formation (Fig. 53).

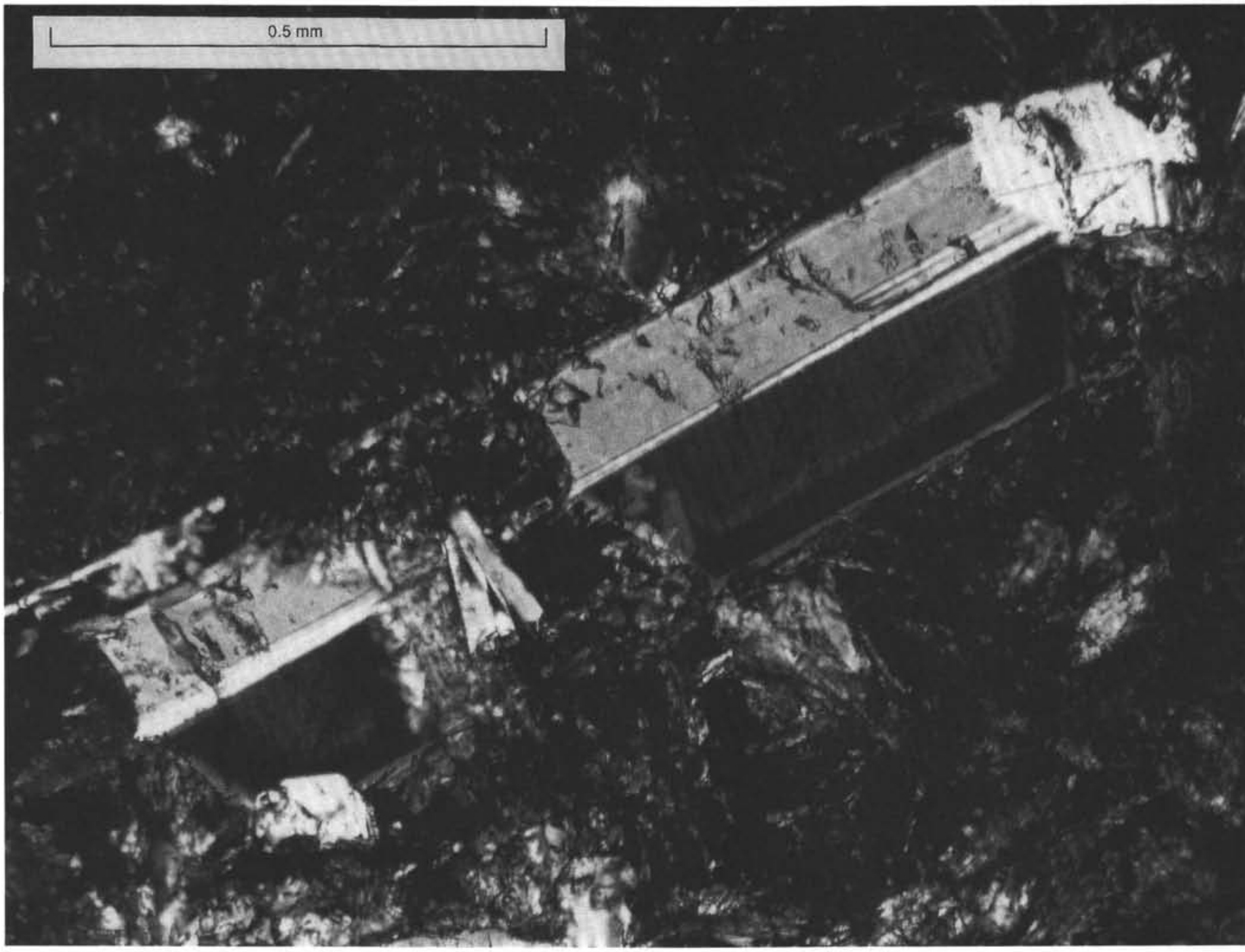

Figure 40. Sample 139-855D-5R-1, 29–32 cm (Piece 8). Large plagioclase phenocryst with concentric zonation. Note thin white sodic rim on crystals. Transmitted polarized light, 10×.

Measured temperatures rise rapidly at first and then level off, in this case to an extrapolated temperature of 20.4 ± 0.2°C. The temperature record from the deployment after Core 139-855C-8R indicates that the probe was still heating rapidly when the tool was pulled from the mud; the extrapolated temperature of 26.9°C is a lower bound (Fig. 54). An upper limit on this temperature is difficult to estimate, but it is probably not more than about 28°C. The deployment following Core 139-855C-10R resulted in a record which suggests a poor contact between the probe and the formation (Fig. 55). Measured temperatures rise smoothly at first, then fall off rapidly with time. A minimum *in-situ* temperature for this depth, estimated from extrapolation of the first part of the curve, is about 26.1°C. One additional deployment following collection of Core 139-855D-1W at 80.6 mbsf probably penetrated fill at the bottom of the hole, as measured temperatures were extremely low and the tool heated continuously during the station (Fig. 56).

Interpretation

A plot of all estimated temperatures from Site 855 reveals a probable thermal gradient of 0.328°C/m through the upper 76.3 mbsf (Fig. 57). This gradient was calculated as a least-squares, linear best-fit of the estimated temperature following Core 139-855C-6R, the lower boundary for the measurement following Core 139-855C-8R, and the bottom-water temperature of 1.8°C (Davis and Villinger, this volume). We interpret the measurement following Core 139-855C-4R to have been in fill (although it apparently resulted in the collection of a usable water sample; "Fluid Geochemistry" section, this chapter) and the deployment following Core 139-855C-10R to have cracked the formation, allowing water to cool the probe. Assuming a gradient of 0.328°C/m and average thermal conductivity of 1.2 W/(m·K) (see "Physical Properties" section, this chapter) the calculated conductive heat flow is about 394 mW/m^2. This value is low relative to seafloor measurements made near Site 855 (Davis and Villinger, this volume) but farther from the fault scarp. The influence of cold seawater being drawn into the basaltic layer underlying the sediment may be responsible for this low value. There is no thermal evidence for fluid flow through the sediment column at Site 855, although the data are admittedly inconclusive. These interpretations are consistent with those from the results of geochemical studies of pore fluids recovered at this site ("Fluid Geochemistry" section, this chapter.)

SUMMARY AND CONCLUSIONS

Of the four sites drilled in Middle Valley on Leg 139, Site 855 is the easternmost and farthest from the axis of the Juan de Fuca Ridge. It is therefore situated on the oldest crust, which may be as old as 400,000 yr (Davis and Villinger, this volume). The drilling target at

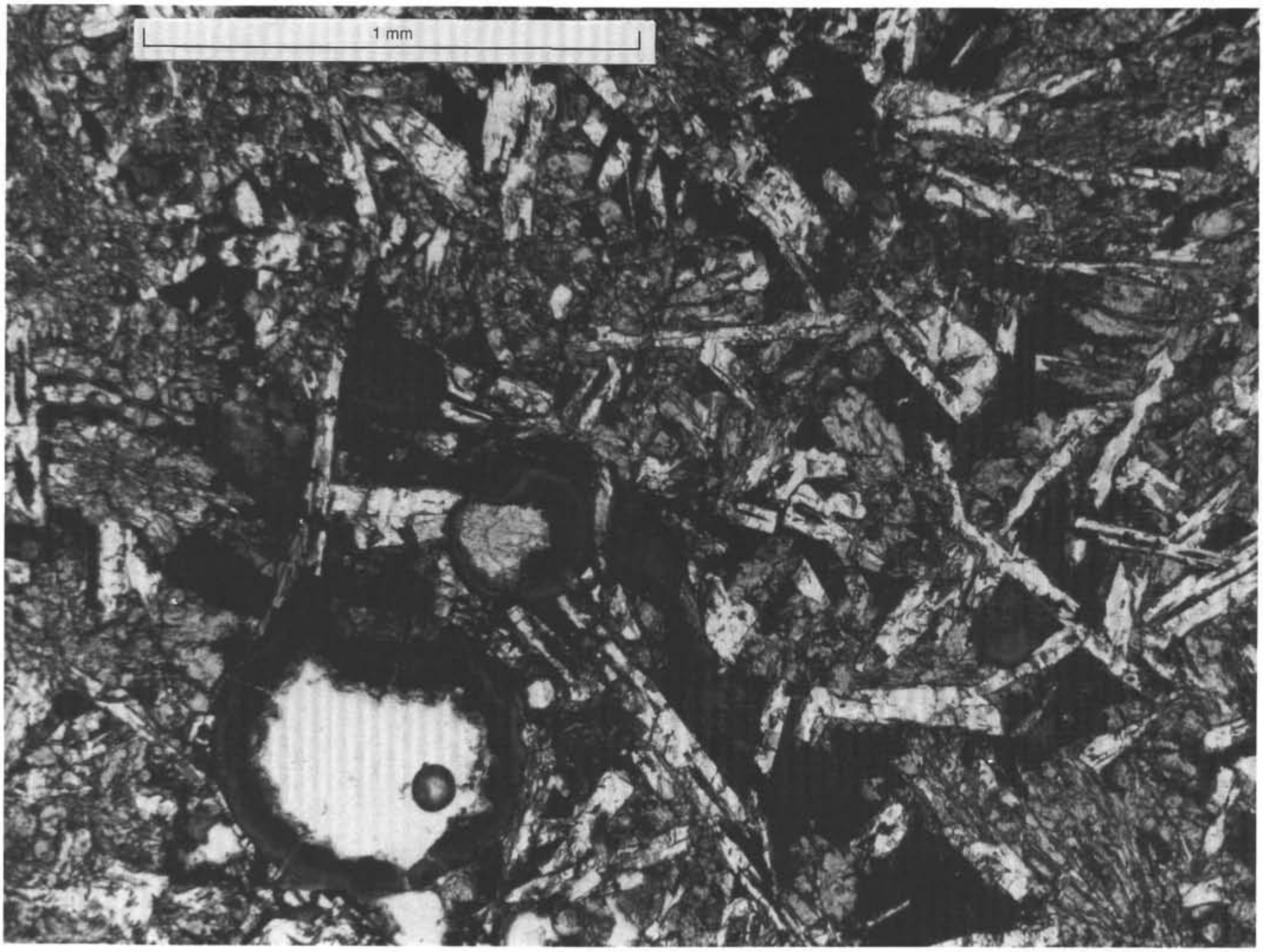

Figure 41. Sample 139-855A-9R-1, 24–26 cm (Piece 3). Round vesicle lined with brown smectite and filled with carbonate. Note fresh glass in surrounding groundmass. Plane transmitted light, 5×.

Site 855 was the fault scarp that, at this latitude, forms the topographic boundary of the valley. The objectives of drilling were to define the cross-sectional geometry and hydrologic nature of this rift-bounding fault, and to determine the nature and rate of fluid flow along the fault or through basement. Low heat flow at Site 855 (Davis and Villinger, this volume) suggests that seawater may be drawn into basement either along the fault or through the thin sediment section.

The four holes at Site 855 were drilled into the hanging wall of the fault. They were sited 40 m (Hole 855B), 70 m (Hole 855A), and 125 m (Holes 855C and 855D) west of the base of the fault scarp. All four holes bottomed in basalt, two inferred to be in the foot wall (855A and 855B) and two in the hanging wall (855C and 855D) (see Fig. 35). The depths at which basalt was encountered in Holes 855A (74 mbsf) and 855B (45 mbsf) indicate that the fault has an apparent dip of approximately 45°. Whether this is the true dip, or the average dip of a zone of en-echelon stair-step faults, cannot be ascertained. In either case it is consistent with the dip inferred from acoustic mapping and from the seismic reflection profiles, which also suggest that the full relief on the fault has been produced since the accumulation of the full section of sediment. The depths at which basalt was encountered in Holes 855C (98 mbsf) and 855D (108 mbsf), compared with the height of the scarp (115 m), indicate that basalt of the foot-wall block probably outcrops at the base of the scarp.

Basalt recovered from the four holes at Site 855, from depths up to 18 m into basement, is typical MORB that is similar in composition to basalt from the nearby Endeavor segment of the Juan de Fuca Ridge. The main distinction is that it has a slightly higher content of Al_2O_3 relative to MgO than typical basalt from the Juan de Fuca Ridge south of the Cobb propagator (Karsten et al., 1990). The recovered samples crystallized from moderately evolved magmas and range from highly phyric olivine-plagioclase-clinopyroxene basalt, through phyric plagioclase basalt, to aphyric basalt. They probably were erupted at different stages of a magmatic cycle that is typical of medium- to slow-spreading ridges. Well-defined quench margins, abundant fresh glass, and spherulitic texture suggest that they are pillow basalts. The samples are fresh, with secondary minerals including calcite, smectite, celadonite, and, rarely, talc, restricted to a few samples with filled vesicles and altered olivine. The deepest rocks recovered from Hole 855D had a fracture-fill of greenschist mineralogy, but petrographic examination revealed no substantial penetrative metamorphism or replacement.

Sediment at Site 855, as elsewhere in Middle Valley, consists mainly of turbidites shed from the western margin of North America, alternating with hemipelagic sediment. A single lithologic unit was defined at Site 855, consisting of dark green to gray clay, silty clay, and quartz-plagioclase sandy silt and silty sand, comprising fining-

Table 17. Composition of basalts from Site 855.

Hole	855A	855A	855A	855D
Core, section	8R-1	9R-1	9R-1	5R-1
Interval (cm)	26–28	26–28	37–39	29–31
Depth (mbsf)	65.06	74.56	74.67	108.79
(wt%)				
SiO_2	49.55	50.35	50.64	50.60
TiO_2	1.75	1.47	1.50	1.61
Al_2O_3	15.90	14.84	14.48	14.38
Fe_2O_3	10.83	10.50	10.50	11.06
MnO	0.20	0.18	0.18	0.19
MgO	6.89	7.70	7.54	7.81
CaO	12.37	11.96	12.53	12.09
Na_2O	2.06	2.43	2.29	2.21
K_2O	0.17	0.11	0.10	0.12
P_2O_5	0.19	0.13	0.13	0.14
Total	99.91	99.67	99.89	100.21
LOI			2.90	
CO_2	0.40	0.44	0.44	0.45
H_2O	0.39	0.79	0.58	0.39
(ppm)				
Rb	2	1	1	2
Sr	103	127	126	116
Y	41	32	33	37
Zr	137	114	114	120
Nb	4	5	5	3
Ni	113	80	73	71
Cr	348	246	289	283
V	336	308	333	356
Cu	64	66	74	74
Zn	80	58	59	81
Ba	27	27	37	29

upward turbidite sequences. The turbidites range in thickness from 13 to 131 cm; Hole 855C, which recovered the most complete section, cored 28 of these sequences in 98 m of penetration. The coarser fraction of the sediment contains mainly plagioclase and quartz, with subordinate amounts of chlorite, mica (mostly biotite), and amphibole. The finer fraction contains mainly chlorite, illite, and quartz. Accessory minerals include zircon and, locally, pyrite, calcite, glauconite, and opaque minerals. Biogenic components are nearly ubiquitous and include foraminifers, diatoms, radiolarians, siliceous spicules, and nannofossils. The average composition of the sediment is approximately 59% SiO_2, 16% Al_2O_3, 7.6% Fe_2O_3, 3.7% MgO, 4.0% CaO, 2.4% Na_2O, 2.0% K_2O, 4.0% H_2O, and 0.7% CO_2 by weight. There is no progressive change in sediment composition with depth. Inter-

Table 18. Normative mineral content of basalts from Site 855.

Hole:	855A	855A	855A	855D
Core, section:	8R-1	9R-1	9R-1	5R-1
Interval (cm):	26–28	26–28	37–39	29–31
Quartz	0.47	0.00	0.32	0.37
Anorthite	33.96	29.60	29.21	29.17
Albite	17.60	20.80	19.56	18.31
Orthoclase	1.02	0.66	0.60	0.67
Diopside	22.09	24.28	26.84	25.51
Hypersthene	19.64	18.66	18.90	21.05
Forsterite	0.00	0.85	0.00	0.00
Fayalite	0.00	0.63	0.00	0.00
Ilmenite	3.36	2.83	2.88	3.13
Magnetite	1.44	1.40	1.40	1.49
Apatite	0.42	0.29	0.29	0.29
Total	100.00	100.00	100.00	100.00

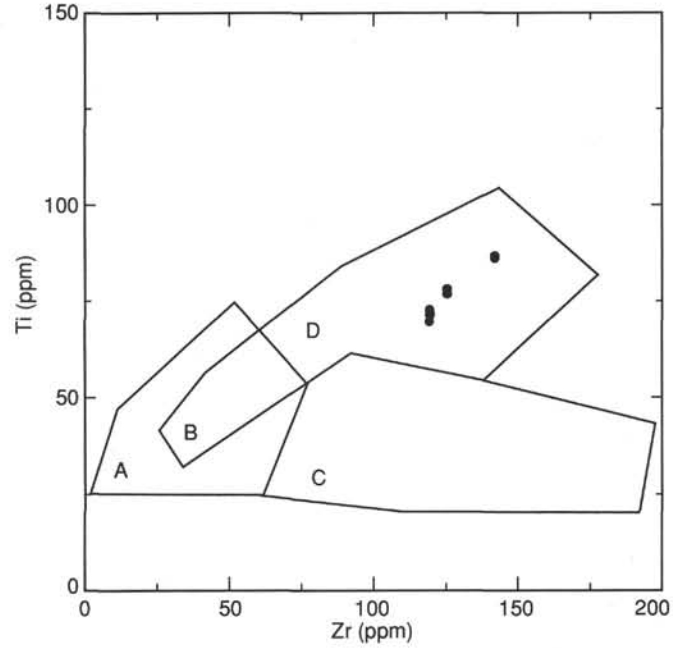

Figure 42. Ti vs. Zr. The slightly curvilinear array is typically produced by fractional crystallization. Ocean-floor basalt plots in fields D and B, low potassium tholeiite in fields A and B, and calc-alkali basalt in fields C and B. Field boundaries from Pearce and Cann (1973).

element correlations reflect the different mineralogy of the coarse vs. fine fractions. Most of the trace elements reside in the fine fraction. The sediment has a consistent ratio of Zn to Cu of 1.8, which may be useful in evaluating the contribution of the sediment to metallogenesis in Middle Valley.

The Holocene-Pleistocene boundary was recognized in two of the four holes, from the relative frequency of dextral to sinistral *Neogloboquadrina pachyderma,* and all samples have been tentatively assigned to Zones CD1 and CD2 of Lagoe and Thompson (1988). The precise depth of the Holocene-Pleistocene boundary has not yet been determined but it generally falls within the uppermost core. The calcareous nannofossil assemblages are characteristic of the lower part of Zone NN21 of Martini (1971), while the upper part of this zone was not found at Site 855. Although the assemblage in a few deeper samples resembles that of Zone NN20, this is probably an artifact of poor preservation, and the sediment cored is probably therefore no older than latest Pleistocene. The planktonic foraminiferal fauna, which bears species typical of subarctic waters, is much more abundant in Holocene samples than in Pleistocene samples, in which mineral grains predominate. The bathyal benthic foraminiferal fauna likewise changes markedly at this series boundary: the Holocene fauna contains few or no taxa reworked from the continental shelf, whereas the Pleistocene fauna contains numerous specimens from the shelf. The faunal changes in both planktonic and benthic foraminifers near the Holocene-Pleistocene boundary thus suggest that the continental shelf was a much more frequent source of turbidites during the latest Pleistocene than during the Holocene.

Natural remanent magnetization of the sediment is consistently high, ranging from 10 to 100 mA/m, probably because of fine-grained titanomagnetite deposited by the turbidites. This magnetization is stable against alternating field demagnetization, with a median destructive field of 23 to 30 mT. Magnetic susceptibility is also high, about 2×10^{-3}, and shows many peaks with depth that correlate well with individual turbidite layers. Over some intervals, the amplitude of these peaks varies from one interval to another, suggesting a change in the magnetite content of the turbidites with depth and hence

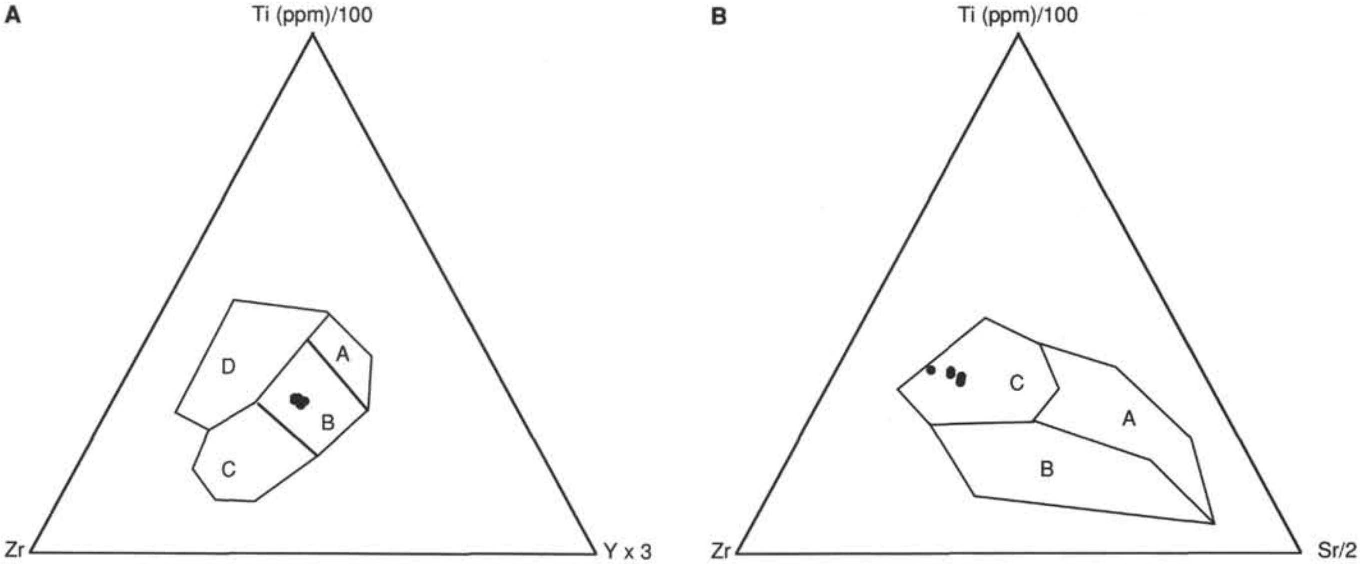

Figure 43. **A.** Ti-Zr-Y. Ocean-floor tholeiite compositions lie in field B, low-potassium tholeiite in fields A and B, continental basalt in field D, and calc-alkali basalt in fields C and B. **B.** Ti-Zr-Sr. Ocean-floor tholeiite compositions lie in field C, low potassium tholeiite in field A, and calc-alkali compositions in field B. Field boundaries from Pearce and Cann (1973).

probably in their source area with time. The basalt recovered has magnetic susceptibility about one order of magnitude higher than the sediment. We could not detect reliable evidence of geomagnetic excursions because these cores, collected with the rotary core barrel, are too disturbed.

Pore waters change in composition with depth, mainly as a result of reaction with the sediment, but then return to the composition of bottom seawater in each hole as the basalt at the bottom is approached. Chlorinity, alkalinity, calcium, sodium, silica, ammonium, and phosphate all display a maximum, and sulfate and magnesium a minimum, in the sediment section. The main reactions are: bacterial degradation of organic matter utilizing sulfate as an oxidant, which produces alkalinity and releases ammonium and phosphate; precipitation of calcium carbonate in response to the elevated alkalinity; dissolution of biogenic silica; and leaching of calcium and uptake of sodium, potassium, and magnesium by detrital silicates undergoing alteration. Chlorinity shows the typical 2% increase between 0 and about 30 mbsf that results from downward diffusion of the more saline bottom water that prevailed during the Pleistocene. The presence of this maximum precludes vertical flow through the sediment column at velocities greater than about 1 mm/yr since the last glacial maximum, about 20 ka ago. That the basal pore water in all four holes so closely resembles bottom seawater, in spite of extensive reaction in the sediment, indicates that seawater is being drawn down into the basalt layer along the rift-bounding fault at a significant rate. Calcium and magnesium both show a lateral gradient in the basal pore water that suggests that the basement fluid becomes more altered farther from the fault.

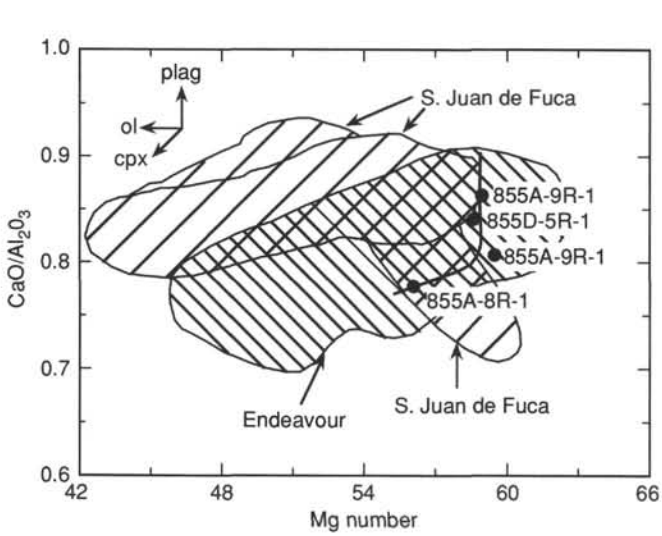

Figure 44. CaO/Al_2O_3 vs. Mg number. Field boundaries from Karsten et al. (1990). The near-vertical trend of three samples results from plagioclase fractionation. Clinopyroxene (cpx) or olivine (ol) must have joined plagioclase (plag) as a crystallization phase to produce the fourth, more evolved sample.

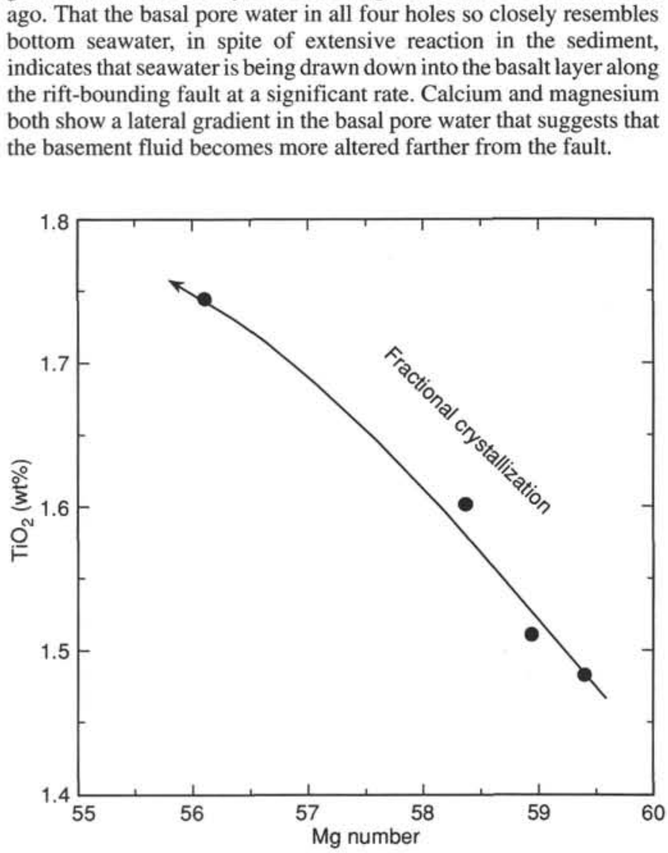

Figure 45. TiO_2 vs. Mg number. The linear array is characteristic of low-pressure crystal fractionation.

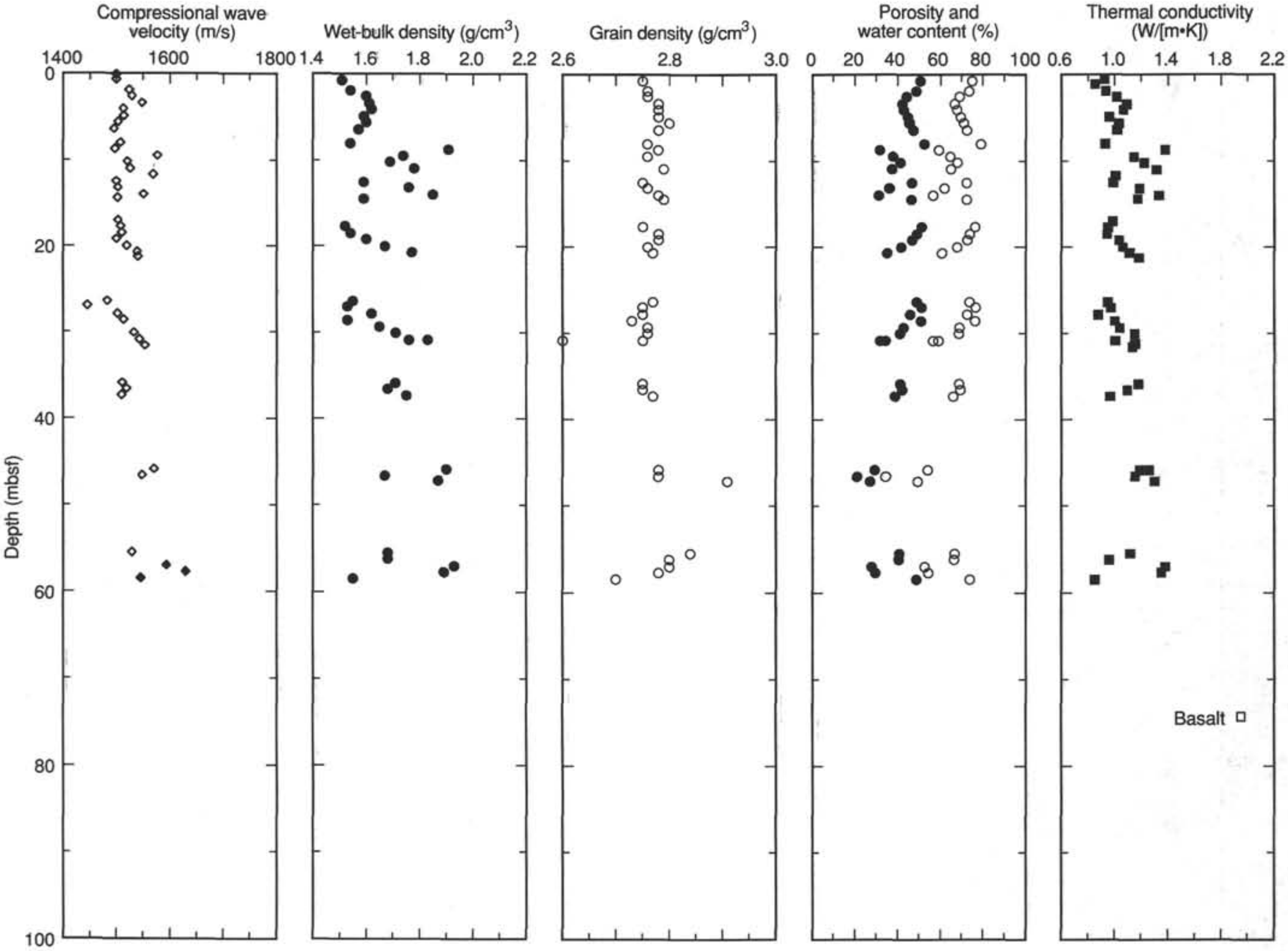

Figure 46. Compressional wave velocity, index properties, and thermal conductivities vs. depth for Hole 855A. Porosities are shown as open circles, water contents as solid circles.

The organic and inorganic carbon contents of the sediment are about 0.4 and 0.2 wt%, respectively, except in the upper 20 mbsf, where some samples exceed 1 to 2 wt%. Sulfur is about 0.2 wt%. Methane in headspace gas ranges from 2 to 6 ppm (v/v) and no ethane or higher hydrocarbons, nor hydrogen sulfide, were detected. These low methane concentrations, coupled with only a partial (25%) depletion of sulfate from the pore waters, indicate that environmental conditions are not favorable for methanogenesis in the sediment. Concentrations of extractable organic matter are extremely low, based on color and intensity of fluorescence; nevertheless, some thermally mature and overmature bitumen appears to be present deeper in the holes. The dominant compound series in the hexane extracts are hydrocarbons ranging from n-C_{15} to n-C_{35}, with pristane ($C_{19}H_{40}$) as the major isoprenoid alkane. The n-alkanes $>C_{26}$ have a significant predominance of odd carbon numbers (CPI >1.0), typical for immature hydrocarbons that originate from terrestrial higher plants. The n-alkane patterns $<C_{24}$ are typical for autochthonous marine bitumen derived from microbial lipids. The sedimentary lipids also contain major amounts of alkenones, molecular fossils indicative of marine algae such as coccolithophorids. Thermal maturation is evident in the CPI, the isoprenoid to normal hydrocarbon ratio, and the pristane to phytane ratio, all of which decrease with depth. These data suggest that the geothermal gradient has been higher in the past than at present, as the deepest sediments have been exposed to temperatures high enough (50°C or slightly higher) to take them into the beginning of the oil window, whereas the present temperature at 100 mbsf is only about 33°C. This conclusion is consistent with the advanced degree of dissolution of foraminifers and calcareous nannofossils with depth. We infer that the cooler conditions that prevail at present were caused by the faulting, which created a path for fluid recharge.

The sediment shows an increase in wet-bulk density, velocity, and thermal conductivity with depth below about 40 mbsf, and a corresponding decrease in porosity and water content, as it becomes more indurated. Temperature measurements in the sediment indicate a linear thermal gradient of 0.328°C/m over the upper 76 mbsf. Coupled with the average thermal conductivity of 1.2 W/(m·K), this gradient yields a conductive heat flow of 394 mW/m^2, lower than the approximately 500 mW/m^2 measured farther west of the fault. The lower heat flow at Site 855 may result from cold seawater being drawn down into the basaltic layer, as indicated by the pore-water data. There is no thermal evidence for fluid flow through the sediment, consistent with the limit of <1 mm/yr placed on vertical flow by the chlorinity data.

REFERENCES

Bandy, O. L., 1960. The geological significance of coiling ratios in the foraminifer *Globigerina pachyderma* (Ehrenberg). *J. Paleontol.*, 34:671–681.

Brigaud, F., and Vasseur, G., 1989. Mineralogy, porosity and fluid control on thermal conductivity of sedimentary rock. *Geophys. J.*, 98:525–542.

Broecker, W. S., and Peng, T. H., 1982. *Tracers in the Sea:* Palisades, NY (Lamont-Doherty Geological Observatory).

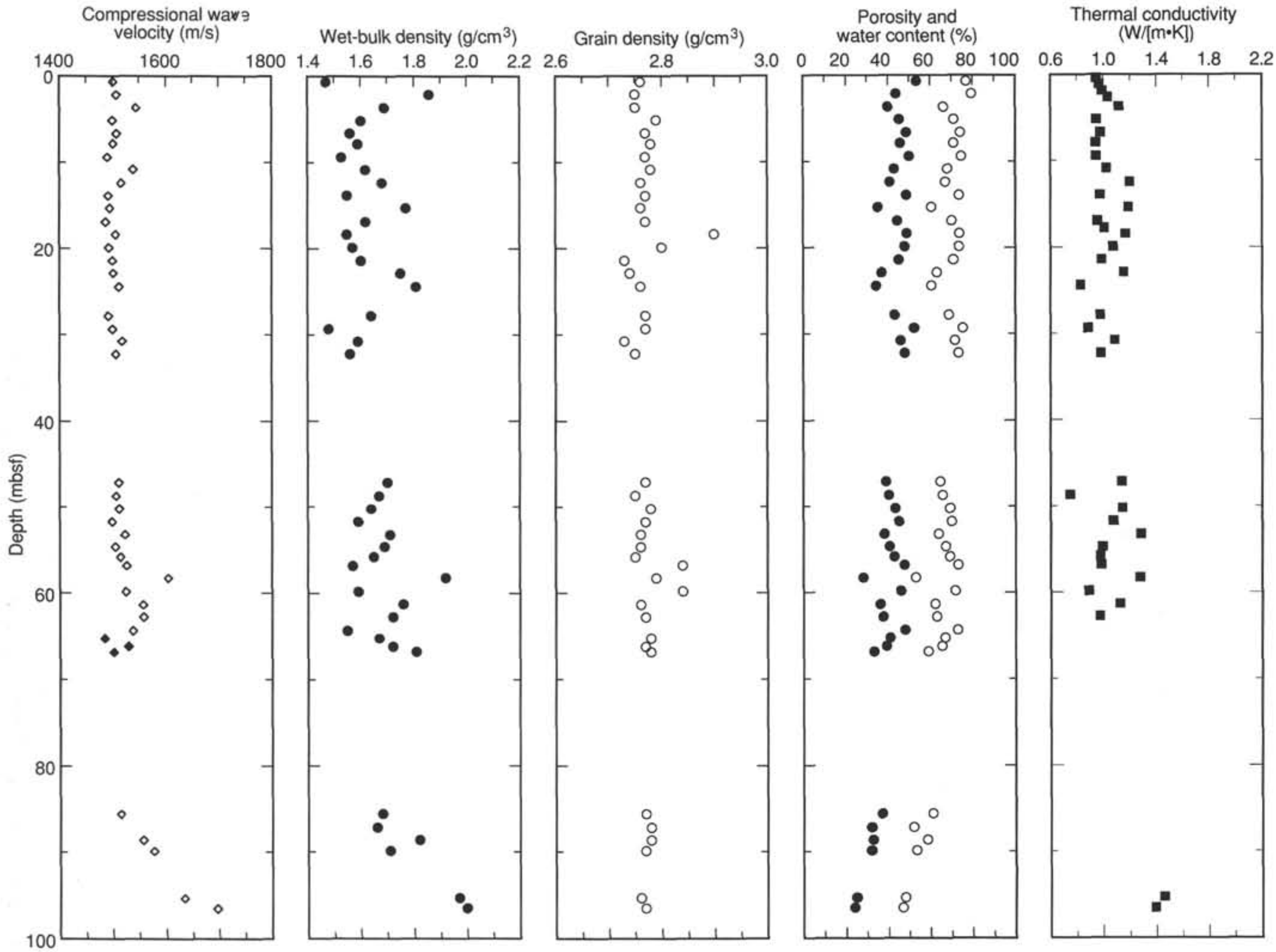

Figure 47. Compressional wave velocity, index properties, and thermal conductivities vs. depth for Hole 855C. Porosities are shown as open circles, water contents as solid circles.

Claypool, G. E., and Kaplan, I. R., 1974. The origin and distribution of methane in marine sediments. *In* Kaplan, I. R. (Ed.), *Natural Gases in Marine Sediments:* New York (Plenum), 99–139.

Didyk, B. M., Simoneit, B.R.T., Brassell, S. C., and Eglinton, G., 1978. Organic geochemical indicators of palaeoenvironmental conditions of sedimentation. *Nature,* 272:216–222.

Emeis, K.-C., and Kvenvolden, K. A., 1986. Shipboard organic geochemistry on *JOIDES Resolution. ODP Tech. Note,* 7.

Farrington, J. W., Davis, A. C., Tarafa, M. E., McCaffrey, M. A., Whelan, J. K., and Hunt, J. M., 1988. Bitumen molecular maturity parameters in the Ikpikpuk well, Alaskan North Slope. *Org. Geochem.,* 13:303–310.

Hamilton, E. L., 1976. Variation of density and porosity with depth in deep-sea sediments. *J. Sediment. Petrol.,* 46:280–300.

Hays, J. D., Saito, T., Opdyke, N. D., and Burckle, L. H., 1969. Pliocene-Pleistocene sediments of the equatorial Pacific: their paleomagnetic, biostratigraphic and climate record. *Geol. Soc. Am. Bull.,* 80:1481–1514.

Imbrie, J., Hays, J. D., Martinson, D. G., McIntyre, A., Mix, A. C., Morley, J. J., Pisias, N. G., Prell, W. L., and Shackleton, N. J., 1984. The orbital theory of Pleistocene climate: support from a revised chronology of the marine $\delta^{18}O$ record. *In* Berger, A., Imbrie, J., Hays, J., Kukla, G., and Saltzman, B., *Milankovitch and Climate* (Pt. 1): Dordrecht (D. Reidel), 269–306.

Johnson, H. P., Franklin, J. M., and Currie, R. G., in press. SeaMARC IA acoustic imagery of the Middle Valley Area, Northern Juan de Fuca Ridge. *Geol. Surv. Can. Open File Rep.*

Karsten, J. L., Delaney, J. R., Rhodes, J. M., and Liias, A., 1990. Spatial and temporal evolution of magmatic systems beneath the Endeavour Segment, Juan de Fuca Ridge: tectonic and petrologic constraints. *J. Geophys. Res.,* 95:19235–19256.

Lagoe, M. B., and Thompson, P. R., 1988. Chronostratigraphic significance of Late Cenozoic planktonic foraminifera from the Ventura Basin, California: potential for improving tectonic and depositional interpretation. *J. Foraminiferal Res.,* 18:250–266.

Marlowe, I. T., Brassell, S. C., Eglinton, G., and Green, J. C., 1984. Long chain unsaturated ketones and esters in living algae and marine sediments. *Org. Geochem.,* 6:135–141.

Martini, E., 1971. Standard Tertiary and Quaternary calcareous nannoplankton zonation. *In* Farinacci, A. (Ed.), *Proc. 2nd Planktonic Conf. Roma:* Rome (Ed. Tecnosci.), 2:739–785.

McDuff, R. E., 1985. The chemistry of interstitial waters, Deep Sea Drilling Project Leg 86. *In* Heath, G. R., Burckle, L. H., et al., *Init. Repts. DSDP,* 86: Washington (U.S. Govt. Printing Office), 675–687.

Pearce, J. A., and Cann, J. R., 1973. Tectonic setting of basic volcanic rocks determined using trace element analyses. *Earth Planet. Sci. Lett.,* 19:290–300.

Rohr, K. M., Davis, E. E., and Hyndman, R. D., 1992. Multichannel seismic reflection profiles across Middle Valley, Northern Juan de Fuca Ridge. *Geol. Surv. Can. Open File Rep.,* 2476.

Shipboard Scientific Party, 1982. Guaymas Basin: Sites 477, 478, and 481. *In* Curray, J. R., Moore, D. G., et al., *Init. Repts. DSDP,* 64 (Pt. 1): Washington (U.S. Govt. Printing Office), 210–415.

Simoneit, B.R.T., 1977. Diterpenoid compounds and other lipids in deep-sea sediments and their geochemical significance. *Geochim. Cosmochim. Acta,* 41:463–476.

———, 1978. The organic chemistry of marine sediments. *In* Riley, J. F., and Chester, R. (Eds.), *Chemical Oceanography* (2nd ed.) (Vol. 7): New York (Academic Press), 233–311.

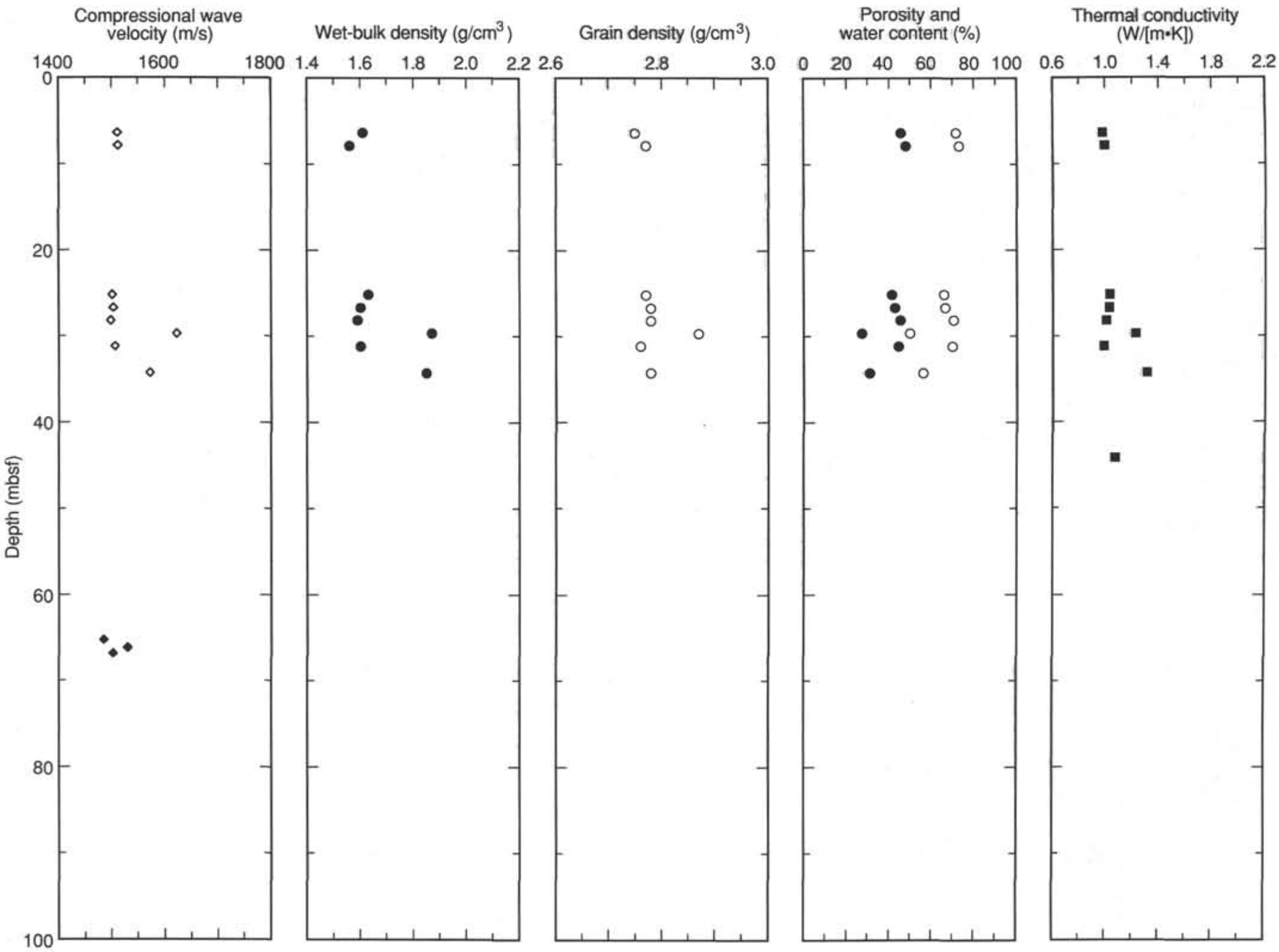

Figure 48. Compressional wave velocity, index properties, and thermal conductivities vs. depth for Hole 855B. Porosities are shown as open circles, water contents as solid circles.

Simoneit, B.R.T., Brenner, S., Peters, K. E., and Kaplan, I. R., 1981. Thermal alteration of Cretaceous black shale by basaltic intrusions in the eastern Atlantic. II: effects on bitumen and kerogen. *Geochim. Cosmochim. Acta,* 45:1581–1602.

Simoneit, B.R.T., Goodfellow, W. D., and Franklin, J. M., in press. Hydrothermal petroleum at the seafloor and organic matter alteration in sediments of Middle Valley, northern Juan de Fuca Ridge. *Applied Geochem.*

Telford, W. M., Geldart, L. P., Sheritt, R. E., and Keys, D. A., 1976. *Applied Geophysics:* Cambridge (Cambridge Univ. Press).

Volkman, J. K., Eglinton, G., Corner, E.D.S. and Sargent, J. R., 1980. Novel unsaturated straight-chain C_{37}–C_{39} methyl and ethyl ketones in marine sediments and a coccolithophore *Emiliania huxleyi. In* Douglas, A. G., and Maxwell, J. R. (Eds.), *Advances in Organic Geochemistry 1979:* Oxford (Pergamon Press), 219–228.

Ms 139A-105

NOTE: For all sites drilled, core description forms ("barrel sheets") and core photographs have been printed on coated paper and bound as Section 3, near the back of the book, beginning on page 573. Forms containing smear slide data are bound as Section 4, beginning on page 933. Thin-section data are given in Section 5, beginning on page 949.

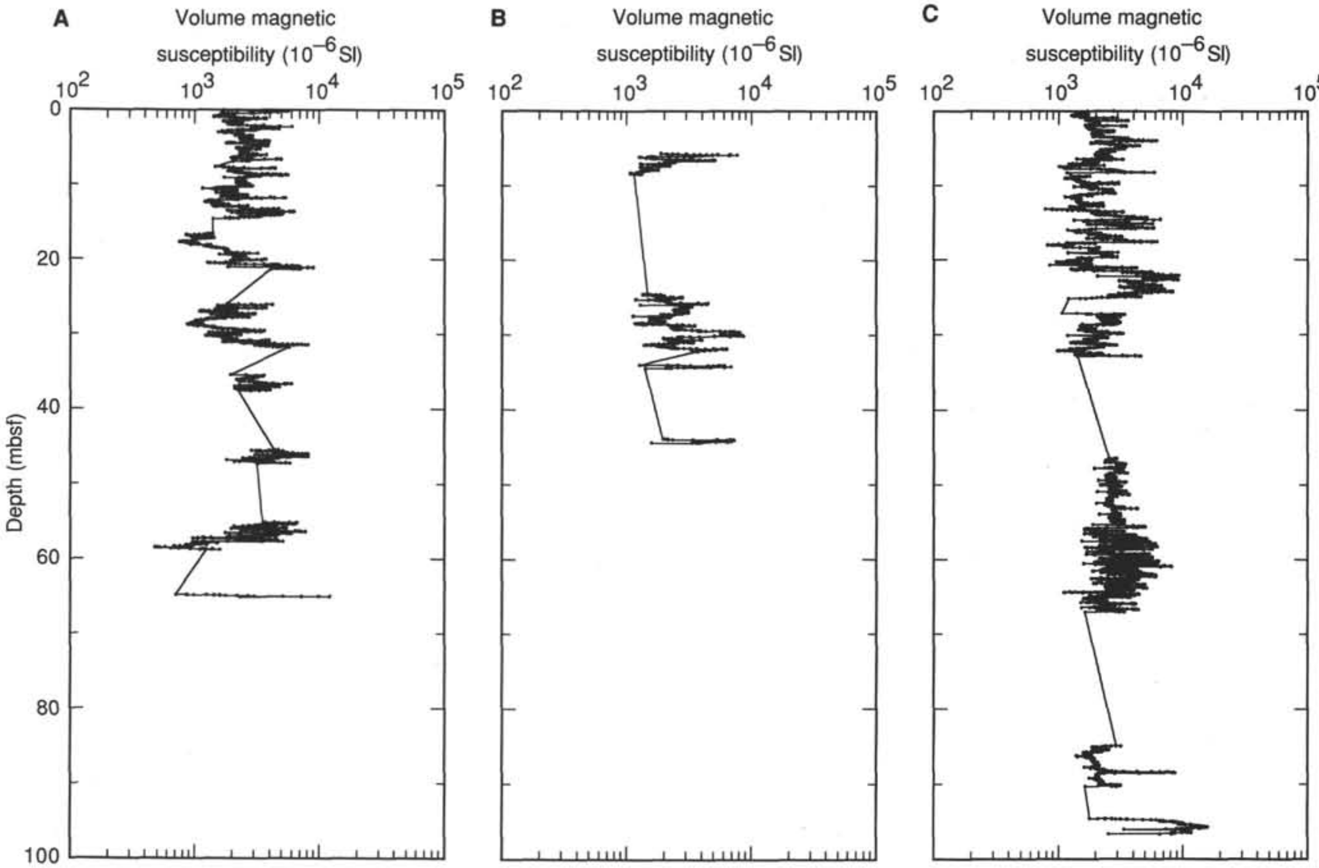

Figure 49. Volume magnetic susceptibility vs. depth for Holes 855A (**A**), 855B (**B**), and 855C (**C**). The gaps in the data reflect low core recovery.

Table 19. Summary of average physical properties at Site 855.

	Units	N[a]	Mean	Standard deviation	Minimum	Maximum
Hole 855A sediment (depth interval 0–60 mbsf)						
Acoustic velocity	m/s	40	1520	25.2	1446	1577
Thermal conductivity	W/m·K	84	1.08	0.14	0.85	1.38
Wet-bulk density	g/cm^3	41	1.67	0.12	1.51	1.93
Grain density	g/cm^3	40	2.77	0.04	2.60	2.90
Porosity	%	40	67.4	7.3	49.7	79.2
Hole 855A basalt						
Thermal conductivity	W/m·K	4	1.95	0.07	1.86	2.06
Hole 855C sediment (depth interval 0–95 mbsf)						
Acoustic velocity	m/s	40	1526	42.4	1487	1697
Thermal conductivity	W/m·K	38	1.05	0.15	0.75	1.46
Wet-bulk density	g/cm^3	43	1.67	0.12	1.47	2.00
Grain density	g/cm^3	43	2.78	0.05	2.73	3.02
Porosity	%	43	66.6	7.7	46.7	79.6
Hole 855D basalt						
Thermal conductivity	W/m·K	4	2.03	0.03	1.96	2.04

[a]Number of measurements. For sediments, N represents the number of samples measured. For hard rocks, all measurements were made twice so that the number of samples is half the number of measurements.

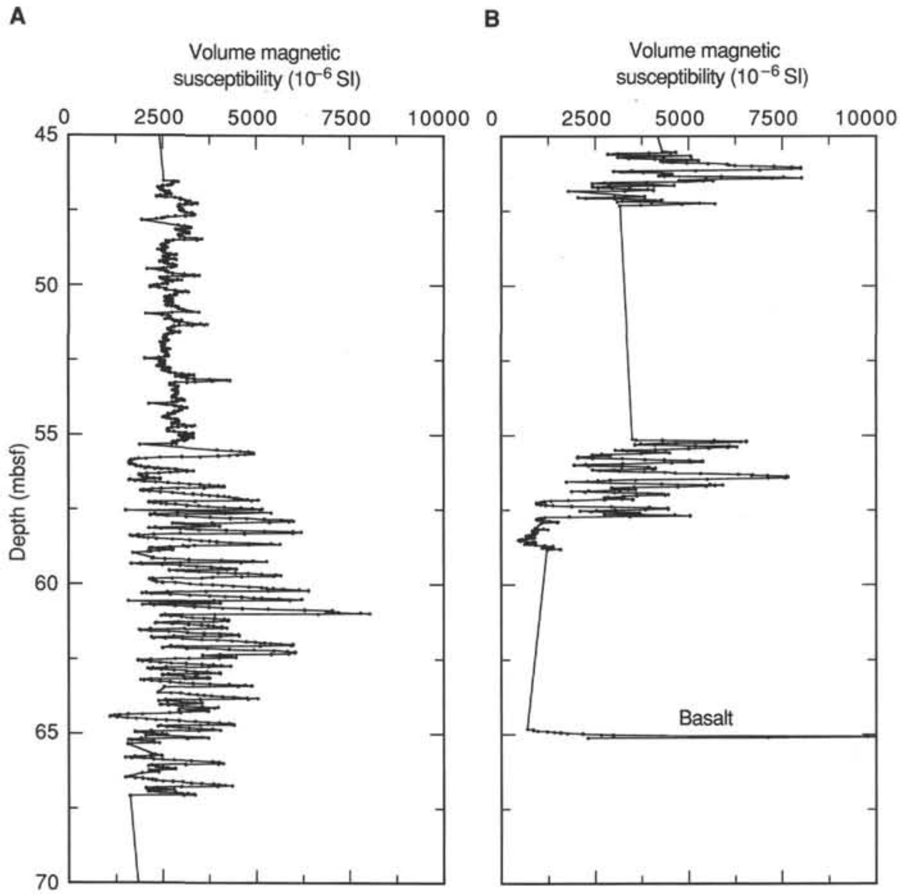

Figure 50. **A.** Change in volume magnetic susceptibility signature in Hole 855C, at a depth of 55 to 67 mbsf, associated with small and frequent turbidites. **B.** Large changes in volume magnetic susceptibility in Hole 855A, at a depth of 45 to 59 mbsf, associated with small and frequent turbidites.

Table 20. Index properties for Hole 855A.

Core, section, interval (cm)	Depth (mbsf)	Wet-bulk density (g/cm^3)	Grain density (g/cm^3)	Wet porosity (%)	Wet water content (%)	Void ratio
139-855A-						
1R-1, 73–76	0.73	1.51	2.75	75.0	50.8	2.99
1R-2, 41–43	1.91	1.54	2.76	73.6	48.9	2.79
1R-2, 107–109	2.57	1.60	2.76	69.0	44.2	2.23
1R-3, 40–43	3.40	1.61	2.78	66.8	42.4	2.01
1R-3, 108–111	4.08	1.62	2.78	67.9	42.9	2.11
1R-4, 41–43	4.91	1.59	2.78	69.6	44.7	2.29
1R-4, 107–109	5.57	1.60	2.80	71.1	45.5	2.46
1R-5, 41–44	6.41	1.57	2.78	72.5	47.3	2.63
2R-1, 41–44	8.01	1.54	2.76	79.2	52.7	3.81
2R-1, 110–113	8.70	1.91	2.78	59.4	31.9	1.46
2R-2, 37–40	9.47	1.74	2.76	64.8	38.1	1.84
2R-2, 110–113	10.20	1.69	0.58	68.3	41.4	2.16
2R-3, 37–40	10.97	1.78	2.79	65.2	37.5	1.87
2R-4, 41–44	12.51	1.59	2.75	72.5	46.7	2.64
2R-4, 107–110	13.17	1.76	2.76	62.0	36.2	1.63
2R-5, 38–41	13.98	1.85	2.78	56.6	31.4	1.31
2R-5, 85–88	14.45	1.59	2.79	72.4	46.6	2.62
3R-1, 108–111	17.68	1.52	2.75	76.4	51.4	3.23
3R-2, 41–44	18.51	1.54	2.78	73.9	49.1	2.82
3R-2, 110–113	19.20	1.60	2.78	72.8	46.7	2.68
3R-3, 40–43	20.00	1.67	2.76	67.8	41.7	2.11
3R-3, 110–113	20.70	1.77	2.77	60.9	35.2	1.56
4R-1, 38–40	26.38	1.55	2.77	73.9	49.0	2.83
4R-1, 101–104	27.01	1.53	2.75	76.6	51.3	3.28
4R-2, 37–40	27.87	1.62	2.75	72.7	45.9	2.66
4R-2, 108–111	28.58	1.53	2.73	76.5	51.1	3.26
4R-3, 39–41	29.39	1.65	2.76	69.0	42.9	2.22
4R-3, 107–110	30.07	1.71	2.76	68.8	41.2	2.21
4R-4, 38–41	30.88	1.76	2.75	59.2	34.4	1.45
4R-4, 38–41	30.88	1.83	2.60	56.6	31.7	1.30
5R-1, 36–39	35.86	1.71	2.75	69.1	41.5	2.24
5R-1, 106–109	36.56	1.68	2.75	69.6	42.3	2.29
5R-2, 34–38	37.34	1.75	2.77	66.4	38.8	1.98
6R-1, 38–41	45.88	1.90	2.78	54.0	29.2	1.18
6R-1, 109–113	46.59	1.67	2.78	34.5	21.2	0.53
6R-2, 16–20	47.16	1.87	2.91	49.7	27.3	0.99
7R-1, 38–41	55.48	1.68	2.84	66.7	40.8	2.00
7R-1, 108–112	56.18	1.68	2.80	66.6	40.7	1.99
7R-2, 38–40	56.98	1.93	2.80	52.8	28.0	1.12
7R-2, 108–112	57.68	1.89	2.78	54.4	29.4	1.19
7R-3, 36–40	58.46	1.55	2.70	73.9	48.9	2.83

Table 21. Compressional wave velocity for Hole 855A.

Core, section, interval (cm)	Depth (mbsf)	DSV velocity (m/s)
139-855A-		
1R-1, 10–10	0.10	1500
1R-1, 70–70	0.70	1524
1R-2, 41–41	1.91	1529
1R-2, 110–110	2.60	1548
1R-3, 40–40	3.40	1513
1R-3, 110–110	4.10	1514
1R-4, 40–40	4.90	1503
1R-4, 110–110	5.60	1495
1R-5, 40–40	6.40	1508
2R-1, 40–40	8.00	1498
2R-1, 110–110	8.70	1577
2R-2, 40–40	9.50	1521
2R-2, 110–110	10.20	1526
2R-3, 40–40	11.00	1569
2R-3, 110–110	11.70	1500
2R-4, 40–40	12.50	1503
2R-4, 110–110	13.20	1551
2R-5, 40–40	14.00	1502
2R-5, 80–80	14.40	1524
3R-1, 40–40	17.00	1503
3R-1, 110–110	17.70	1508
3R-2, 40–40	18.50	1510
3R-2, 110–110	19.20	1500
3R-3, 40–40	20.00	1519
3R-3, 110–110	20.70	1539
3R-4, 15–15	21.25	1541
4R-1, 40–40	26.40	1483
4R-1, 95–95	26.95	1446
4R-2, 40–40	27.90	1502
4R-2, 110–110	28.60	1514
4R-3, 40–40	29.40	1518
4R-3, 110–110	30.10	1533
4R-4, 40–40	30.90	1543
4R-4, 110–110	31.60	1553
5R-1, 40–40	35.90	1511
5R-1, 110–110	36.60	1519
5R-2, 34–34	37.34	1510
6R-1, 40–40	45.90	1570
6R-1, 110–110	46.60	1548
7R-1, 40–40	55.50	1529

Note: DSV = digital sound velocimeter.

Table 22. Thermal conductivities for Hole 855A.

Sample (cm)	Depth (mbsf)	Thermal conductivity (W/m·K)
139-855A-		
1R-1, 50	0.50	0.93
1R-1, 110	1.10	0.85
1R-2, 40	1.90	0.94
1R-2, 110	2.60	1.02
1R-3, 40	3.40	1.09
1R-3, 110	4.10	1.07
1R-4, 40	4.90	0.96
1R-4, 110	5.60	1.03
1R-5, 40	6.40	1.02
2R-1, 40	8.00	0.93
2R-1, 110	8.70	1.38
2R-2, 40	9.50	1.15
2R-2, 110	10.20	1.22
2R-3, 40	11.00	1.32
2R-3, 110	11.70	1.01
2R-4, 40	12.50	0.99
2R-4, 110	13.20	1.19
2R-5, 40	14.00	1.34
2R-5, 80	14.40	1.17
3R-1, 40	17.00	0.99
3R-1, 110	17.70	0.95
3R-2, 40	18.50	0.94
3R-2, 110	19.20	1.03
3R-3, 40	20.00	1.06
3R-3, 110	20.70	1.12
3R-4, 16	21.26	1.19
4R-1, 40	26.40	0.95
4R-1, 110	27.10	0.97
4R-2, 40	27.90	0.88
4R-2, 110	28.60	1.00
4R-3, 40	29.40	1.04
4R-3, 110	30.10	1.15
4R-4, 40	30.90	1.01
4R-4, 80	31.30	1.16
4R-4, 110	31.60	1.13
5R-1, 40	35.90	1.18
5R-1, 110	36.60	1.10
5R-2, 34	37.34	0.97
6R-1, 40	45.90	1.26
6R-1, 40	45.90	1.19
6R-1, 110	46.60	1.16
6R-2, 18	47.18	1.31
7R-1, 40	55.50	1.12
7R-1, 110	56.20	0.96
7R-2, 40	57.00	1.38
7R-2, 110	57.70	1.35
7R-3, 40	58.50	0.85
9R-1, 1	74.51	[a]1.96

[a] Basalt, mean of five measurements.

Table 23. Index properties for Hole 855B.

Core, section, interval (cm)	Depth (mbsf)	Wet-bulk density (g/cm^3)	Grain density (g/cm^3)	Wet porosity (%)	Wet water content (%)	Void ratio
139-855B-						
2R-1, 68–72	6.38	1.61	2.75	71.8	45.7	2.54
2R-2, 68–72	7.88	1.56	2.77	73.1	48.0	2.71
4R-1, 68–72	25.18	1.63	2.77	65.9	41.5	1.93
4R-2, 68–72	26.68	1.60	2.78	66.7	42.8	2.00
4R-3, 68–72	28.18	1.59	2.78	70.5	45.5	2.38
4R-4, 68–72	29.68	1.87	2.87	49.9	27.3	0.99
4R-5, 68–72	31.18	1.60	2.76	69.9	44.7	2.32
5R-1, 28–32	34.28	1.85	2.78	56.1	31.0	1.28

Table 24. Compressional wave velocity for Hole 855B.

Core, section, interval (cm)	Depth (mbsf)	DSV velocity (m/s)
139-855B-		
2R-1, 70–70	6.40	1511
2R-2, 70–70	7.90	1513
4R-1, 70–70	25.20	1502
4R-2, 70–70	26.70	1503
4R-3, 70–70	28.20	1498
4R-4, 70–70	29.70	1623
4R-5, 70–70	31.20	1506
5R-1, 30–30	34.30	1572

Note: DSV = digital sound velocimeter.

Table 25. Thermal conductivities for Hole 855B.

Sample (cm)	Depth (mbsf)	Thermal conductivity (W/m·K)
139-855B-		
2R-1, 70	6.40	0.98
2R-2, 70	7.90	0.99
4R-1, 70	25.20	1.03
4R-2, 70	26.70	1.03
4R-3, 70	28.20	1.00
4R-4, 70	29.70	1.20
4R-5, 70	31.20	0.99
5R-1, 30	34.30	1.31
6R-1, 30	44.20	1.08

Table 26. Index properties for Hole 855C.

Core, section, interval (cm)	Depth (mbsf)	Wet-bulk density (g/cm^3)	Grain density (g/cm^3)	Wet porosity (%)	Wet water content (%)	Void ratio
139-855C-						
1R-1, 68–72	0.68	1.47	2.76	76.9	53.7	3.32
1R-2, 68–72	2.18	1.86	2.75	79.6	43.9	3.91
1R-3, 68–70	3.68	1.69	2.75	66.2	40.1	1.96
1R-4, 68–70	5.18	1.60	2.79	71.1	45.4	2.46
1R-5, 68–70	6.68	1.56	2.77	74.2	48.7	2.87
1R-6, 38–40	7.88	1.59	2.78	71.2	46.0	2.47
2R-1, 74–76	9.44	1.53	2.77	74.8	50.2	2.96
2R-2, 66–68	10.86	1.62	2.78	68.4	43.2	2.16
2R-3, 74–76	12.44	1.68	2.76	67.3	41.0	2.06
2R-4, 71–74	13.91	1.55	2.77	73.8	48.7	2.82
2R-5, 66–69	15.36	1.77	2.76	60.8	35.2	1.55
2R-6, 73–77	16.93	1.62	2.77	70.3	44.6	2.37
3R-1, 68–71	18.38	1.55	2.90	74.0	49.0	2.85
3R-2, 73–76	19.93	1.57	2.80	73.5	47.9	2.78
3R-3, 74–77	21.44	1.60	2.73	71.0	45.3	2.45
3R-4, 66–67	22.86	1.75	2.74	63.3	36.9	1.72
3R-5, 71–74	24.41	1.81	2.76	60.7	34.3	1.54
4R-1, 73–75	27.83	1.64	2.77	68.8	43.1	2.20
4R-2, 73–75	29.33	1.48	2.77	75.4	52.3	3.06
4R-3, 66–70	30.76	1.59	2.73	71.6	46.0	2.52
4R-4, 64–67	32.24	1.56	2.75	73.4	48.1	2.75
6R-1, 65–68	47.15	1.70	2.77	64.5	38.9	1.82
6R-2, 73–76	48.73	1.67	2.75	65.8	40.4	1.92
6R-3, 73–76	50.23	1.64	2.78	69.3	43.4	2.26
6R-4, 74–77	51.74	1.59	2.77	69.9	45.1	2.32
6R-5, 73–76	53.23	1.71	2.76	63.8	38.2	1.76
6R-6, 66–69	54.66	1.69	2.76	67.0	40.7	2.03
6R-7, 33–36	55.83	1.65	2.75	69.0	42.9	2.23
7R-1, 73–77	56.83	1.57	2.84	73.1	47.6	2.71
7R-2, 67–71	58.27	1.92	2.79	53.0	28.3	1.13
7R-3, 73–77	59.83	1.59	2.84	71.7	46.1	2.54
7R-4, 73–77	61.33	1.76	2.76	62.0	36.0	1.63
7R-5, 65–69	62.75	1.72	2.77	63.0	37.5	1.70
7R-6, 73–77	64.33	1.55	3.02	72.9	48.1	2.69
7R-7, 12–16	65.22	1.67	2.78	66.9	41.0	2.02
8R-1, 47–51	66.17	1.72	2.77	65.6	39.1	1.91
8R-2, 36–40	66.81	1.81	2.78	59.0	33.4	1.44
10R-1, 67–71	85.57	1.68	2.77	60.9	37.1	1.56
10R-3, 77–81	87.17	1.66	2.78	51.9	32.0	1.08
10R-4, 71–75	88.61	1.82	2.78	58.4	32.8	1.40
10R-5, 48–52	89.88	1.71	2.77	53.4	32.0	1.15
11R-1, 68–72	95.28	1.97	2.76	48.0	24.9	0.92
11R-2, 38–42	96.48	2.00	2.77	46.7	24.0	0.88

Table 27. Compressional wave velocity for Hole 855C.

Core, section, interval (cm)	Depth (mbsf)	DSV velocity (m/s)
139-855C-		
1R-1, 70–70	0.70	1502
1R-2, 70–70	2.20	1508
1R-3, 70–70	3.70	1544
1R-4, 70–70	5.20	1500
1R-5, 70–70	6.70	1508
1R-6, 40–40	7.90	1502
2R-1, 75–75	9.45	1490
2R-2, 67–67	10.87	1539
2R-3, 75–75	12.45	1516
2R-4, 75–75	13.95	1492
2R-5, 68–68	15.38	1495
2R-6, 75–75	16.95	1487
3R-1, 70–70	18.40	1506
3R-2, 75–75	19.95	1494
3R-3, 75–75	21.45	1500
3R-4, 68–68	22.88	1502
3R-5, 73–73	24.43	1513
4R-1, 75–75	27.85	1492
4R-2, 75–75	29.35	1500
4R-3, 68–68	30.78	1518
4R-4, 65–65	32.25	1506
6R-1, 67–67	47.17	1511
6R-2, 75–75	48.75	1506
6R-3, 74–74	50.24	1513
6R-4, 75–75	51.75	1498
6R-5, 74–74	53.24	1523
6R-6, 68–68	54.68	1505
6R-7, 34–34	55.84	1514
7R-1, 75–75	56.85	1526
7R-2, 69–69	58.29	1604
7R-3, 75–75	59.85	1524
7R-4, 75–75	61.35	1556
7R-5, 67–67	62.77	1558
7R-6, 75–75	64.35	1538
10R-1, 69–69	85.59	1514
10R-3, 79–79	87.17	1570
10R-4, 73–73	88.63	1556
10R-5, 50–50	89.90	1577
11R-1, 70–70	95.30	1634
11R-2, 40–40	96.50	1697

Note: DSV = digital sound velocimeter.

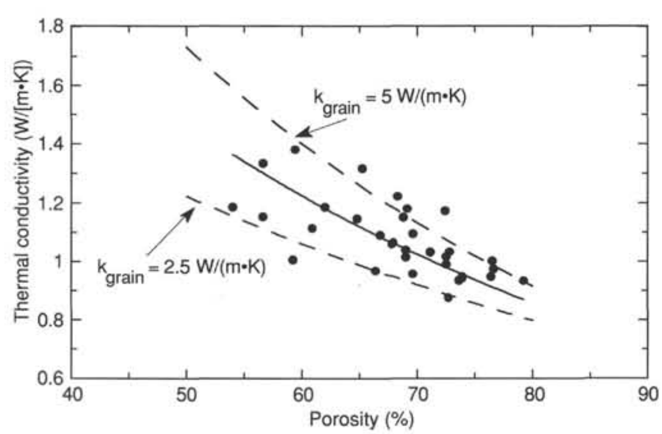

Figure 51. Correlation of thermal conductivity with porosity for measurements at Hole 855A. The data used are from a depth range of 0 to 40 mbsf. Dashed lines show the calculated geometric mean thermal conductivity for two different grain thermal conductivities. The solid line represents a best-fit geometric mean with a calculated best-fitting grain thermal conductivity of 3.6 W/(m·K).

Table 28. Thermal conductivities for Hole 855C.

Sample (cm)	Depth (mbsf)	Thermal conductivity (W/m·K)
139-855C-		
1R-1, 40	0.40	0.95
1R-1, 110	1.10	0.97
1R-2, 40	1.90	0.99
1R-2, 110	2.60	1.03
1R-3, 70	3.70	1.12
1R-4, 70	5.20	0.94
1R-5, 70	6.70	0.98
1R-6, 40	7.90	0.94
2R-1, 75	9.45	0.95
2R-2, 68	10.88	1.02
2R-3, 75	12.45	1.20
2R-4, 75	13.95	0.97
2R-5, 68	15.38	1.19
2R-6, 75	16.95	0.96
2R-7, 10	17.80	1.01
3R-1, 75	18.45	1.17
3R-2, 75	19.95	1.07
3R-3, 75	21.45	0.98
3R-4, 69	22.89	1.15
3R-5, 69	24.39	0.83
4R-1, 75	27.85	0.98
4R-2, 75	29.35	0.88
4R-3, 68	30.78	1.08
4R-4, 65	32.25	0.98
6R-1, 68	47.18	1.14
6R-2, 75	48.75	0.75
6R-3, 75	50.25	1.14
6R-4, 75	51.75	1.07
6R-5, 75	53.25	1.28
6R-6, 75	54.75	0.99
6R-7, 32	55.82	0.97
7R-1, 75	56.85	0.98
7R-2, 69	58.29	1.28
7R-3, 75	59.85	0.89
7R-4, 75	61.35	1.12
7R-5, 67	62.77	0.97
11R-1, 70	95.30	1.46
11R-2, 40	96.50	1.39

Table 29. Summary of *in-situ* temperature tool (WSTP) deployments at Site 855.

Core[a]	Depth[a] (mbsf)	Quality[b]	Temperature[c] (°C)
139-855A-4R	36.6	Battery failure	—
139-855C-4R	37.7	Fair	7.9 ± 0.3
139-855C-6R	57.2	Excellent	20.4 ± 0.2
139-855C-8R	67.6	Good	26.9 ± 0.4
139-855C-10R	95.7	Fair	>26.1
139-855D-1W	80.6	Poor	—

Note: — indicates no useful data.

[a]WSTP measurements were made after the specified core, at a depth 1.1 m greater than the maximum coring depth.

[b]Quality is subjective and based on interpretations described in the text.

[c]Estimated error is based on a subjective assessment of deployment operations and how well recovered data fit a theoretical model.

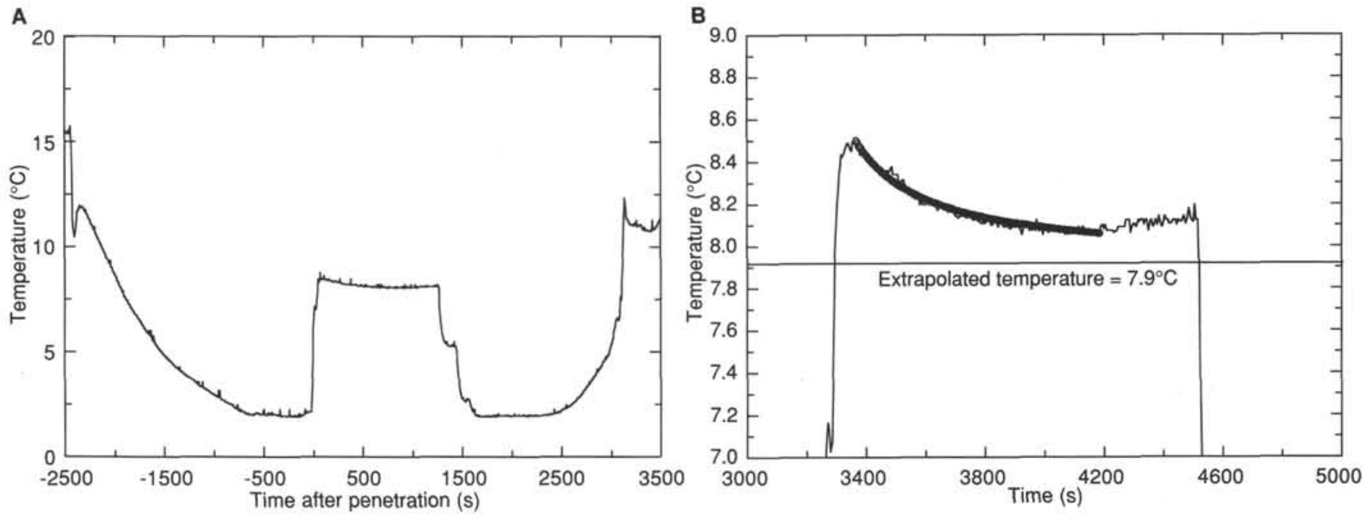

Figure 52. **A.** WSTP temperature vs. time after penetration following recovery of Core 139-855C-4R (36.6 mbsf). **B.** Detail of this deployment, comparing measured (line) and modeled (open circles) temperatures, with data-logger noise removed by hand.

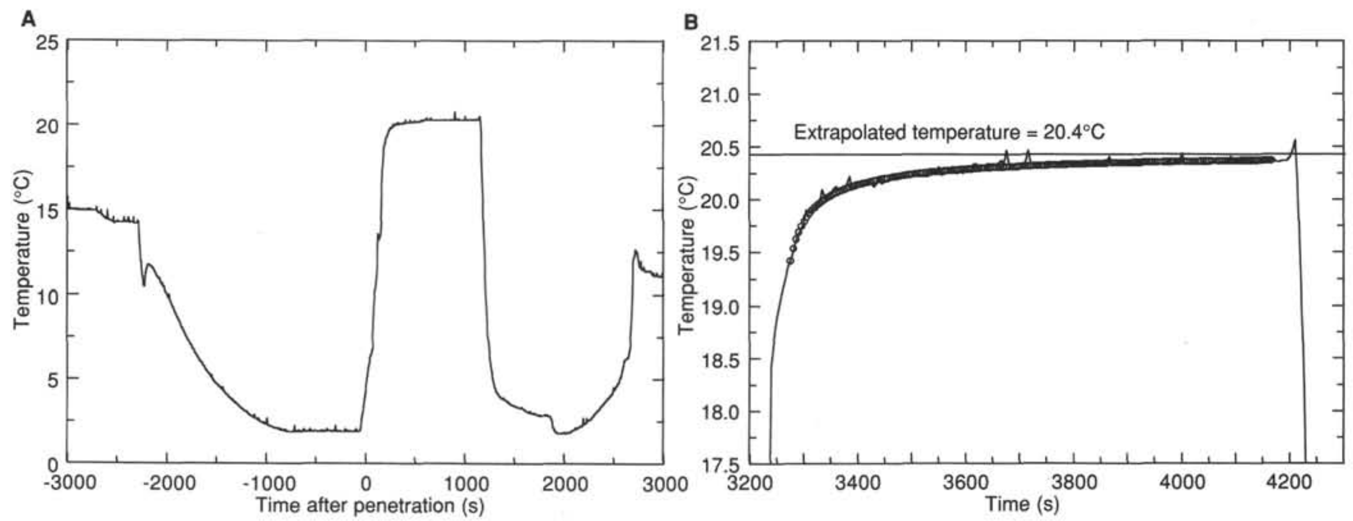

Figure 53. **A.** WSTP temperature vs. time after penetration following recovery of Core 139-855C-6R (57.2 mbsf). **B.** Detail of this deployment, comparing measured and modeled temperatures, with data-logger noise removed by hand. Symbols as in Figure 52.

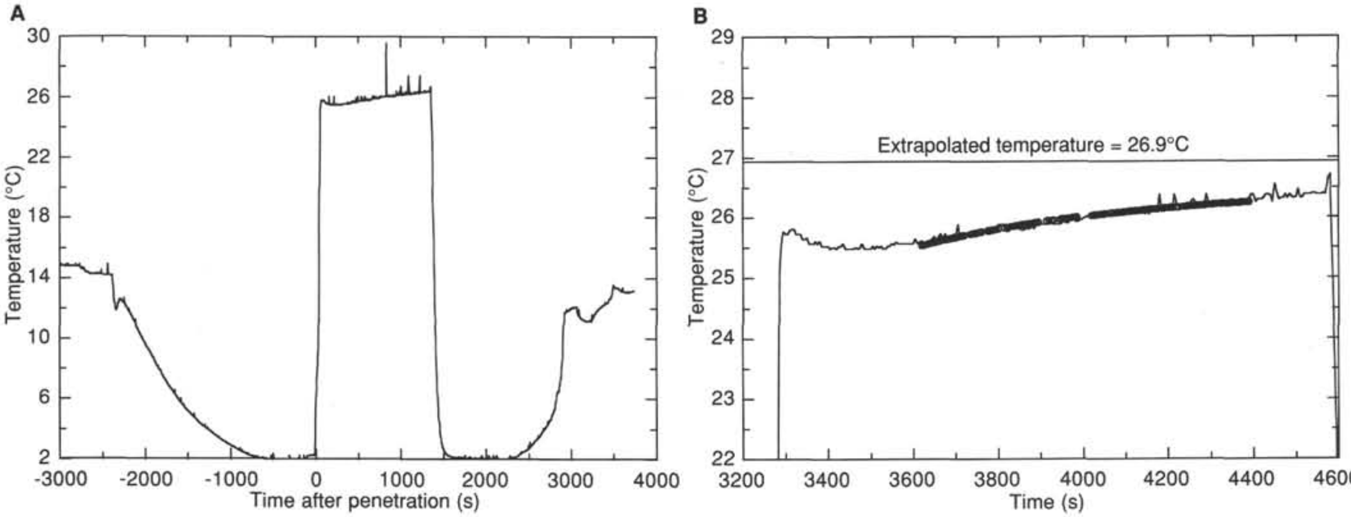

Figure 54. **A.** WSTP temperature vs. time after penetration following recovery of Core 139-855C-8R (76.3 mbsf). **B.** Detail of this deployment, comparing measured and modeled temperatures, with data-logger noise removed by hand. Symbols as in Figure 52.

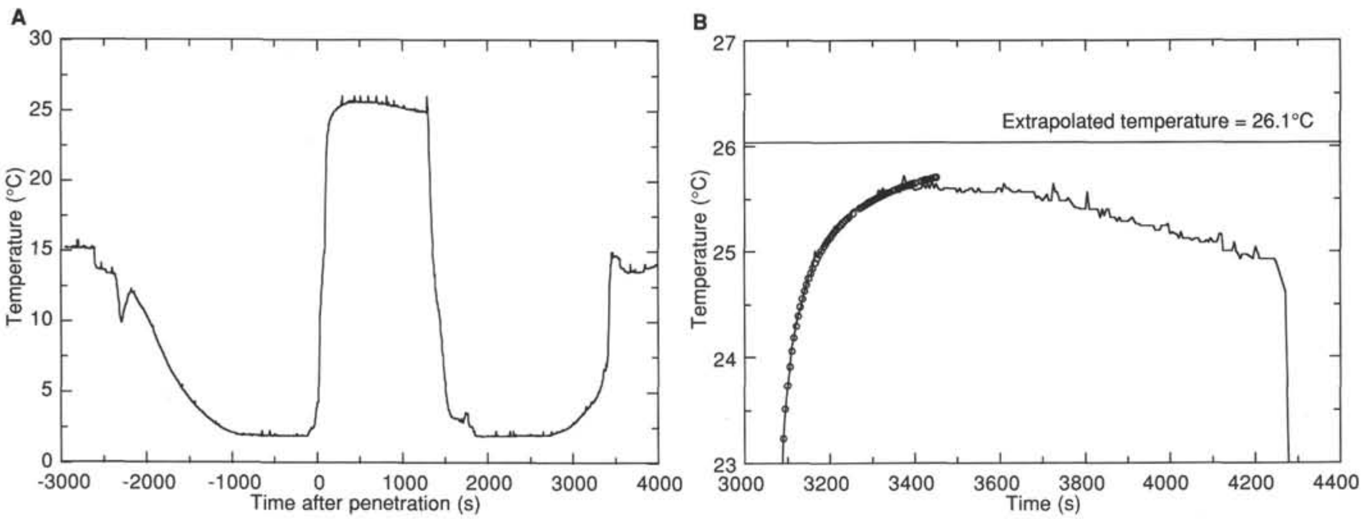

Figure 55. **A.** WSTP temperature vs. time after penetration following recovery of Core 139-855C-10R (95.7 mbsf). **B.** Detail of this deployment, comparing measured and modeled temperatures, with data-logger noise removed by hand. Symbols as in Figure 52.

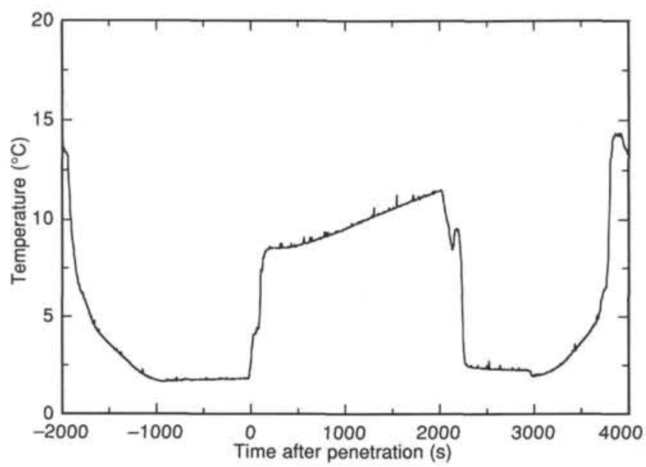

Figure 56. WSTP temperature vs. time after penetration following recovery of Core 139-855D-1W (80.6 mbsf).

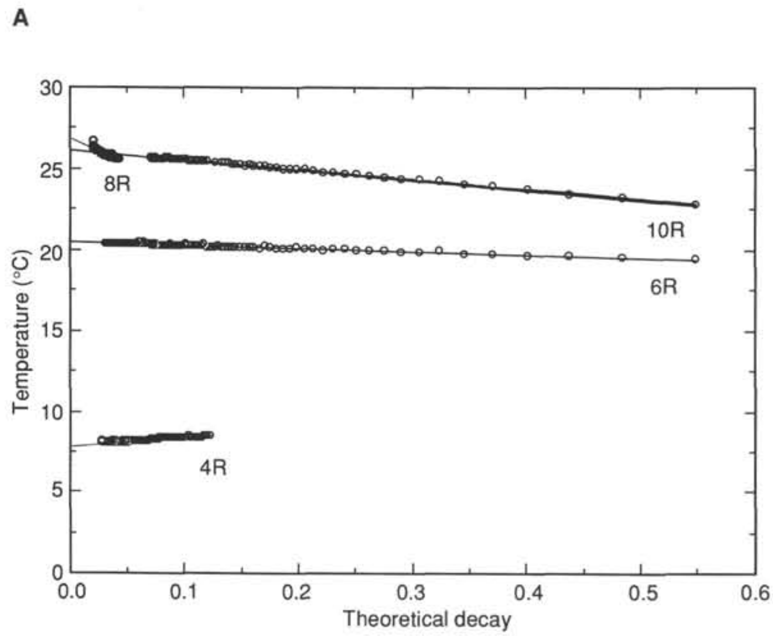

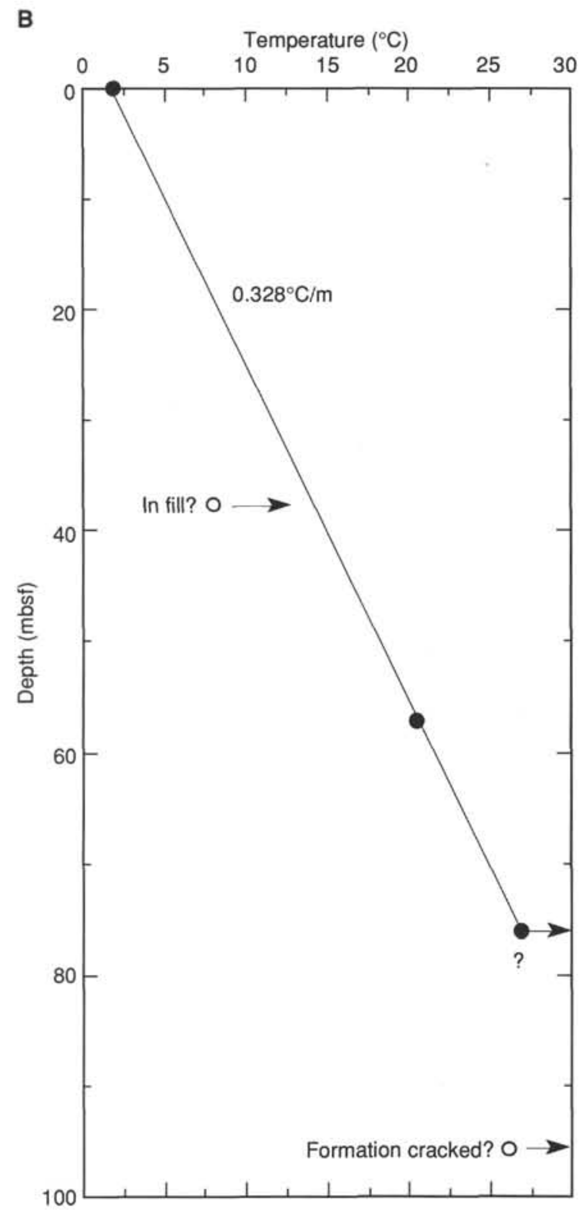

Figure 57. **A.** Temperature vs. theoretical decay. Circles are measured temperatures and lines are modeled temperatures. **B.** Estimated temperatures vs. depth in Hole 855C. The least-squares best-fitting linear gradient through the two most reliable subsurface temperatures, following recovery of Cores 139-855C-6R and -8R (at 57.2 and 76.3 mbsf), and bottom water (solid circles) is 0.328°C/m.